MICROCOPY RESOLUTION TEST CHART
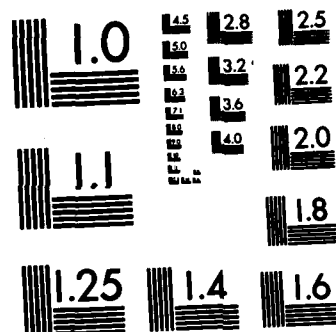
NATIONAL BUREAU OF STANDARDS-1963-A

AD A 124681

MODELING THE HELMET-MOUNTED SIGHT SYSTEM

THESIS

AFIT/GE/EE/82D-24   Wayne R. Clubine
                      Capt   CAF

DTIC
SELECTED
FEB 2 2 1983

A

DEPARTMENT OF THE AIR FORCE
AIR UNIVERSITY (ATC)

AIR FORCE INSTITUTE OF TECHNOLOGY

DTIC FILE COPY

Wright-Patterson Air Force Base, Ohio

AFIT/GE/EE/82D-24

MODELING THE HELMET-MOUNTED SIGHT SYSTEM

THESIS

AFIT/GE/EE/82D-24

Wayne R. Clubine
Capt   CAF

Approved for public release; distribution unlimited

MODELING THE HELMET-MOUNTED

SIGHT SYSTEM

THESIS

Presented to the Faculty of the School of Engineering

of the Air Force Institute of Technology

Air University

in Partial Fulfillment of the

Requirements for the Degree of

Master of Science

by

Wayne R. Clubine, B.S.

Capt   CAF

Graduate Electrical Engineering

December 1982

Preface

The latest advances in Helmet-Mounted Sight technology provides a wide range of possible applications that take advantage of the head's natural aiming ability to control a sensor or weapon. As is the case with most modern weapon systems, before any hardware is built, a model or simulation of the proposed system is developed to predict the performance of the equipment configuration. Since the Helmet-Mounted Sight may be a component of these systems, then it too must be part of the simulation. In order to simulate the performance of the Helmet-Mounted Sight in the proposed weapon system, an accurate model of the sight and the factors that effects its accuracy and performance must be developed. It is the intent of this study to develop such a model. The performance of this model in a simulation program is presented after the development of the model, to demonstrate the effect of an improved model on the simulation results.

The achievement of the results presented here would not have been possible without the support and guidance rendered me by Lt Col Robert M. Edwards, my thesis advisor, and Mr. Stanton H. Musick, the project sponsor. The opportunity to work with these gentlement has been a valuable and enjoyable educational experience.

Finally, I wish to thank my wife, Carol, for her love and understanding during this challenging period.

Wayne R. Clubine

ii

Contents

List of Figures

List of Tables

Abstract

This report describes the development of an error model for the Helmet-Mounted Sight System. This model is designed to generate the HMS aiming errors that are encountered when the sight is used in the Navigation Update role. This report details the research performed to identify. catagorize, and model the Helmet-Mounted Sight (HMS) errors. The HMS error model includes errors generated by the human operator. the HMS equipment, the vibration enviroment, canopv refraction, and the system boresighting procedure. The final portion of this report demonstrates the performance of this model in a Monte Carlo simulation program.

MODELING THE HELMET-MOUNTED

SIGHT SYSTEM

I Introduction

This report presents the development of an error model for the Helmet-Mounted Sight (HMS) system. The model is specifically designed to generate the HMS aiming errors that are encountered when the sight is used in the Navigation Update role. The bulk of this report details the research performed to identify, catagorize, and model the Helmet-Mounted Sight errors. The final sections of this report demonstrate the use of the HMS error model in a Monte Carlo simulation program.

Modern aircraft require accurate estimates of the aircraft acceleration and velocity for precise navigation and weapon delivery. This requirement has led to the development and use of onboard inertial navigation equipment. Conceptually the inertial navigation system is self-contained, but in practice its performance deteriorates seriously with time, unless external indications of the aircraft position, velocity, or attitude are used to remove or bound the system errors. The use of external measurements, properly accounting for measurement and sensor errors, has become the primary means of improving inertial navigation accuracy.

A new method of providing update information to the inertial navigation system is currently being studied by the Air Force's Avionics Laboratory. This inertial aiding technique is called the Low Altitude Navigation Augmentation (LANA) system. This concept first proposed by the Charles Stark Draper Laboratory (CSDL) is a passive, self-containing

means of conducting head-up, low altitude flight operations, with enhanced navigation performance. With this system, the pilot, using a helmet-mounted sight, takes a position fix of a presurveyed landmark that has been cued for him on his head-up display. The bearing angles which describe the attitude of the helmet are processed through a Kalman filter and used to update the inertial navigation system (Ref 1:1).

A working simulation of the LANA system has been developed by the Avionics Laboratory for a typical mission scenario. The present simulation employs a necessarily simplified model of the helmet-mounted sight errors, because the information to identify and define the full range of these errors was not readily available. This application of the HMS is not known to have been previously studied.

Research Goals

The objective of this thesis was to identify, define, and model the helmet-mounted sight system errors. Once an error model was developed, this model was to be implemented into the truth model of the LANA simulation. The truth model or "reference model" is the best, most complete mathematical model of the real world system under study. In a simulation program the truth model supplies information that normally would be generated by the real world environment. Finally, a sensitivity analysis was to be performed with the new truth model, and changes to the simulation Kalman filter would be considered to reflect the improved HMS model.

Background

As previously mentioned, the Low Altitude Navigation Augmentation (LANA) concept uses a Helmet-Mounted Sight (HMS) to allow the pilot to

2

take position "fixes" with which to update the aircraft Inertial Navigation System (INS). The current method of taking a position fix requires the aircraft to overfly the landmark. However, under actual combat conditions it may be inconvenient or hazardous to fly directly over a known checkpoint. With a helmet-mounted sight it is possible to take a position fix on a landmark which is offset some distance from the aircraft's flight path, and to do it with minimal pilot workload.

The LANA system uses information about a particular area of terrain which has been obtained from airborne or satellite reconnaissance. The prominent features and landmarks of a predetermined course over this terrain are stored in the navigation computer as land-mass data. As the aircraft flies along the course the on-board computer projects onto the Head-Up Display (HUD), a simulated outline of the terrain which the pilot should see before him. This outline is generated based upon the aircraft's estimated position and the available land-mass data for that position. A navigation update begins when the pilot searches out and identifies a pre-surveyed landmark that has been cued for him on the HUD. He aligns the reticle on his HMS with the landmark and signals the on-board computer that alignment has been achieved. At this instant the bearing angles that describe the helmet's line-of-sight are read into the navigation computer and used in a Kalman filter to limit error growth in position, velocity, and attitude (Ref 1:2).

If this system can be made to perform as envisioned it can offer a number of significant advantages. The principle benefit is the ability to take position fixes without having to overfly heavily defended areas. There is also a reduction in the aircrew workload, "by using the natural head-up tracking abilities of the pilot it permits a completely head-up

and hands-free means of updating the INS" (Ref 2:29). This system has
advantages in weight and cost when compared to other means available; it
is self-contained and cannot be easily disrupted by enemy
countermeasures.

Sequence of Presentation

This report has been structured in the following manner:

1. Chapter II describes the approach taken to develop the error
models and presents the models in summary form. A brief description
of the LANA simulation program and its use of the Monte Carlo
simulation program SOFE is presented.

2. Chapter III defines and describes the different ways of
expressing statistical measures of error that are used in the
literature and appear in the subsequent chapters.

3. Chapter IV to Chapter VII are the detailed analysis of the
individual HMS errors and the development of a model for each error
source.

4. Chapter VIII takes all the models from Chapter IV through
Chapter VII and discusses their implementation into the truth model
of the LANA simulation.

5. Chapter IX presents the results of a number of Monte Carlo
studies to demonstrate the effects of the new HMS error model on the
LANA simulation.

6. Chapter X presents the conclusions and recommendations which
were derived from this study.

4

II Approach

LANA Program

The Avionics Laboratory is examining the LANA concept through Monte Carlo simulation. The LANA simulation was implemented using a general purpose program called SOFE, which stand for Simulation for Optimal Filter Evaluation (Ref 3). This program requires the designer to supply user-written subroutines which specify the system under study, including both the truth and filter models. The filter model refers to the Kalman filter that is used in the simulation. The Kalman filter is data processing algorithum. In the simulation program it represents a computer program in the aircraft computer which calculates estimates of quantities of interest that describe the states of the system. For example, in the LANA simulation the position measurements are used to also update the position, velocity, and attitude. The reader is referred to the SOFE user's manual (Ref 3) for a complete description of the SOFE program.

Because of the nonlinear nature of the bearing angle measurements, the LANA Kalman filter is implemented in SOFE as an extended Kalman Filter. This simulation is capable of updating the aircraft position relative to the landmark using only the azimuth and elevation angles (the bearing angles) of the line-of-sight (LOS) pointing vector to the landmark. The LANA simulation also contains the ability to update the INS using laser range measurements from the aircraft to the landmark. This capability has been shown by Avionics Lab personnel to help stabilize the Kalman filter, but will not be explored in this report. The range measurements provide an independent measure of the target range

5

to overcome the basic observability problem which arises when only bearing angle measurements are used to calculate the LOS pointing vector and range to the landmark. The range state in the Kalman filter can become unobservable when only the bearing angle information is provided in the measurement. This observability problem arises from the uncertainty of the estimate of the aircraft velocity. Without the range measurement it is possible that the estimation error of the range would not decrease, regardless of how long measurements were taken. The range measurements help to stabilize the Kalman filter, but the observability problem was not severe enough to mandate the use of the range finder (Ref 29:46). The complete description of the reference frames used and the non-linear and linearized measurement equations are presented in Ref 1, titled, "Landmark Observation Equations for Kalman Filter Update in LANA."

The LANA simulation uses data from the trajectory driver program PROFGEN (Ref 4). The mission and hence each Monte Carlo runs lasts for 7200 seconds (2 hours). For the first 1440 seconds (24 minutes) the flight is over water during which time no position fixes are possible. After landfall at the 1440 second point, update measurements are taken approximately every 300 seconds (5 minutes) until the end of the mission. These update measurements occur in a three measurement bursts, each update consisting of an azimuth and elevation measurement for Kalman processing. The three measurements within a burst are spread over a three second interval. This update measurement sequence simulates a mission where a landmark is cued to the pilot on his HUD every five minutes; at that time the pilot finds the landmark and takes three successive position fixes with the HMS as he closes on the landmark. In

6

the LANA simulation, three nominal ranges are employed for initial fix
range in any burst series, 20,000, 15,000, and 10,000 feet.

The original LANA program which has the simplified HMS model,
contains a 49-state truth model and a 15-state filter model. Table 2.1
shows the truth states used while Table 2.2 illustrates the filter
states. Truth states one through forty-seven represent Widnall and
Grundy's error model for the Litton LN-15 local-level INS, with a
barometric altimeter altitude reference model (Ref 5:143). Truth states
48 and 49 are the azimuth and elevation first-order Markov processes
which were used to model bias type error for the two components of the
LOS bearing angle measurement. Filter states one through thirteen are
the reduced order representative of the original 49 truth states. Filter
states for the HMS measurements 14 and 15 are intended to model truth
states 48 and 49.

This study will not alter the structure of the first 47 truth
states, nor the first 13 filter states of the original model. The truth
and filter states which represent the helmet-mounted sight errors will be
modified or replaced as a result of the HMS error model development
detailed in the following chapters.

Helmet-Mounted Sight Error Overview

To assist the reader's understanding of the structure of the HMS
error model, which will be developed in the remaining chapters, the
following overview of error sources is presented. A detailed review of
the literature and discussions with Air Force engineers working with HMS
systems has resulted in the catagorization of the HMS errors into three
groups. First, there are the errors resulting from the human factor, or

Table 2.1   Original LaMA Truth Error States (Ref 35)

Truth State Index	Error Source	Error Model	Input Parameters		
			Initial One Sigma Value	Noise Spectral Density	Correlation Parameter
1	East Longitude	Dynamic	221.8 Cos(LT)FT.		
2	North Latitude	Dynamic	191.1 Feet		
3	Altitude	Dynamic	30.0 Feet		
4	East Velocity	Dynamic	0.1 FT/SEC		
5	North Velocity	Dynamic	0.1 FT/SEC		
6	Vertical Velocity	Dynamic	0.1 FT/SEC		
7	East Attitude	Dynamic	0.5E-01 MRAD		
8	North Attitude	Dynamic	0.5E-01 MRAD		
9	Vertical Attitude	Dynamic	0.4 MRAD		
10	Vertical Acceleration	Dynamic	$0.6E-02$ FT/SEC^2		
11	X Gyro Drift	Random Walk	0.6E-02 DEG/HR	0.3E-02 $(Deg/Hr)^2$	
12	Y Gyro Drift	Random Walk	0.3E-02 DEG/HR	0.3E-02 $(Des/Hr)^2$	
13	Z Gyro Drive	Random Walk	0.5E-02 DEG/HR	0.5E-02 $(Deg/Hr)^2$	
14	X Gyro G-Sens Drift, Input (X)	Random Constant	0.3 DEG/HR/G		
15	Y Gyro G-Sens Drift, Spin (Y)	Random Constant	0.3 DEG/HR/G		
16	Y Gyro G-Sens Drift, Spin (X)	Random Constant	0.3 DEG/HR/G		

Truth State Index	Error Source	Error Model	Initial One Sigma One	Noise Spectral Density	Correlation Parameter
			. . . . Input Parameters		
17	Y Gyro G-Sens Drift Input (Y)	Random Constant	0.3 DEG/HR/G		
18	Z Gyro G-Sens Drift, Spin (Y)	Random Constant	0.3 DEG/HR/G		
19	Z Gyro G-Sens Drift, Input (Z)	Random Constant	0.2E-01 DEG/HR/G		
20	X Gyro G*G-Sens Drift	Random Constant	0.4E-01 DEG/HR/(G*G)		
21	Y Gyro G*G-Sens Drift	Random Constant	0.4E-01 DEG/HR/(G*G)		
22	Z Gyro G*G-Sens Drift	Random Constant	0.2E-02 DEG/HR/(G*G)		
23	X Gyro Scale Factor	Random Constant	300.0 PPM		
24	Y Gyro Scale Factor	Random Constant	300.0 PPM		
25	Z Gyro Scale Factor	Random Constant	1000.0 PPM		
26	X Gyro Misalignment About Y	Random Constant	40.0 ARC SEC		
27	X Gyro Misalignment About Z	Random Constant	40.0 ARC SEC		
28	Y Gyro Misalignment About X	Random Constant	40.0 ARC SEC		
29	Y Gyro Misalignment About Z	Random Constant	40.0 ARC SEC		
30	Z Gyro Misalignment About X	Random Constant	40.0 ARC SEC		
31	Z Gyro Misalignment About Y	Random Constant	40.0 ARC SEC		
32	X Accelerometer Bias	Random Walk	50.0 UGEE	$(10. \ UGEE)^2/HR$	
33	Y Accelerometer Bias	Random Walk	50.0 UGEE	$(10. \ UGEE)^2/HR$	

Truth State Index	Error Source	Error Model	Initial One Sigma Value	Noise Spectral Density	Correlation Parameter
				. . . . Input Parameters	
34	Z Accelerometer Bias	Random Walk	100.0 UGEE	$(10.\ UGEE)^2$/HR	
35	X Accelerometer Scale Factor	Random Constant	150.0 PPM		
36	Y Accelerometer Scale Factor	Random Constant	150.0 PPM		
37	Z Accelerometer Scale Factor	Random Constant	150.0 PPM		
38	X Accel Misalignment About Y	Random Constant	30.0 ARC SEC		
39	X Accel Misalignment About Z	Random Constant	180.0 ARC SEC		
40	Y Accel Misalignment About Z	Random Constant	30.0 ARC SEC		
41	Y Accel Misalignment About X	Random Constant	180.0 ARC SEC		
42	Z Accel Misalignment About Z	Random Constant	30.0 ARC SEC		
43	Z Accel Misalignment About Y	Random Constant	30.0 ARC SEC		
44	Baro Altimeter Bias	First Order Markov	100.0 Feet	$0.2E+04\ FT^2$/NM	0.25E+03 NM
45	X Gimbal Misalignment	First Order Markov	4.0 MRAD	$0.18E-1\ MR^2$/SEC	0.18E+04 SEC
46	Y Gimbal Misalignment	First Order Markov	4.0 MRAD	$0.18E-1\ MR^2$/SEC	0.18E+04 SEC
47	Z Gimbal Misalignment	First Order Markov	4.0 MRAD	$0.18E-1\ MR^2$/SEC	0.18E+04 SEC
48	Azimuth Measurement Bias	First Order Markov	0.3 Degrees	$0.1E-02\ DEG^2$/SEC	0.18E+04 SEC
49	Elevation Measurement Bias	First Order Markov	0.3 Degrees	$0.1E-03\ DEG^2$/SEC	0.18E+04 SEC

Table 2.2 Original LANA Filter States (Ref 35)

Filter State Index	Error Source	Error Model	Initial One Sigma Value	Noise Spectral Density	Correlation Parameter
1	East Longitude	Dynamic	221.8 Cos(LT)FT		
2	North Latitude	Dynamic	191.1 FT		
3	Altitude	Dynamic	30.0 FT		
4	East Velocity	Dynamic	0.1 FT/SEC		
5	North Velocity	Dynamic	0.1 FT/SEC		
6	Vertical Velocity	Dynamic	0.1 FT/SEC		
7	East Attitude	Dynamic	0.5E-1 MR		
8	North Attitude	Dynamic	0.5E-1 MR		
9	Vertical Attitude	Dynamic	0.4 MR		
10	Baro Altimeter Bias	First Order Markov	100.0 FT	$0.2E+4$ FT^2/NM	$.25E+3$ NM
11	X Gyro Drift	Random Walk	0.3E-2 DEG/HR	$(.36E-2$ DEG/HR$)^2$/HR	
12	Y Gyro Drift	Random Walk	0.3E-2 DEG/HR	$(.36E-2$ DEG/HR$)^2$/HR	
13	Z Gyro Drift	Random Walk	0.5E-2 DEG/HR	$(.6E-2$ DEG/HR$)^2$/HR	
14	Azimuth Measurement Bias	First Order Markov	0.2865 DEG	$0.1E-3$ DEG^2/SEC	1800 SEC
15	Elevation Measurement Bias	First Order Markov	0.2865 DEG	$0.1E-3$ DEG^2/SEC	1800 SEC

11

human operator. Since the pilot is part of the overall system, his aiming errors are a component of the total system aiming error. Next are the errors resulting from the environment. These include vibrational effects on the human and canopy refraction effects. Last are the HMS equipment or hardware related errors, i.e. the inherent inaccuracy of the helmet-mounted sight itself. To clarify the terminology that will be used in this report the term Helmet-Mounted Sight System, with the emphases on system, is intended to include all the HMS system components, the operator, environment and the HMS equipment. The term HMS system model is an all-inclusive term referring to the combined operator, environment, and equipment models. The term HMS model refers to the HMS equipment model only.

The errors and their relationship to the landmark measurements are modeled as follows:

Azimuth Component

$$\tilde{Z}_{Az} = Z_{Az} + E_{Hu_{Az}} + E_{Vib_{Az}} + E_{Can_{Az}} + E_{Hel_{Az}} + E_{BS_{Az}} + v_{Az} \qquad (2\text{-}1)$$

Elevation Component

$$\tilde{Z}_{El} = Z_{El} + E_{Hu_{El}} + E_{Vib_{El}} + E_{Can_{El}} + E_{Hel_{El}} + E_{BS_{El}} + v_{El} \qquad (2\text{-}2)$$

where $\tilde{Z}_{Az}$ and $\tilde{Z}_{El}$ represent the azimuth and elevation measurements.

Z_{Az} and Z_{El} represent the sine of the true azimuth and elevation measurements.

$E_{Hu_{Az\&El}}$ are the azimuth or elevation components of the human sighting error.

$E_{Vib_{Az\&El}}$ are the azimuth or elevation components of the vibration error.

$E_{Can_{Az\&El}}$ are the azimuth or elevation components of the canopy refraction error.

12

$E_{Hel_{Az\&El}}$ are the azimuth or elevation components of the helmet HMS readout error.

$E_{BS_{Az\&El}}$ are the azimuth and elevation components of the HMS initial alignment errors.

$V_{Az\&El}$ is white measurement noises added to the azimuth and elevation components of the measurement to account for the unmodeled error sources.

III Error Describing Terms

The performance of the LANA system is influenced by a variety of disturbances, and describing the estimated performance of this system requires knowledge of the probability distribution of these disturbances or errors. The experimental data from the literature, upon which the models of these errors are based, were often condensed into a single measure to be used as a performance indicator. But the use of different measures by various authors can cause difficulty in making comparisons. This chapter is intended to make such comparisons easier, by providing the relationships between the commonly used error measures. These relationships are the basis for the conversions used in later chapters.

The most commonly used forms to express the results of two dimensional target aiming experiments are as follows:

Mean Radial Error ($\bar{R}$)

Standard Deviation of the Radial Error (σ_R)

Root Mean Square Radial Error (RMS_R)

Circular Error Probable (CEP)

Mean of the Azimuth or Elevation Error ($\bar{Az}, \bar{El}$)

Standard Deviation of the Azimuth or Elevation Error (σ_{Az}, σ_{El})

The LANA simulation requires that the helmet-mounted sight system errors be specified in terms of the azimuth (horizontal) and elevation (vertical) components of the pilot's line-of-sight vector. Therefore the effects of the corrupting errors will also be evaluated and modeled in terms of their azimuth and elevation components. The units of measurement will be standardized to feet, seconds, and radians.

14

The most commonly used means of describing target aiming error is some measure of the radial error, where

Radial Error (R) - is the angular distance between the vector from the eye to the target and the vector from the eye to the aim point. See Figure 3.1.
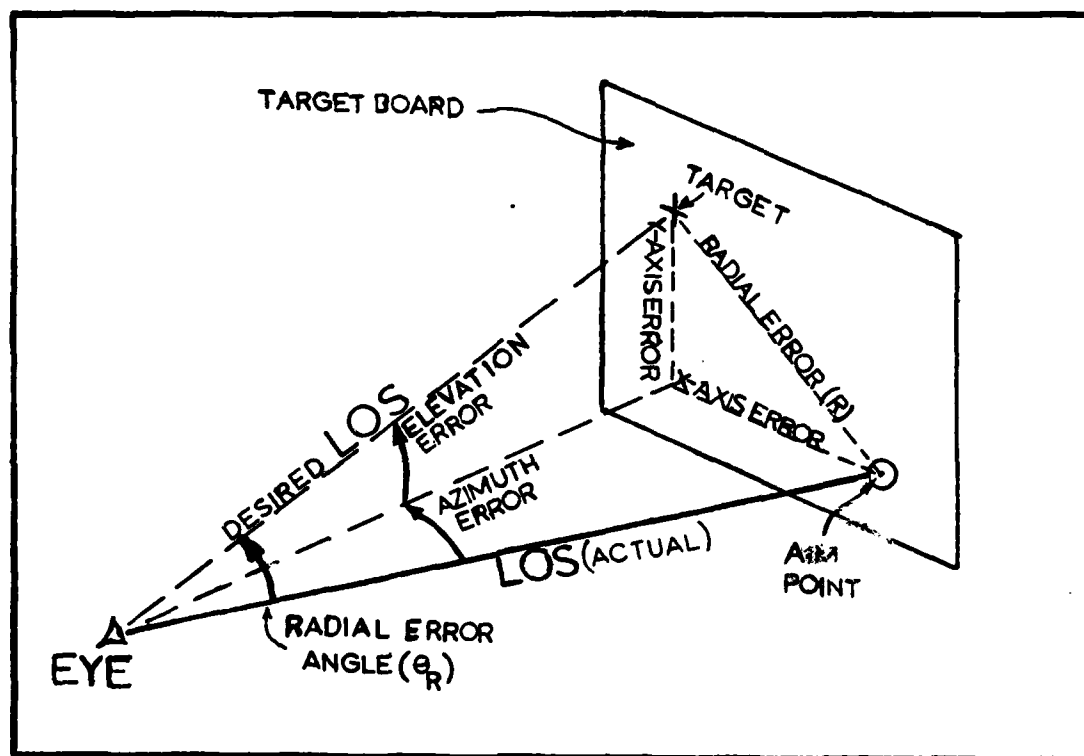
Figure 3.1 Definition of Data Terminology

If the experiment has some form of systematic error or bias, then the errors may be expressed in any of the forms shown in Figure 3.2. If the experimenter has removed the system bias, either physically or statistically, then the errors will have a distribution which is centered over the target. This correction moves the center of the tracking centroid, shown in Figure 3.2, to the target location. These errors are typically described by one of the terms shown in Figure 3.3. The head

15
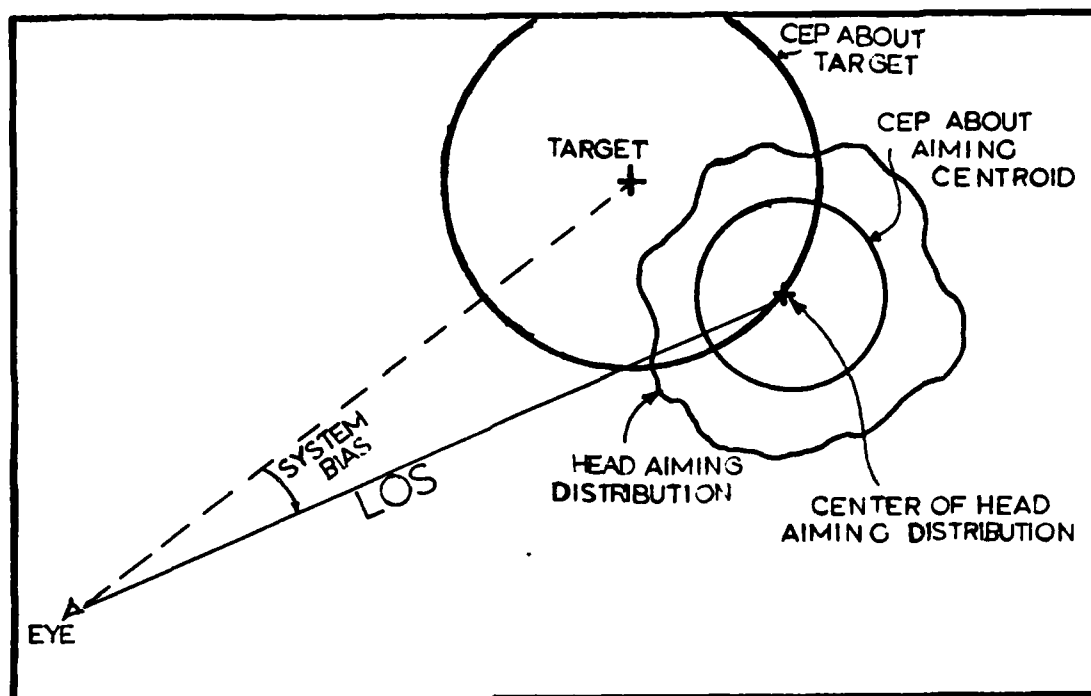
Figure 3.2   Data Terminology for a System with a Bias (Ref 6)
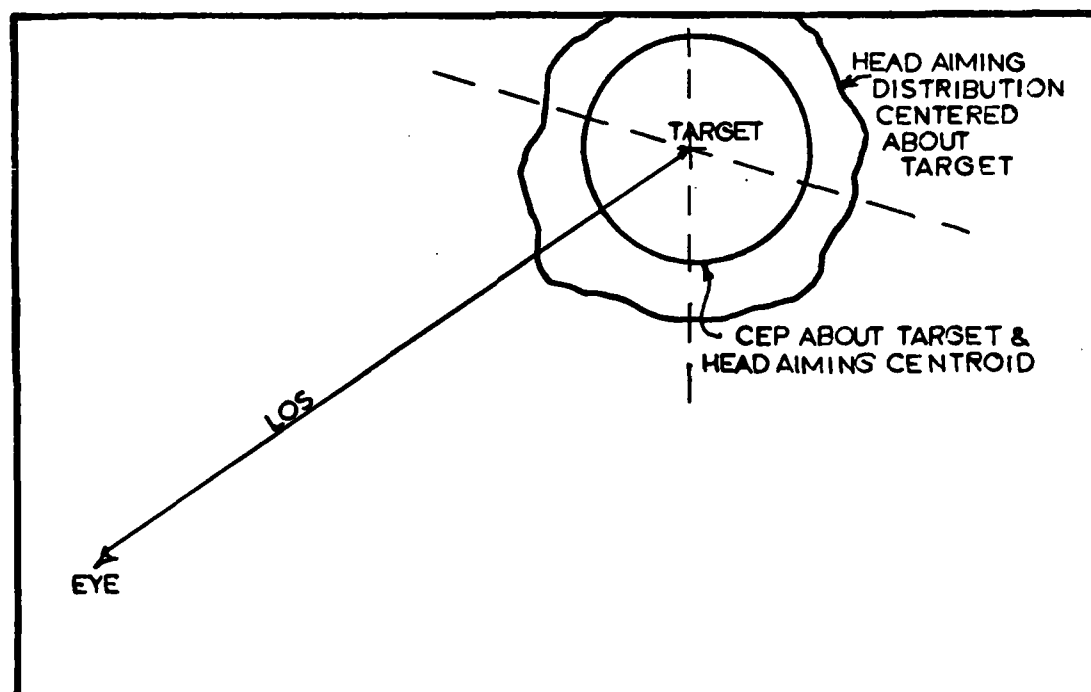
Figure 3.3   Data Terminology for an Unbiased System (Ref 6)

16

tracking distribution, in most experiments, is centered about the target such that there is a zero mean error distribution, or the sum of the X and Y components of the aiming errors approaches zero as the number of measurement becomes large.

From Figure 3.1, we can see that if the radial error angle (Θ_R) is small and the LOS is perpendicular to the target board then

$$\Theta_R = \tan^{-1}\left(\frac{R}{d}\right) \approx \left(\frac{R}{d}\right) \qquad (3-1)$$

where   d   is the distance from the eye to the plane of

the target,

and   R = radial error $= \sqrt{X^2 + Y^2}$.   (3-2)

Then the mean radial error $(\bar{R})$ is

$$\bar{R} = E[R] = E[\sqrt{X^2 + Y^2}], \qquad (3-3)$$

The variance of the Radial Error (σ_R^2) is

$$\sigma_R^2 = E[(R - E[R])^2], \qquad (3-4)$$

and the Standard Deviation of the Radial Error (σ_R) is

$$\sigma_R = \sqrt{\sigma_R^2} \qquad (3-5)$$

Bivariate Normal Distribution. The bivariate normal, or the two-dimensional Gaussian distribution, can be represented as the joint probability density function of the form

$$f(x,y) = \frac{1}{2\pi\sigma_x\sigma_y\sqrt{1-\rho^2}} \; e^{-G/2}, \qquad (3-6)$$

where

$$G = \left\{-\frac{1}{(1-\rho^2)}\left[\frac{(x-\bar{x})^2}{\sigma_x^2} - 2\rho\frac{(x-\bar{x})(y-\bar{y})}{\sigma_x\,\sigma_y} + \frac{(y-\bar{y})^2}{\sigma_y^2}\right]\right\} \qquad (3-7)$$

given that   X and Y are continuous random variables

ρ is the correlation coefficient between X and Y

(x,y) is the mean of this distribution.

Therefore the probability that any point (x,y) falls in a region S of the

x,y-plane is

$$P(S) = \iint_s f(x,y) \, dx \, dy \quad (\text{Ref } 7{:}97).\qquad(3\text{-}8)$$

Circular Case. In the case where $\sigma_x = \sigma_y = \sigma$ and the correlation coefficient $\rho = 0$, then the normal or Gaussian distribution is called circular. The probability density corresponding to $f(x,y)$ is

$$f(R) = (R/\sigma^2)\, e^{-R^2/2^2},$$

where $\quad R^2 = (x-\bar{x})^2 + (y-\bar{y})^2$, is the radial error.

The probability ellipses have become circles. When the systematic error, or system bias has been removed, then the point (x,y) is located at the origin and

$$\bar{x} = 0.0,$$

$$\bar{y} = 0.0.$$

The radial error becomes

$$R = \sqrt{x^2 + y^2}.$$

The majority of the error terms in this literature are expressed in terms of radial error (R). Because the LANA simulation requires the errors be broken into their azimuth and elevation components, all the error values are converted to the bivariate normal distributions. Most of the results for target aiming experiments in the literature have zero mean error distributions. Unfortunately, the experimental results do not usually indicate if the error distribution is isotropic or uniform in all directions or whether there is any correlation between the errors. Therefore, lacking any information to the contrary, unless otherwise stated, all the error distributions will be assumed to be zero-mean, bivariate normal distributions, where $\sigma_{Az} = \sigma_{El} = \sigma$, and the correlation coefficient $\rho = 0$. From here onwards this error distribution shall be called the "Circular Distribution". The circular error probable (CEP)

18

can be defined as the circle of radius R into which 50% of the
probability distribution lies, and

$$CEP = 0.5887 \left[\sigma_x + \sigma_y \right]. \tag{3-9}$$

This formula is an approximation which is good over a wide range of σ_X
and σ_Y (Ref 7:101).

For the circular case, when $\sigma_x = \sigma_y = \sigma$, then CEP $= 1.1774\sigma$.

Rayleigh Distribution. The Rayleigh distribution has wide applications
to two dimensional target problems; since the value of the radial error
(R) is always positive and maps into the set of positive real numbers.
Rayleigh distributions are part of a family associated with the Gaussian
or normal distributions, where the bivariate normal random variables x
and y are mapped to the Rayleigh distribution using the function

$$R = \sqrt{x^2 + y^2}$$

This association can be seen by comparing the Rayleigh distribution
functions shown below with the circular case or equiprobability Gaussian
distributions discussed previously. The Rayleigh probability density
function is shown in Figure 3.5.

For the one dimensional case:

$$\text{Rayleigh Distribution, } f(x) = \frac{x}{\sigma^2} e^{-x^2/2\sigma^2} U(x), \tag{3-10}$$

where $U(x)$ is the unit step function

$$U(x) = \begin{cases} 1, & x \geq 0 \\ 0, & x < 0 \end{cases}$$

In the two-dimensional case, the probability density function is

$$f(x,y) = \frac{1}{2\pi\sigma^2} e^{-(x^2+y^2)/2\sigma^2}. \tag{3-11}$$

Now, when x and y are related such that

$$R = \sqrt{x^2 + y^2} \, ,$$

then $\quad f(R) = \frac{R}{\sigma^2} e^{-R/2\sigma^2} U(R). \tag{3-12}$

where $\qquad$ $U(R)$ is the unit step function

$$U(R) = \{ \begin{matrix} 1, & R \geq 0 \\ 0, & R < 0 \end{matrix}$$

Thus, the experimental results that are expressed in terms of mean radial error, standard deviation of the radial error, and the root mean square radial error are all using the Rayleigh distribution to describe the aiming errors.
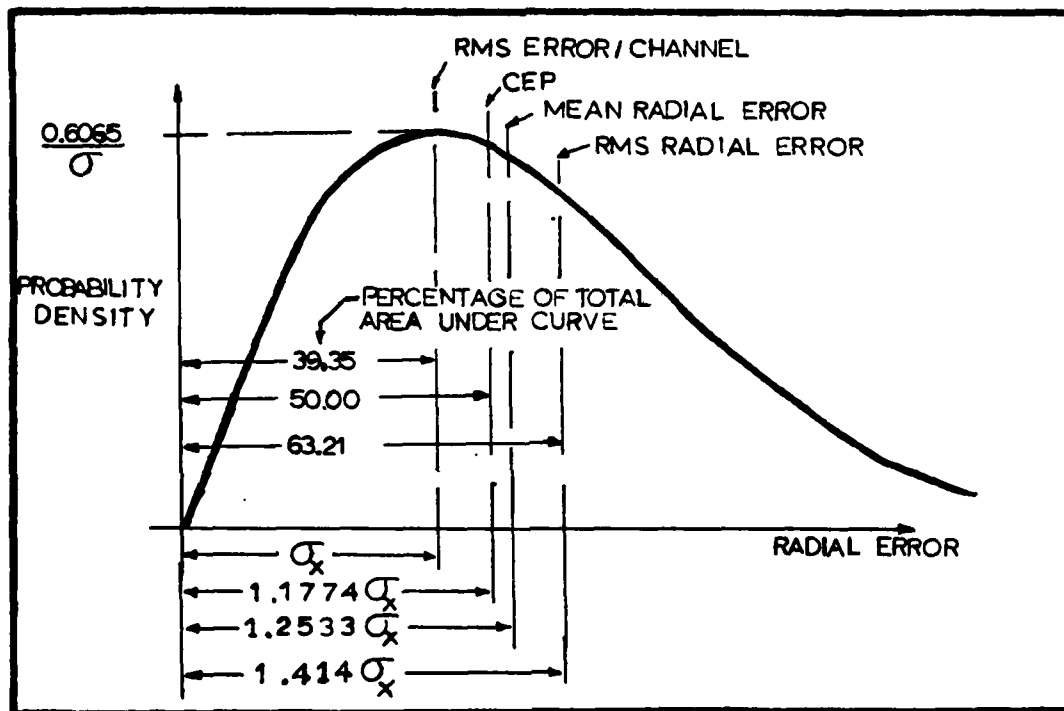
Figure 3.5 Rayleigh Distribution (Ref 9:104)

Conversion Formula

In order to use the experimental data from the literature and compare the findings, a means of converting from the Rayleigh distribution to the bivariate normal means of expressing data is desired. Since the LANA simulation requires that the errors be expressed in terms of the azimuth (x) and elevation (y) components of the error, the following conversion formula will be used to perform the conversions. These formula assume a circular normal distribution with the errors

20

centered on the target with $\sigma_x = \sigma_y = \sigma$ and $\rho = 0$.

The following relationship is used to convert from the Rayleigh to the
bivariate normal distribution:

$$(R) \qquad R = \sqrt{x^2+y^2} \qquad (x,y)$$

$$\text{Rayleigh} \Longleftrightarrow \text{Bivariate Normal.}$$

The conversion formula are:

Mean Radial Error $\quad \bar{R} = E[R] = \sigma\sqrt{\frac{\pi}{2}} = 1.2533\sigma = 1.0645(CEP)$ (3-13)

                                                                     (Ref 7:100)

Root Mean Square
Radial Error $\qquad RMS_R = E[R^2] = \sqrt{2\sigma^2}$ (3-14)

                                                  (Ref 7:100)

Variance of
Radial Error $\qquad \sigma_R^2 = \left(2 - \frac{\pi}{2}\right)^2 = 0.4292\sigma^2$ (3-15)

                                                     (Ref 7:130)

Circular Error
Probable $\qquad CEP = 1.1774\sigma$ (3-16)

                                                         (Ref 7:100).

Terminology

There are three terms that are commonly used to describe the
pointing or aiming process. These are "HMS sighting", "HMS aiming", and
"HMS tracking". In this report the term HMS tracking is mean to imply
the process of continually following or tracking a moving target with the
sight. The term aiming is used when the target is stationary, and also
to describe the instant in time when the HMS operator presses the button
to record his aim point for moving targets. The term sighting is an
all-inclusive term which can be used in place of either aiming or
tracking and usually implies a combination of these actions.

IV Errors Due to the Human Operator

Historically, investigations of human tracking and aiming behavior have involved the use of some type of hand-operated control, i.e. force-stick, track-ball, or a combination of multi-axis controls. In most cases, the operator's task involves accurate hand/eye coordination to minimize the error between a fixed or independently moving reference point and a moving target. The input to the operator is typically visual, and the output is a movement of hand-operated control (Ref 10:2). A number of proposed models for the human hand/eye closed-loop control system are available in the literature (Ref 38 and 39).

The recent development of methods to accurately measure head position has enabled engineers to utilize the head as a control device. Subsequently, the human head coupled with a helmet-mounted sight (HMS) has been demonstrated to be a reliable and accurate means of making precise control responses. Unfortunately, the recent advance in HMS hardware developed have not be equaled by research into the head aiming and tracking capabilities of the human. Unlike the hand-controlled studies, there does not exist a generally accepted model for the movement of the human head when used as a control device for aiming/tracking task, and research results documented in the open literature are often contradictory in nature. Since the interest in measuring human head sighting abilities followed from the development of the head position measurement systems, it is not surprising that many of the experiments to measure head sighting accuracies were flawed by faults in the head position sensing equipment available at that time.

The LANA system profits if the helmet-mounted sight can be aimed at

the landmark with a high degree of accuracy. Since the purpose of this study is to estimate just how accurately this task can be performed, a model of the pilot's aiming accuracy is essential. This chapter reviews the experimental results documented in the literature; then this information, supplemented by current research performed by experts in the field, is used to develop a model of the pilot's aiming sighting.

Modeling Discussion

The development of an accurate model of the head sighting capabilities is dependent upon obtaining quantitative data for pilot performance using a helmet-mounted sight. A measure of this performance, built upon the accuracy and precision of a controlled laboratory experiment, together with data from flight testing, should yield a good basis for a model. A review of the current literature indicates that the following questions must be considered when attempting to quantify the human factor:

1. How accurately can the human aim a helmet-mounted sight at a static target?

2. How accurately can the human use a helmet-mounted sight to track a moving or dynamic target?

3. What are the effects of the target's angular rate of movement upon the pilot's aiming accuracy?

4. Does the position of the head affect a pilot's aiming accuracy?

5. What are the effects on sighting accuracy from the accelerations or G-forces experienced by the pilot in the operational environment?

6. How do the whole body vibrations, which are transmitted through the aircraft seat to the pilot, effect his sighting accuracy?

23

7. What are the effects on sighting accuracy from the workload stresses of flying an aircraft while using the HMS?

The vibrational effects are more complex than they may initially appear, and have a significant impact upon the pilot's sighting accuracy. For these reasons, a later chapter has been devoted to answer this question.

Static Sighting Accuracy

A number of studies have been peformed to investigate the basic human performance capabilities when using a helmet-mounted sight to aim at stationary or static targets under laboratory conditions (viz. Nicholson, 1966; Hughes et al., 1970; Reichwein, 1970; Verona et al., 1979). Often the static sighting tests were performed as portions of more complex experiments, which were intended to study the effects of vibration, target angular rate, or aircraft accelerations on the pilot's aiming ability. The static sighting tests were used as a reference against which the effects of these factors were compared. In each of the studies, the experimental technique and hardware used were different, and all of the experimenters attempted to remove from the sighting accuracy results any systematic errors due to the equipment or experiment design. Most of the experimenters also trained the subjects in the aiming/tracking task until their learning curve became flat.

Nicholson (Ref 11) found that three subjects using a helmet-mounted sight to aim at targets projected on a screen, had a combined sighting error, expressed as a standard deviation of radial error, of 0.13 degrees (2.27 milliradians). He noted that, "it is important to keep in mind that these accuracies were obtained when the subject's average response times were only two seconds"; during which time he was required to locate

24

the target on the screen, superimpose the reticle over the target and press the "pickle" switch (Ref 11:419). Nicholson expressed the sighting errors as a standard deviation of the radial error (σ_R). He removed the constant errors or biases by boresighting the sight and subject prior to collecting the data. It is assumed that the error probability density function is isotropic (uniform in all directions) and therefore the σ_R data can be converted to the circular distribution by using the conversions of Chapter III. The sighting error becomes

$$\sigma_R^2 = (2.27 \text{ mr})^2$$

using $\qquad \sigma_R^2 = (2 - \frac{\pi}{2})^2 \sigma$ $\qquad\qquad\qquad\qquad$ (3-15)

where σ is the standard deviation of the bivariate normal distribution and $\sigma = \sigma_{AZ} = \sigma_{EL}$ $\qquad$ AZ = Azimuth $\quad$ EL = Elevation

therefore $\sigma = 3.45$ milliradians

Hughes (Ref 10) measured the ability of six subjects to sight on a static target, over a 15 second interval, using a helmet-mounted sight. The extra experimental equipment mounted on the helmet required that the helmet be partially supported to reduce the asymmetric weight on the subject's head. Some restriction of head movement was unavoidable. However, Hughes felt that while the restriction may affect the data quantitatively, the qualitative results would still be valid. After removing the constant error or bias, the sighting error for the static target, averaged over the six subjects and expressed as a standard deviation of radial error was 0.14 degrees (2.44 mr). Again assuming a circular error distribution, the aiming error, expressed as a standard deviation, is

$$(2.44)^2 = (2 - \frac{\pi}{2})^2 \sigma$$

$$\sigma = 3.72 \text{ milliradians}$$

25

A study by Verona et al. (Ref 12), was designed to investigate man's head aiming/tracking ability in a simulated helicopter environment, using a very accurate test device. An infrared telescope projector was mounted on the helmet and boresighted with the helmet-mounted sight reticle. A small light in the center of a photocell array was used as a target for the subject to sight and/or track. As the subject tracked the target by superimposing his reticle over it, the coincident beam of infrared light would energize the appropriate photocell(s). This system was able to measure static aiming accuracies to within 1.6 milliradians using a target whose motion was controlled by the experimentor. Any systematic errors or biases were removed by the experimenter by boresighting the subject and HMS equipment prior to each trial.

Verona found that a subject aiming at a static target with a helmet-mounted sight had a root mean squared radial error (RMS_R) of 3.0 milliradians. Again the systematic errors have been removed, and assuming that the probability density function of the aiming errors in the azimuth (horizontal) and elevation (vertical) directions is isotropic, with a zero mean, then the RMS_R error can be converted to values representing the standard deviation of the circular distribution using the conversion formula of Chapter III as follows:

$$(RMS_R)^2 = 2_\sigma^2 \qquad (3\text{-}14)$$

$$(3.0 \text{ mr})^2 = 2_\sigma^2$$

$$\sigma = 2.12 \text{ milliradians}$$

Reichwein (Ref 13) conducted an experiment to determine the effect of steady-state, positive accelerations (+Gz), on a subject's ability to aim a helmet-mounted sight at a stationary target. Performance was measured as a percentage of the time-on-target for a target exposure of

26

20 seconds. The subject was considered to be on target when he held the reticle sight within a 0.25 degree (4.36 mr) circle about the target. The one +Gz level (normal gravity) was used as a reference level for comparison with the higher g-level scores. At the 1.0 g-level, the subject's were found to be capable of holding the target within the 0.25 degree circle for approximately 90% of the time, with a 10% standard deviation between subjects. Again assuming that the distribution of the errors are isotropic, then the Rayleigh distribution conversion to the circular distribution gives

90% of the area under the Rayleigh curve $\simeq 2.146\sigma$ (Ref 7:131)

and is 90% of the population is encompassed by the 0.25 deg solid angle

therefore $\sigma = 0.25$ deg/2.146

$\sigma = 0.116$ degrees $= 2.03$ milliradians.

From the summary of the preceeding results (see Table 4.1), it is apparent that a human subject is capable of aiming a helmet-mounted sight at static targets with an accuracy of between 2 and 4 milliradians. After reviewing the four experiments, it can be shown that both Reichwein and Verona used the more sophisticated and accurate error measurement techniques. This fact combined with the possible corruption of Hughes' results due to the suspension system used to support the asymmetric helmet weight, indicates that the actual sighting error of a pilot for static targets may be closer to the 2 milliradian figure. Therefore for the purposes of this model the LANA pilot will be considered able to aim at static targets with an accuracy of between 2 and 3 milliradians, one sigma. The actual value of static aiming accuracy was selected to be 2.6

milliradians, one sigma value. This value was determined from

Nicholson's dynamic accuracy data described later in this chapter.

TABLE 4.1

Summary of Static Target Aiming Accuracy Results	
Source	Aiming Error, Expressed as a Standard Deviation of the Circular Distribution
Nicholson (Ref 11)	3.465 milliradians
Hughes (Ref 10)	3.724 milliradians
Verona et al. (Ref 12)	2.120 milliradians
Reichwein (Ref 13)	2.033 milliradians

Dyanmic Sighting Accuracy

From the preceeding section it is apparent that reasonably high

levels of aiming accuracy are possible, for static targets, while using

the helmet-mounted sight. The objective of this section is to review the

experiments which have been conducted to measure how accurately a subject

was able to track moving targets, using the large and small muscle groups

of the neck and shoulders.

Pursuit tracking is the tracking mode used in the majority of the

experiments, and is "similiar" to the tracking mode(s) that are expected

to be used in the LANA system. Pursuit tracking is best illustrated by a

ground-to-air gunnery situation. The gun crew is fixed in one location

while the target aircraft traces either a predictable or evasive path

from one line-of-sight (LOS) to another. The gun crew's task is to place

the weapon's reference mark over the target and keep it in close

proximity during the tracking and firing sequence. The task of the pilot

in the LANA system is to track stationary ground targets from his moving

cockpit. As the target passes through his field-of-view (FOV), he must

take one or more "fixes" or sightings of the target using his

28

helmet-mounted sight reticle (Ref 5).

It is important to note that his task is not exactly the same as that of the gun crew. While the gun crew must continuously track his target, the LANA pilot instead attempts to align his reticle with the target, as accurately as possible, at some point(s) in time along it's path, and fix or "pickle" the target. This difference between the continuous pure pursuit tracking mode and the sight and pickle mode is of vital interest, since most of the experimental data in the literature involves measuring man's ability to use the helmet-mounted sight in the pursuit tracking mode. This means that when the subject is instructed to employ a pursuit tracking mode, his aiming errors are not necessarily the same as those that would be generated if he were simply instructed to take one or more fixes of a moving target, only when he thought he was on target. We would expect that the aiming errors for the sight and pickle mode will be less than those for the continuous tracking mode, since the operator can determine the instant at which he declares he has a valid sighting. The sight and pickle mode is expected to be the aiming method adopted by the LANA pilot.

Since the target is a stationary landmark, then the movement of the target as seen from the pilot's point-of-view in the cockpit, is a very predictable path. Depending upon the maneuvers that the aircraft is making, the target path will be straight or slightly curving. The angular rates of the target are rarely greater than 20 degrees/second and are normally less than 10 degrees per second. It is expected that the sighting errors for a target moving at low angular rates along a predictable path will be substantially smaller than errors that arise from tracking an evasive target which is moving at high angular rates,

such as is found in the air-to-air combat environment.

Sighting Modes-Dynamic Targets. Furness (Ref 6), in studies conducted at the Royal Aircraft Establishment, found that pilots developed a different tracking mode, as compared to the pure pursuit mode, when asked to align and pickle targets that were moving at angular rates below 20 degrees per second and moving along a predictable path. The pilots, once they gain experience at performing this task, tended to develop sighting modes which are a function of the angular rate of the target. These are the modes that the pilot adopts when he is given instructions to pickle a moving target, one or more times during a sighting run and he is allowed to choose his own tracking method. The sighting modes suggested by Furness are as follows:

Target Angular Rate	Sighting Mode
0 to 2 degrees/second	The same aiming mode as used for static targets, with aiming errors of the same type and magnitude as the static target.
2 to 5 degrees/second	Pure pursuit tracking mode, aiming errors that are zero mean with the standard deviation of the errors increasing linearly with angular rate.
5 to 10 degrees/second	Pilot leads the target by a constant amount, i.e. a fixed bias with random oscillations about the aim point.
10 to 20 degrees/second and above	The pilot aims ahead of the target and waits for the target to pass through his aim point; as the target passes

30

he pickles it. The aiming errors
are zero mean and the standard
deviation of the error increases
linearly as the angular rate increases

Unfortunately, estimates of the magnitudes of the bias and standard deviations of the errors for each of these modes are not available in the open literature. Therefore it is necessary to develop estimates of these values from the results of experiments conducted to measure man's ability to aim a helmet-mounted sight at a moving target. Despite the fact that the majority of these experiments required the subject to employ the pure pursuit mode at all times, these data can be adapted to provide reasonable estimates of the aiming errors for the sight and pickle modes suggested by Furness.

Dynamic Sighting Experiments. Nicholson (Ref 11) conducted laboratory and flight test experiments to measure man's ability to sight moving targets. The targets moved along predictable paths which ran parallel to the subject's forward line-of-sight. The target's linear speed was constant, while the target movement with respect to the subject resulted in target angular rates of between 2 and 68 degrees per second. This type of target motion relative to the observer is remarkably similiar to the expected motion of the landmark in the LANA system with respect to the aircraft. The landmark will be sighted initially off the nose of the aircraft and as the aircraft flies towards and past the landmark the apparent motion of the target will increase in angular rate.

The results of the laboratory tests are shown in Figure 4.1. This plot of the standard deviation of radial error versus target angular rate shows the decrease in performance as the angular rate increases. The

31

broken line is Nicholson's least squares fit curve to the data. These laboratory results are very important, since they measure only the human aiming error, free from environmental conditions, that results from aiming at a moving target. Environmental factors such as vibration and G-forces are not present to corrupt the results.

In Figure 4.2 the same data points as shown in Figure 4.1 are used, except that a piecewise linear curve fit has been performed to the data over the specific angular rate intervals that Furness suggested for the sight and pickle aiming model. These curves were found by performing a linear regression on the data points that extend over each of the angular rate intervals. The piecewise linear fit assumes no jump discontinuities at the boundaries of the intervals. It can be seen from these curves that although there are too few data points to be conclusive, the data can also support the four distinct sight and "pickle" aiming modes predicted by Furness.

The flight test phase of Nicholson's experiment had an extra data measurement feature that the laboratory tests did not have. The pilot was provided with a button with which he was instructed to pickle or designate the target when he thought he had his sight perfectly aligned with the moving target. Figure 4.3 is typical of the flight test plots that were made for all subjects. The solid irregular line represents the pilot's tracking error, i.e. the continuous error of the sight with respect to the position of the target. The circles on this line represent the pickle points, i.e. the instants in time that the subject thought he was on target. The smooth broken curve represents the target line-of-sight angular rate versus time, for each pass and are read off the right ordinate of the chart. Nicholson found that, on the average,

32
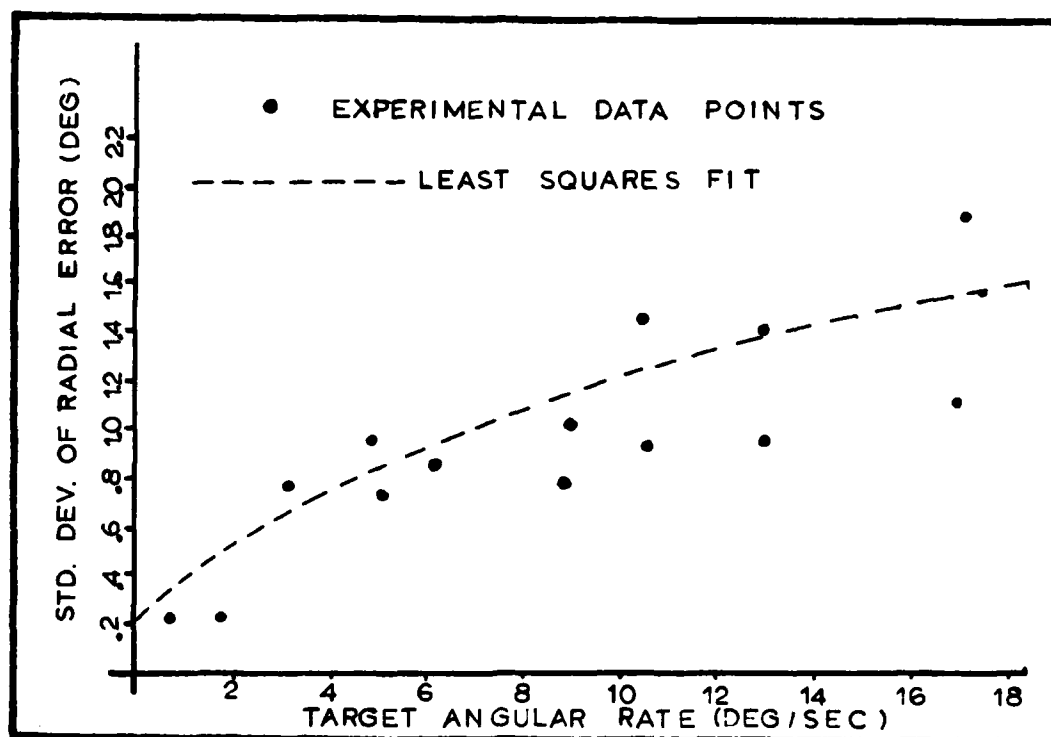
Figure 4.1   Aiming Error vs. Target Angular Rate -
Laboratory Test Data (Ref 11:421)
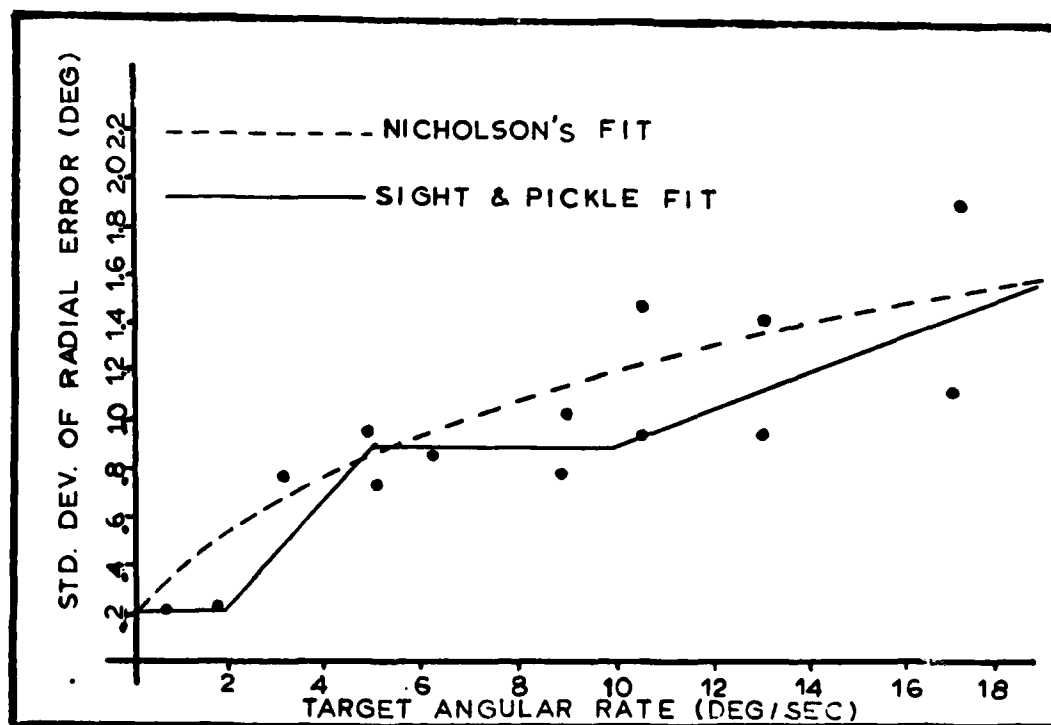
Figure 4.2   Aiming Error vs. Target Angular Rate -
Sight and Pickle Modes Fit to Nicholson's Data

33

FLIGHT 2 - PASS 6

Velocity = 500 Knots
Altitude = 300 Feet
Offset = 500 Feet

Radial Error - Degrees

Target Angular Rate - Degrees/Second

Time - Seconds
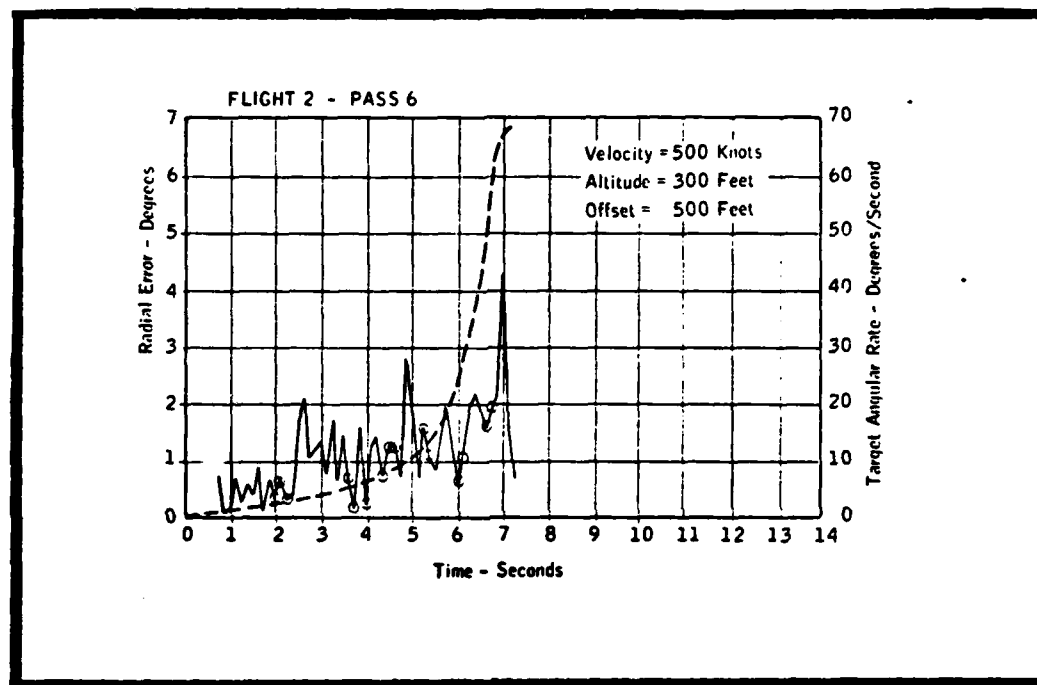
Figure 4.3 Typical Data From Flight Test Illustrating Radial Error (in degrees) as a Function of Time and Target Angular Rate. Flight Conditions are noted on the Figure (Ref 11:423)

after removing the constant error from the data, that the standard deviation of the pickled frames versus the tracking frames were:

Standard deviation of radial   3.0 degrees (52.36 mr)
error - tracking line

Standard deviation of radial   1.9 degrees (33.16 mr)
error - pickled points

Because these errors are corrupted by environmental conditions and therefore are not representative of the sighting ability of the subject alone, the magnitude of the error is not of interest. However, the relative change in the standard deviation of radial error between the tracking and pickling line of Figure 4.3 is significant. If we can assume that a reduction in the standard deviation of radial errors equivalent to that seen in the flight test data of Figure 4.3, would also occur had the subject's in the laboratory tests been able to "pickle" the targets, then by reducing the magnitude of the radial errors in the plots of Figure 4.1 and 4.2 we can generate a more representative estimate of the errors made during the tracking tasks of interest. Using this assumption, the reduction of approximately 37% from the tracking mode to the pickling mode can be used to convert the laboratory data from the pure tracking mode in Figure 4.1 to data which approximates the sight and pickle mode. Figure 4.4 shows the data points of Figure 4.1, and the sight and "pickle" aiming curve from Figure 4.2, both reduced by 37%. This curve now represents the aiming ability of the subject against moving targets using the sight and "pickle" aiming mode.

The experiment conducted by Verona et al. (Ref 12), described in the static aiming section of this report, measured man's ability to aim a helmet-mounted sight at targets moving at an angular rate of 4 degrees per second. The sighting errors for the subjects were

Moving Target (4 deg/sec)   10.5 milliradians of RMS radial
Static Subject   sighting error (Ref 12:45)

Now, converting this result to the circular distribution standard

deviation values using the conversion of Chapter III, gives

$$RMS_{\bar{R}} \text{ (at .4 deg/sec)} = 10.5 \text{ milliradians}$$

using $RMS_{\bar{R}} = 2\sigma$, assuming $\sigma_{AZ} = \sigma_{EL} = \sigma$

$$\sigma = 7.42 \text{ milliradians}$$

In 1970, a study was conducted by Hughes et al. (Ref 10), to measure

the tracking capabilities of the human against stationary, predictable

path and evasive path moving targets. The predictable path targets moved

in either a straight line from one quadrant to another or a slightly

curved path across the subject's sighting area. The evasive targets

traced a path that made three or more random changes in bearing, of

between 90 and 270 degrees. Since this experiment was designed to

measure the change in performance between tracking predictable and

evasive targets, all the sighting accuracy data was collected at a single

value of angular rate. The angular rate of movement of the target with

respect to the subject was held constant at 6 degrees per second, for

both the predictable and evasive targets. After removing the constant

error or bias, the results were expressed as a standard deviation of

radial error (σ_R). These aiming errors are shown in column one of Table

4.2. Column two shows the same errors expressed as a standard deviation

of the circular distribution, assuming the error probability density

function is isotropic. Column three gives the comparitive values from

Nicholson's results at the 6 degree per second angular rate. These

values were read from Figure 4.4 and converted from the radial error to

circular distribution representation of standard deviation.

36
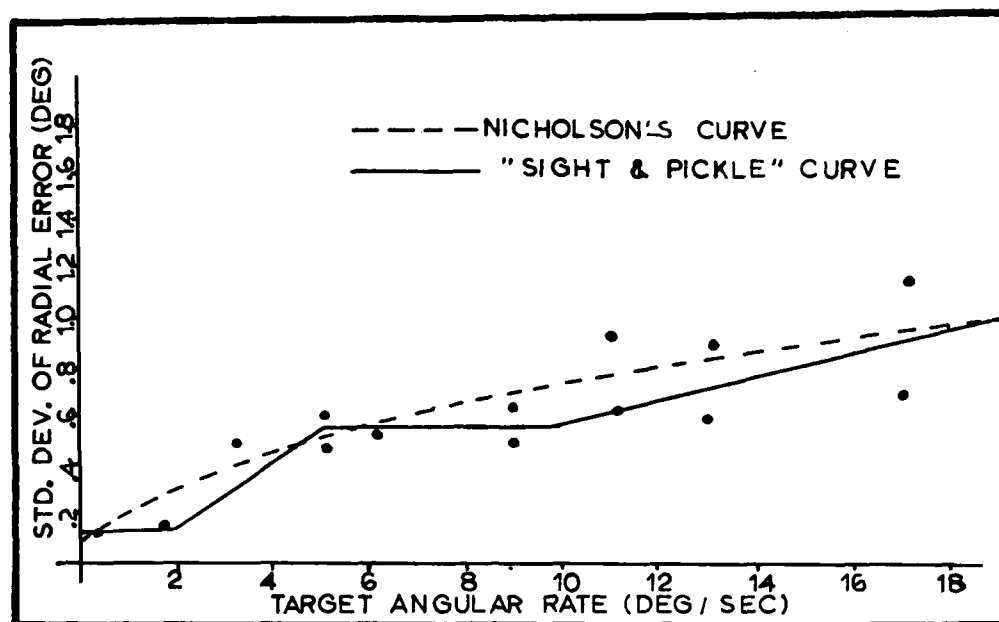
Figure 4.4   Data Points and Curves from Fig. 4.2 Reduced by 37%
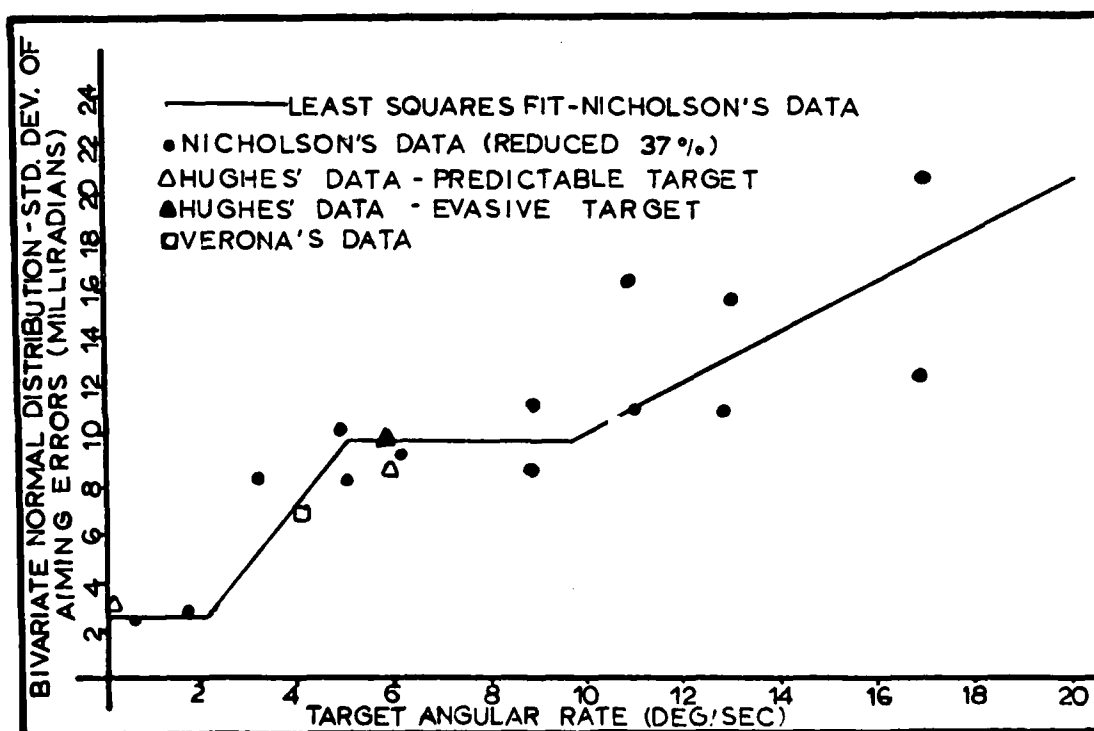
Figure 4.5   Aiming Error vs. Target Angular Rate – Sight and
Pickle Fit, and Other Experimental Data Points

TABLE 4.2

Dynamic Sighting Accuracy, Comparison of Hughes and Nicholson Results
(Ref 10:23)

Target Type	Std. Dev. of Radial Error σ_R mr.	Circular Distribution Std. Dev. of Aiming Error (σ)	Nicholson's Results Std. Dev. (σ)
Static	2.44 mr	3.72 mr	2.6 mr
Predictable Path (6 deg/sec)	5.81 mr	8.87 mr	9.7 mr
Evasive Path (6 deg/sec)	6.54 mr	9.99	*

* Nicholson did not evaluate with evasive targets.

Figure 4.5 is a plot of the data points and curves from Figure 4.4 with the aiming errors converted from the standard deviation of radial error (σ_R) to standard deviation values for the circular normal distribution. The data points from the Verona and Hughes experiment have been added to this plot. Although the results from Hughes and Verona are limited to a singe angular rate, the close agreement with Nicholson's results are remarkable. The curves of Figure 4.5 can be used to develop a model for the pilot sighting accuracy for dynamic targets. The least squares fit to the reduced data as shown in Figure 4.5 was performed as a linear regression to fit the data in each angular rate segment, using an HP-41Cv program (Ref 37). The results of this linear fit, with ω being the magnitude of the target angular rate (ω) measured in deg/sec, are:

$$
\sigma(\omega) \begin{cases} \sigma_1 & 0 \leq \omega \leq 2 \\ \sigma_1 + k_1 \cdot (\omega - 2) & 2 < \omega \leq 5 \\ \sigma_1 + k_1 \cdot (3) + k_2 \cdot (\omega - 5) & 5 < \omega \leq 10 \\ \sigma_1 + k_1 \cdot (3) + k_2 \cdot (5) + k_3 \cdot (\omega - 10) & 10 < \omega \end{cases}
\tag{4-1}
$$

where $\sigma(\omega)$ is the bivariate normal distribution standard deviation of the aiming errors as a function of the target angular rate (ω).

$\sigma_1 = 2.6$ milliradians

$K_1 = 2.54$

$K_2 = -0.055$

$K_3 = 1.15$

assuming $\sigma_{Az}(\omega) = \sigma_{El}(\omega) = \sigma(\omega)$

Aiming Accuracy as a Function of Sighting Angle

A number of studies designed to measure man's tracking abilities also investigated the subject's head aiming performance at various sighting angles, or look angles, away from the straight ahead position. In 1966 Nicholson (Ref 11) found that the radial sighting error was a function of both the angular rate of the target and the pilot's sighting angle, the angle between the aircraft's heading and the pilot's line-of-sight. His data showed that as the off-boresight sighting angle increased, from 0 deg to 90 deg, the magnitude of the sighting errors also increased. During a study completed in 1974, Grossman (Ref 15) found that in his "Flight Evaluation and Pilot Sighting Accuracy" experiment, that the sighting errors were greatest at very small and very large off-boresight angles, i.e. at 0 degrees and 150 degrees, and the smallest errors were at the 90 degree angle.

The findings of these two experiments and other similiar studies frequently contradicted each other. In an effort to resolve these differences, Monk et al. (Ref 16) conducted an experiment at the Air Force Aerospace Medical Research Laboratory to evaluate head tracking at

39

large angles from the straight ahead position. The subjects were asked

to track a randomly moving target at angular rates of up to 45 degrees

per second, over a field-of-view of $\pm$ 55 degrees in azimuth and $\pm$ 45

degrees in elevation. Monk found that there is no practical difference

in man's sighting accuracy as a function of his look angle, and that a

pilot is able to aim his helmet-mounted sight as accurately at any

sighting angle as he can at the straight ahead position.

To explain why Nicholson and Grossman did not reach the same

conclusions, the equipment used in these early experiments must be

examined. Apparently, the accuracy of the early versions of the

helmet-mounted sight could change as the helmet pointing angle was varied

in azimuth or elevation. This change in sight acuracy as a function of

the sighting angle is dependent upon the headware used at the time, and

serves to explain the contradictory findings (Ref 6). In contrast the

latest version of the Polhemus helmet-mounted sight that was used by Monk

in 1978, has statistically constant error over the entire range of the

azimuth and elevation angles.

Monk was careful to point out that pilot sighting accuracy is only

independent of his look angle when he is in a normal one G-positive

acceleration environment. Under G-loads the neck and shoulder muscles

which support the head are unable to support the extra weight of the head

equally at all sighting angles, and the aiming accuracy of the pilot

becomes a function of his azimuth and elevation sighting angles (Ref 17).

Effects of +Gz on Aiming Accuracy

In 1970, Reichwein (Ref 13) conducted an experiment to measure the

effects of steady-state +Gz accelerations on a subject's ability to aim

a helmet-mounted sight at stationary targets located at four extreme positions in his field-of-view. The +Gz direction is defined as the longitudinal direction of the spine, in the seated subject. An F-4 cockpit was located in a human centrifuge and the +Gz conditions ranged form 1 G to 4.5 G. The targets were mounted inside the cockpit and positioned as illustrated in Figure 4.6. The structure of the F-4 and the visual display prevented the placement of a target at the 0 deg azimuth - 0 deg elevation position. The subject's performance was measured as a percentage of time on target for each trial. An example of the results for the six subjects, sighting on target number one is shown in Figure 4.7. The individual scores versus the G-level are plotted and the least square error regression line is indicated. The drop in scores between the pre-test condition and the 2 G values can be almost entirely attributed to the vibrational motion of the centrifuge, since both the pre-test and post-test scores were obtained while the centrifuge arm was stationary. Therefore, the least squares regression was only computed for the dynamic run data.

The negative slope of the regression line indicates a decrease in aiming performance as the G-level increases. Subject variability is demonstrated by the plot of subject number five's plot in Figure 4.7, where he shows an increased accuracy as the acceleration level increase. This variability between subjects is a problem whenever measurements of human response or abilities are involved. Reichwein determined that the subject's aiming performance was poorest for elevated targets and best for eye-level targets. He indicates that a qualitative interpretation of the data is more appropriate than a quantitative interpretation for several reasons. The experiment was preliminary in nature, there were a

41
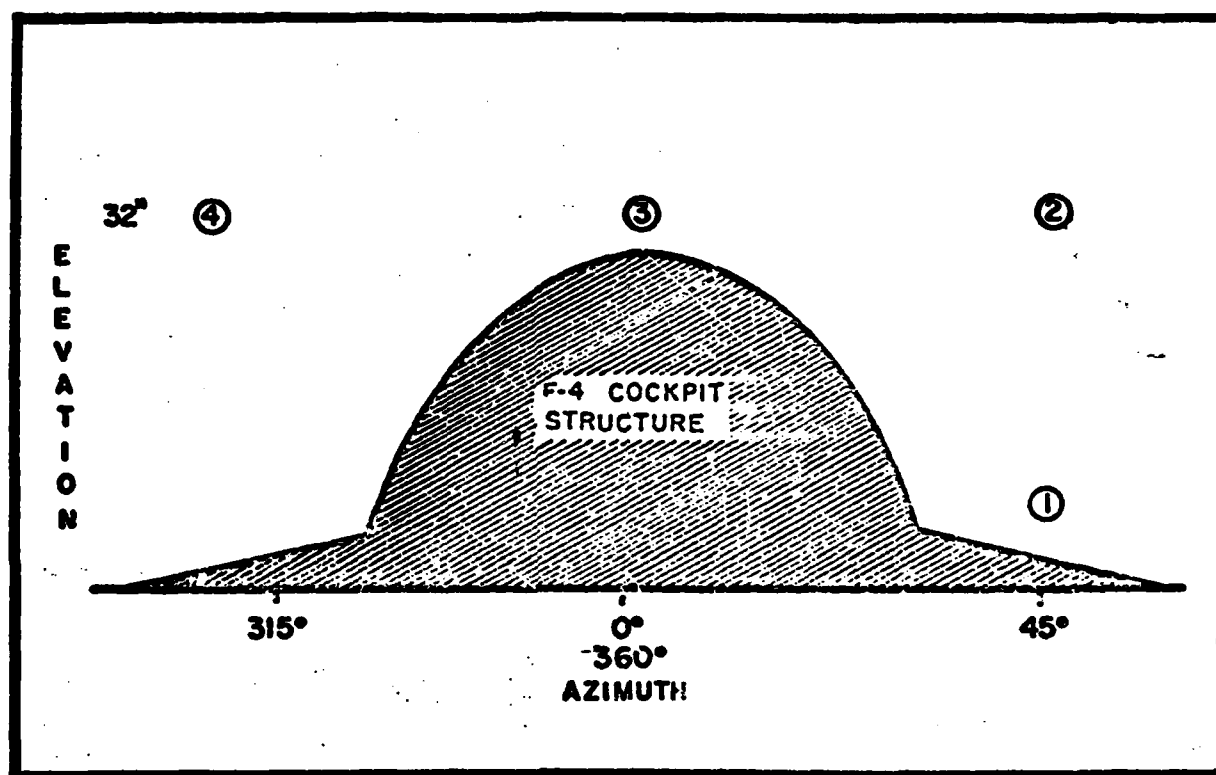
Figure 4.6   Target Position in Gondola (Ref 13:6)
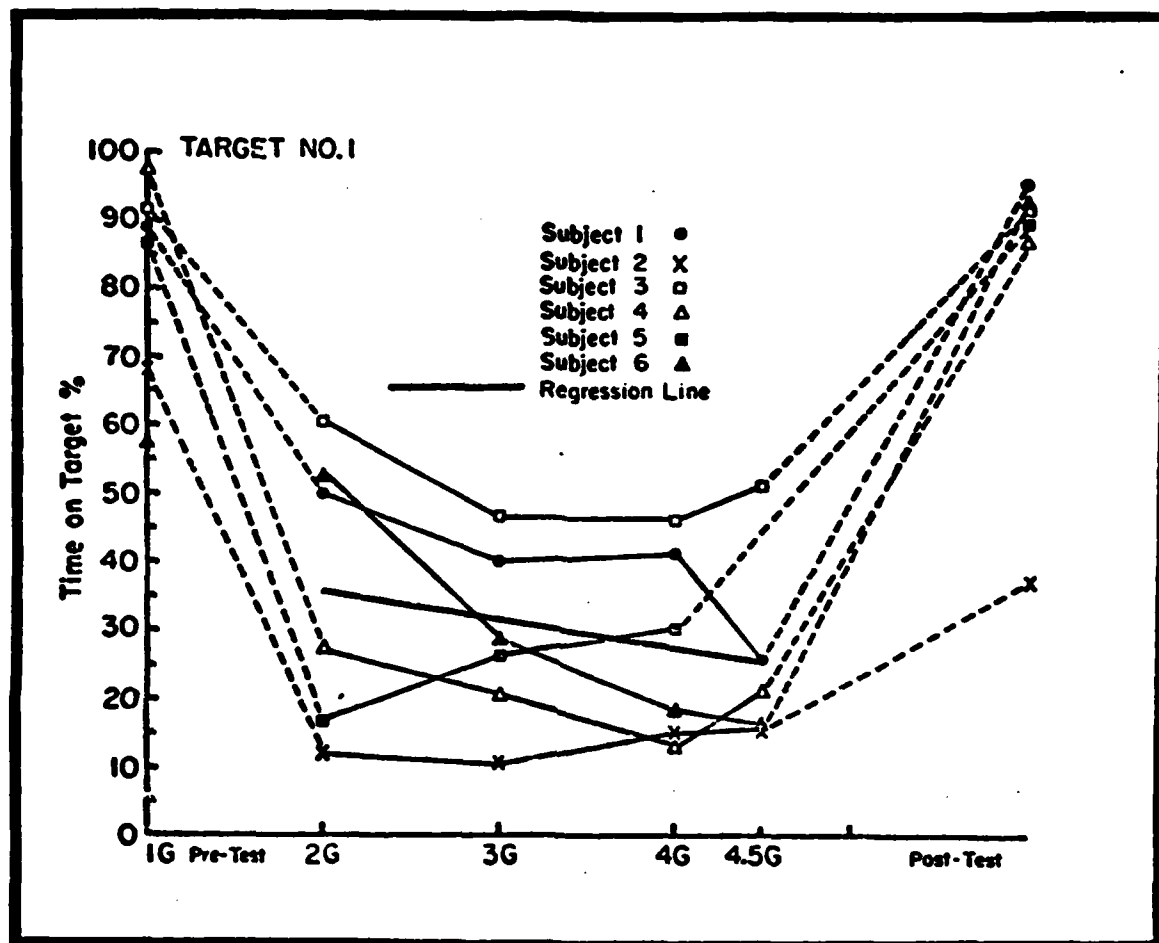
Figure 4.7   All Subject's Aiming Performance
versus $+G_z$ – Target 1 (Ref 13:14)

limited number of targets available, and the helmet-mounted sight used
was neither the type or weight of one that would ever find its way into
an operative system. He concluded from these tests that although aiming
performance does degrade as the G-levels increase, the loss in accuracy
is not as large as might be initially expected. He estimates that
performance is degraded by 8 to 10 percent, per G-level, depending upon
the azimuth and elevation look angles.

Unfortunately, this experiment is the only published study of aiming
accuracy under G-forces in the open literature. The data from this
experiment is insuffiient to use as a basis for a model of the
acceleration induced aiming errors. An evaluation of the proposed
trajectory for the LANA mission and the actual trajectory data used in
the LANA simulation indicates that there are minimal G-forces on the
pilot during those periods in which he is taking position measurements.
Since the pilot can control the amount of "G" he is pulling, it is
assumed that normally he will be taking measurements with the
helmet-mounted sight under the nominal one-G condition. Given this
assumption, and the fact that the effects of acceleration on aiming
accuracy are small, then this source of error will not explicitly
modeled. This error source will be treated as part of the additive
measurement noise which is included in each measurement to account for
the unmodeled errors.

Human Operator Error Model

The laboratory and flight test experiments which were designed to
quantify the aiming accuracy of the human operator have provided the
answers to most of the questions that were posed at the beginning of this

44

chapter. Briefly the answers to these questions are as follows:

1. The human can aim a helmet-mounted sight at static targets with accuracies of between 2 and 3 milliradians. The actual value was set at 2.6 milliradians expressed as a one sigma value.

2. The dynamic or moving target accuracy of the operator is a function of target angular rate. The pilot aiming errors, at any given target angular rate, can be modeled using Equation 4-1. From Figure 4.5, it can be seen that the pilot's aimng error varies from 2.6 milliradians at an angular rate of zero degrees per second, to approximately 20 milliradians at an angular rate of 20 degrees per second.

3. Monk's experiment demonstrated that the pilot's off-boresight azimuth and elevation look-angles do not effect his sighting accuracy.

4. Research has shown that the pilot's aiming accuracy is impaired by acceleration or G-forces that are experienced in flight. The precise nature or magnitude of this impairement has not been adequately studied. Thus an accurate model of this error source cannot be formulated at this time.

5. The effects of stress-level on workload upon the pilot's sighting accuracy were assumed to be inherent in the experiments conducted under actual flight test conditions. In addition stress was induced by allowing the experimental subjects a relatively small time span to perform the sighting task.

Fróm the above conclusions a model of the human operator's contribution to the LANA system measurment error can be developed. The

45

relationship for aiming error as a function of target angular rate, given by Equation 4-1 forms the basis for this model. This equation can be used to determine the value of the standard deviation of the azimuth and elevation aiming error, assuming the errors have an isotropic circular distribution. At this point it is appropriate to point out that an adequate model for the human operator errors could have been developed by simply using the Nicholson's curve of Figure 4.1. Even by ignoring the sight and pickle sighting modes, the differences are small between using Nicholson's curve as a model and the more elaborate sight and pickle model. The reasons for using the sight and pickle model were to demonstrate that the available data in the literature can support this sighting hypothesis and to stimulate further research in this area. The azimuth error is a function of the azimuth component of the target's angular ra   d the elevation error is a function of the elevation component of the target angular rate. The values of azimuth and elevation error standard deviation will be used by the subroutine GAUSS in SOFE to generate random numbers having zero mean and a standard deviation value matching that value given by Equation 4-1. These random numbers will be added to the azimuth and elevation components of the measurement at each measurement update cycle to model the corrupted, true measurement.

V Errors Due to Canopy Refraction

The requirement for good pilot visibility dictates that the optical quality of aircraft canopies must be maintained while meeting the stringent requirements imposed by high-speed flight.

While the optically ideal canopy is a flat plate, good aerodynamic performance requires canopies that are inclined at low angles and have curved surfaces. While these canopies provide a large unobstructed field-of-view, they have undesirable optical effects and the optical quality suffers due to their multi-layer construction. The optical effects produced include changes in both position and magnification of any object when viewed through the canopy (Ref 11:5).

Since the LANA concept uses a helmet-mounted sight (HMS) to take position sightings, the presence of the canopy between the HMS and the target will degrade the accuracy of the sighting. Thus an accurate model of the LANA helmet-mounted sight system must account for these canopy induced errors.

Angular Deviation

There are a number of optical phenomena which can occur when objects are viewed through a transparent material. Some of these include angular deviation, haze, multiple images, rainbowing (birefringence), and distortion. Although any one of these may effect the pilot's ability to locate a target, it is only the angular deviation effects which result in sighting errors. Angular deviation is defined as the angular change of direction of the light ray, caused by the bending or "refraction" of that ray as it passes through a transparency (Ref 6:8). Distortion is often described as the rate of change of angular deviation.

Whenever a ray of light passes through a transparency at any angle other than the normal (a "normal" is a line drawn perpendicular to the transparency surface), several events occur (See Figure 5.1). One of these events results in the lateral displacement of the ray by a relatively small amount. This lateral displacement is usually operationally insignificant beyond a few meters. A second event causes the light ray to undergo an angular direction change. This angular error can be quite significant when considering its effect on apparent target position as seen by the pilot. For each milliradian (mr) of error, the target's true position will be displaced from its apparent position by 1 foot for each 1000 feet of range. In other words, a transparency inducing a 10 mr error will move the apparent position of a target, located 3000 feet away, by a distance of 30 feet (Ref 6:9).

Angular deviations can also be caused by relatively local areas of non-parallellism of the surfaces of the transparency. Figures 5.2, 5.3, and 5.4 show examples of some of the angular deviation effects produced by aircraft canopies.

Canopy Measurement Techniques

Current manufacturing techniques attempt to minimize the amount of angular deviation in the forward area of the canopy. As shown in Figure 5.5, it is through this portion of the canopy that the head-up display (HUD) and the weapons sighting accuracy is critical. It is important to note that in the LANA system the HMS sighting area is not restricted to this small area of the canopy, and potentially any area of the canopy could be interposed between the HMS and the target.

Currently, all HUD equipped aircraft have their forward windscreens

48
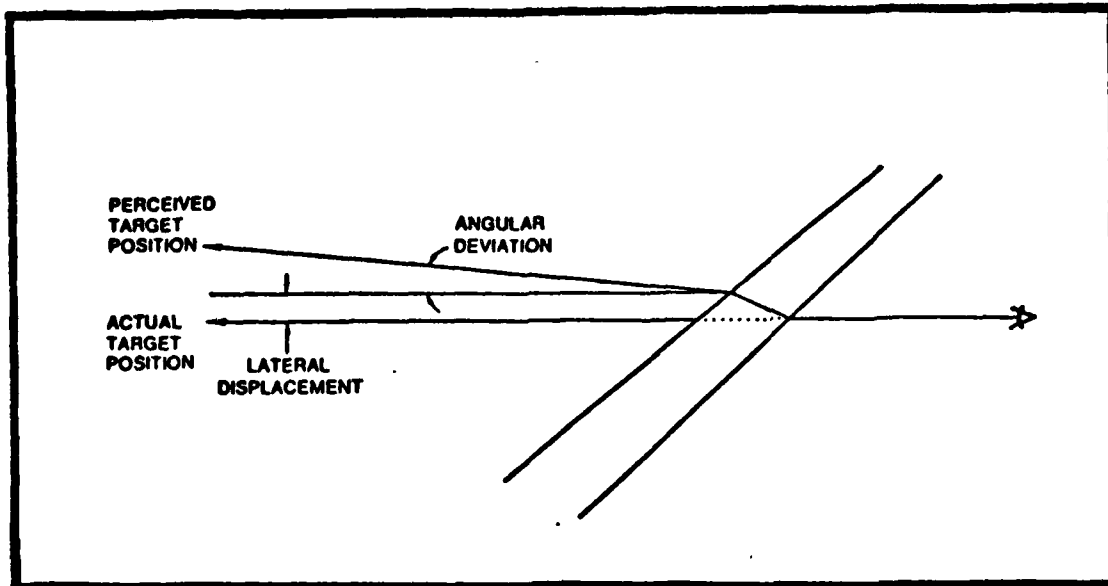
Figure 5.1   Lateral Displacement and Angular Deviation
Effects of Aircraft Canopies (Ref 19:8)
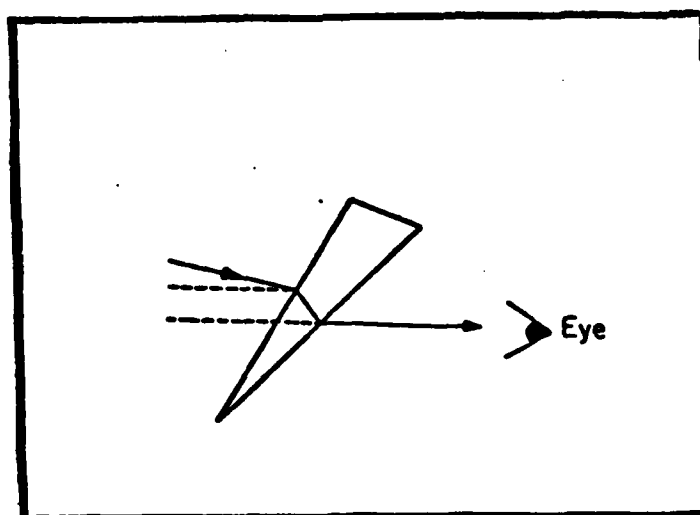
Figure 5.2   Angular Deviation and Displacement Produced
by Prismatic (Wedge) Errors (Ref 18:6)
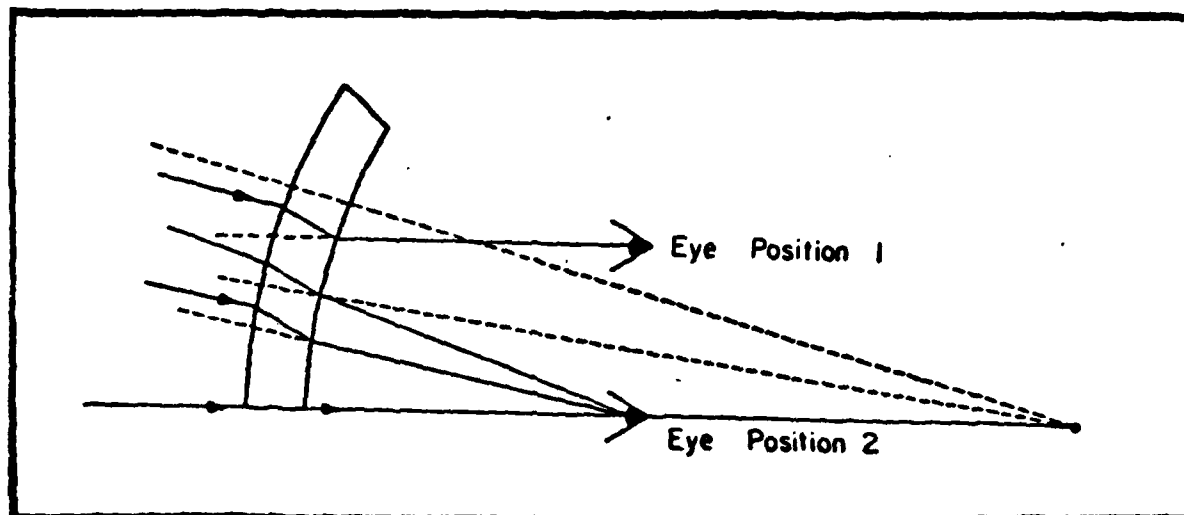
Figure 5.3   Canopy Curvature Producing Angular
Deviation and Displacement (Ref 18:6)
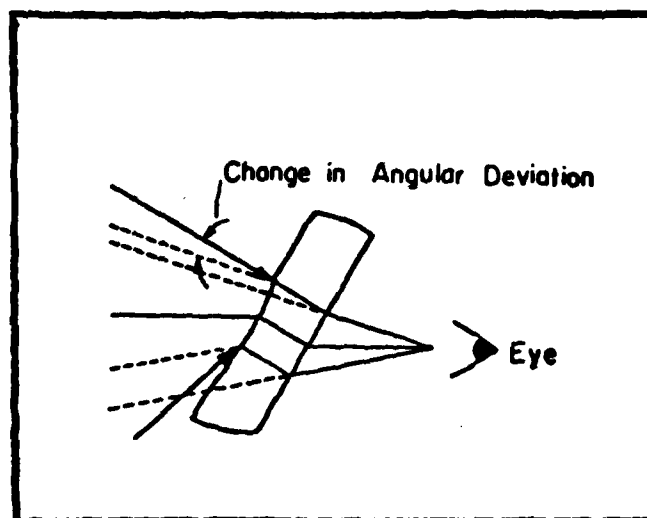
Figure 5.4   Localized Variation in Canopy Shape Producing
Angular Deviation and Displacement (Ref 18:6)

AREA OF CANOPY "SEEN" BY HUD (TOP VIEW)

AREA OF CANOPY "SEEN" BY HUD (SIDE VIEW)
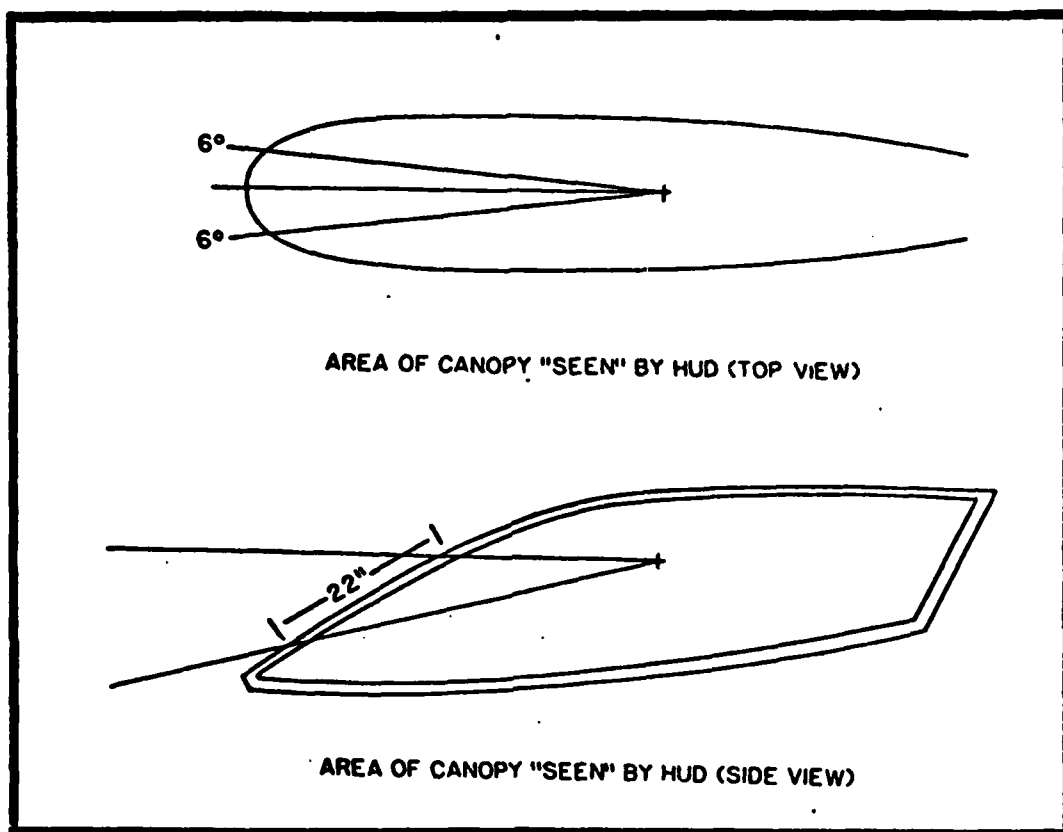
Figure 5.5   Head-Up Display (HUD) Field-of-View (FOV)   (Ref 18:37)

(or canopies) measured to determine their angular deviation, or induced aiming error. Standards have been set to accept only those canopies which cause little aiming error, and at least one aircraft HUD fire control computer is provided with a means to compensate for the remaining error. In the F-16 case, the Air Force has specified that the HUD field-of-view area of the canopy shall have no angular deviation in excess of 3 milliradians (mr), and the Root Mean Square (RMS) average of the error within a single canopy will not exceed 1 mr after compensation from a calculated baseline (Ref 19:10).

Angular Deviation Measurement

The Air Force Aerospace Medical Research Laboratory (AFAMRL), has developed a very accurate yet simple electro-optical device which measures the "pure" angular deviation of the aircraft canopy. As shown in Figure 5.6, light from an incandescent lamp is collected by a condensing lens to illuminate the target slide. This collimated light source is positioned such that the projection lens is approximately at the design eye position, or observer position, for the canopy (transparency) under test. The remainder of the system (the receiver) is located on the other side of the transparency. The receiving lens compensates for lateral displacement (thus eliminating that error source) and images the target slide one focal length away. A beam splitter divides the light into two approximately equal intensities, one channel to measure azimuth (horizontal) deviation and one to measure elevation (vertical) deviation. In each channel a segment of the target slide intersects a charge coupled device (CCD) linear array and its associated electronics. The target slide is shown in Figure 5.7. The image of the

52
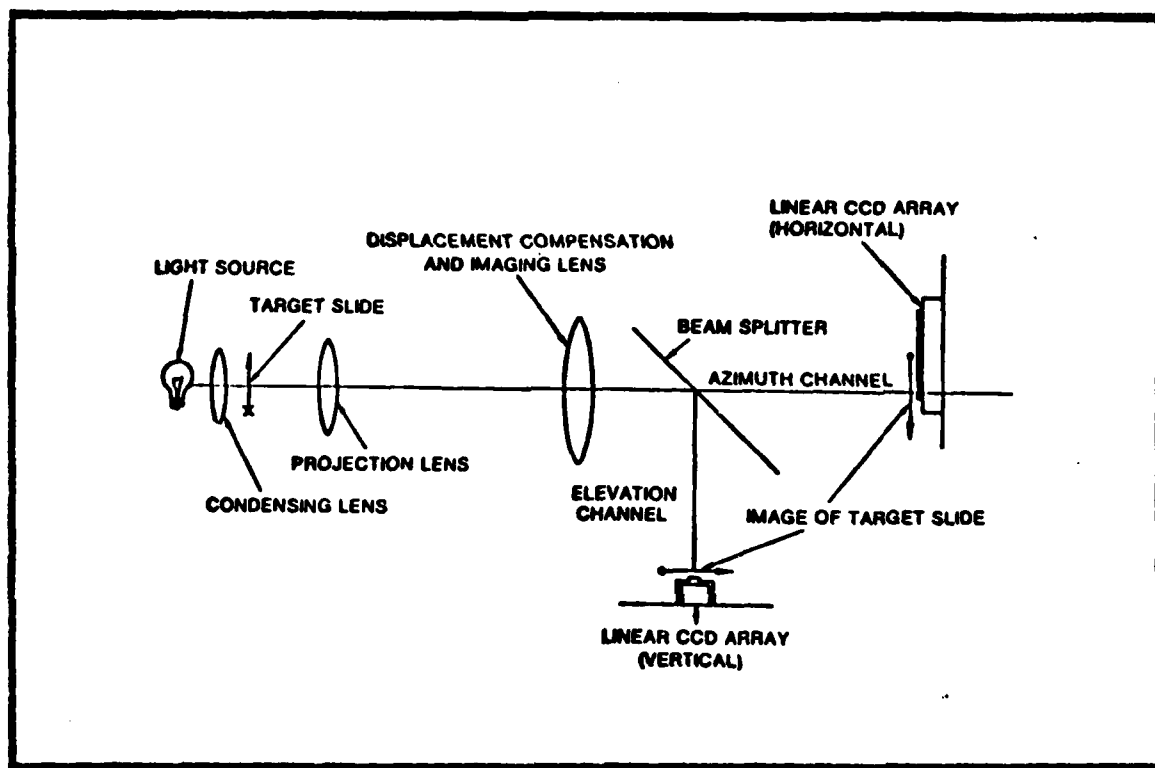
Figure 5.6   Pictorial Layout of Canopy Angular Deviation Measurement Device (the canopy to be measured is positioned between the projection lens and the displacement compensation lens) (Ref 19:13)

"L" is produced at the plane of the CCD array. The array is offset from the optical axis so that one leg of the "L" intersects the azimuth CCD array as shown in Figure 5.8, while the other leg of the "L" intersects the elevation CCD array. The change in position of the individual legs of the "L" between the canopy installed and the no-canopy condition is mathematically related to the angular deviation of the canopy at the point of measurement (Ref 19:14). This system is able to measure angular deviation with an accuracy of 0.07 mr while holding an F-16 canopy in a positioning fixture with an angular position accuracy of 0.1 degree (Ref 19:15)

Modeling Discussion

In order to develop a good model for the canopy-induced errors, we require a means of measuring the magnitude and nature of these errors. Unfortunately, canopy characteristics vary widely between aircraft types, and even canopies for the same type of aircraft are somewhat individual with respect to their angular deviation properties. This fact makes it essentially impossible to develop a good general model to represent the canopy errors. It is for this reason that most helmet-mounted sight accuracy studies ignore this error source; since the data are difficult to generate and use.

However, a reasonable attempt at modeling this error source can be made if two assumptions are permitted. First we assume that the F-16 aircraft is typical of those aircraft which might be used for the LANA mission and second, that a particular F-16 canopy, selected at random, is a typical member of the population of all F-16 canopies. By using a single F-16 canopy from which to take measurements to develop an error

54
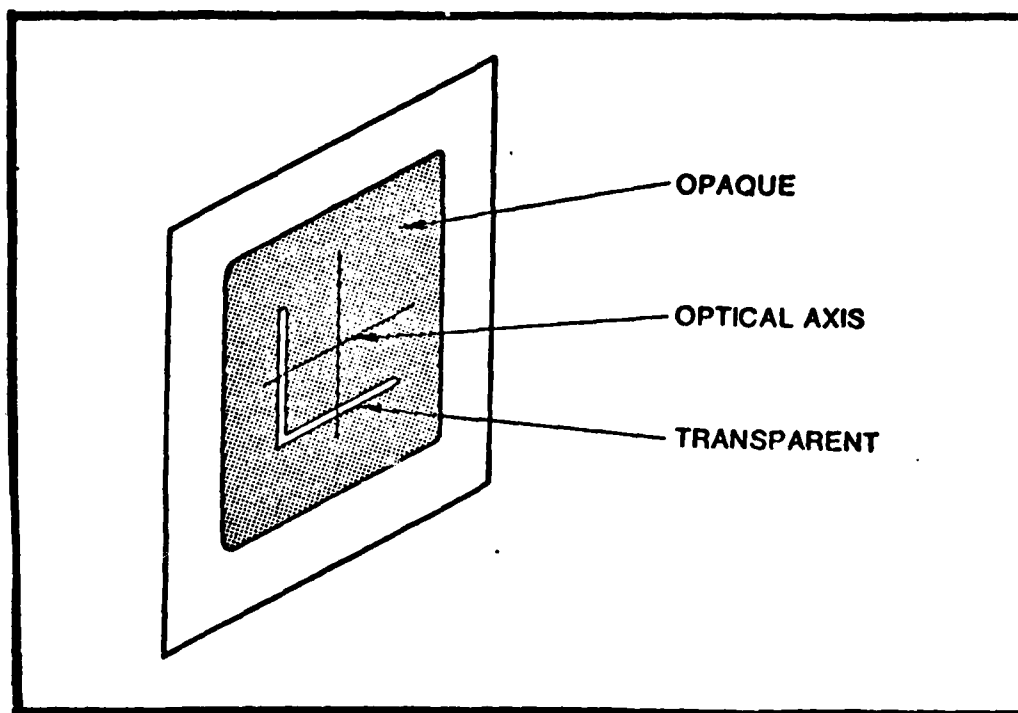
Figure 5.7   Target Pattern for the Projector Half of the
             Angular Deviation Measurement Device (Ref 19:14)
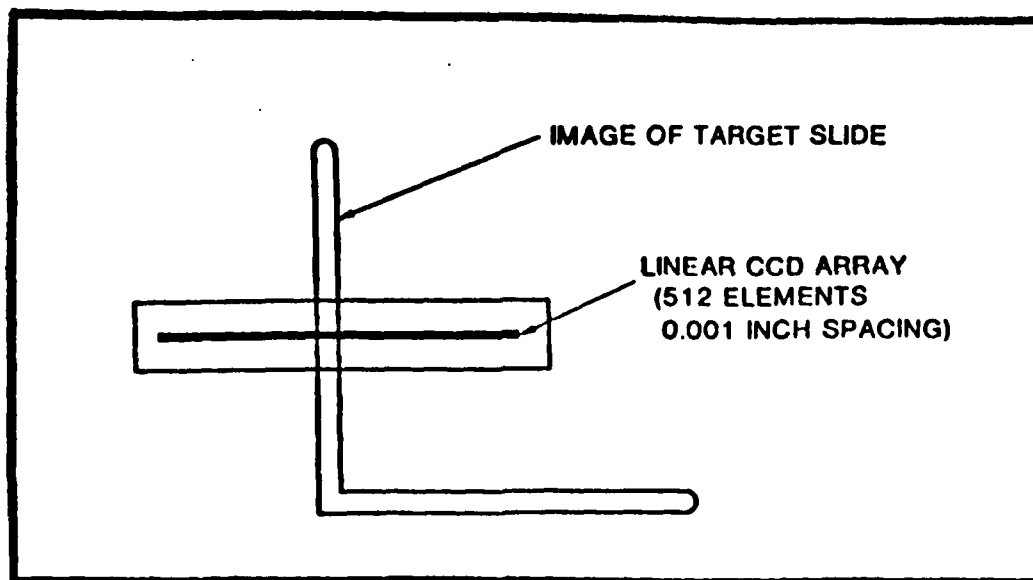
Figure 5.8   Intersection of the Image of the Target Pattern with
             the Vertical Channel of the CCD Array (Ref 19:14)

model, there is a significant risk of producing a point design model. Fortunately, as will be seen later, the compensation techniques used to remove most of the error, also minimizes the individuality of the errors in the canopy, which remain after compensation. In addition, the time constraints on this study and the number of available F-16 canopies precluded taking measurements from more than one sample canopy.

The overall canopy distortion compensation process proceeds as follows. The measurement data from a matrix of canopy locations are used to produce a polynomial curve fit to the data. A separate polynomial is computed for the azimuth and elevation angular deviation data. These polynomials are the calculated baseline used as the compensation curve to remove most of the canopy errors, and as the canopy acceptance criteria.

The polynomial coefficients are affixed to each canopy as "nameplate values" for later input to the HUD Fire Control Computer. These coefficients are intended to allow the computer to offset weapons delivery by an angle equivalent to the angular deviation induced by the canopy, and thus maintain extreme accuracy (Ref 20:13). By using the compensation polynomials, the canopy angular deviation errors are guaranteed to be less than 3 mr, and the root mean square value of all the residual error will be less than 1 mr.

This compensation technique has also removed much of the variability between individual canopies. Although the residual angular deviation errors will differ between canopies at any particular line-of-sight, the magnitude of this residual error will always be within the specified limits. An example of a curve, fitted to earlier measurement data, is shown in Figure 5.9. The heavy line is the best fit curve, while the thin lines are the data from the various eye positions. The polynomial

56

MANUFACTURER: TEXSTAR   C1   1.31096
SERIAL NUMBER: 035   C2   -2.46534
21-JUL-81   C3   20.57142
FIT: A   C4   -50.74121
DATA: AF   RMS(B):   .92675
EYE: CENTER   MAXE: 2.09523

TEXSTAR LAMINATED CANOPY ELEVATION DEVIATION ERROR CURVE.
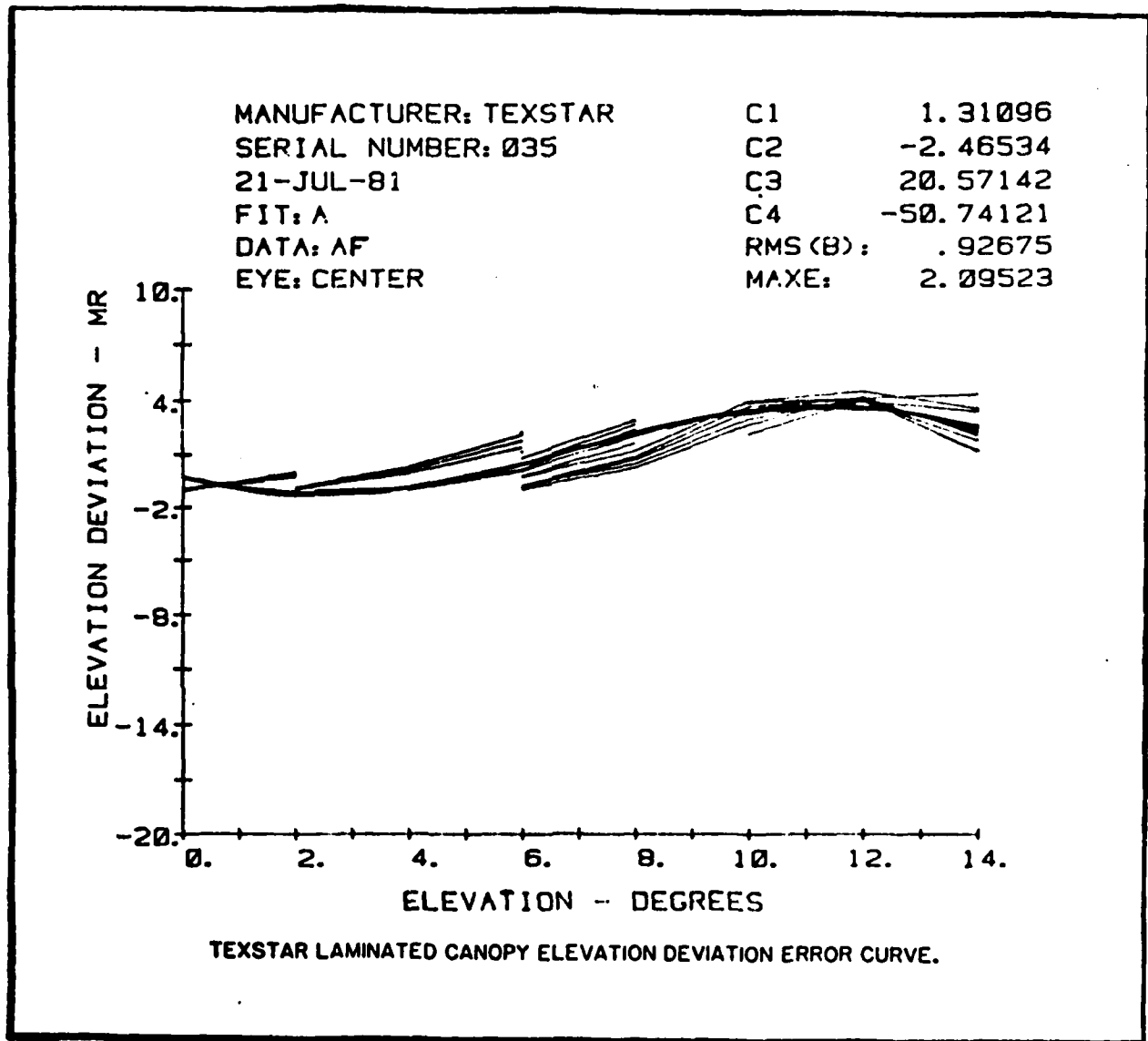
Figure 5.9   Sample Curve Fit of the Elevation Angular Deviation for a Texstar F-16 Canopy. The heavy line is the best curve to the data sequences shown as narrow lines (Ref 20:83

57

coefficients are shown as C_1, C_2, C_3, and C_4. The maximum difference between the best fit curve and the data is shown to be 2.09523 mr, and the RMS average difference is 0.92675 mr.

F-16 Canopy Measurement Experiment

Introduction. Although all the F-16 canopies are measured for angular deviation using the device developed by AMRL, the measurements are only taken over the HUD field-of-view, a relatively small portion of the entire canopy area. Since the LANA simulation is designed to permit line-of-sight vectors over an azimuth range of $\pm$ 90 degrees and $\pm$ 45 degrees in elevation, a more extensive mapping of a canopy is required.

Equipment. The AMRL angular deviation measurement device, as previously described, was used to measure the F-16 canopy. The canopy used in this experiment was canopy serial number 0200, manufactured by the Sierrancin Corporation.

Method. The mapping of the F-16 canopy required that a large number of data points be taken over an area corresponding to the LANA helmet-mounted sight field-of-view. However, the limits of the canopy positioning stand allowed only over a range of $\pm$ 68 degrees in azimuth and $\pm$ 14 degrees in elevation at the design eye position (the expected position of the pilot's eye). If the collimated light projector was moved to the left or right of the design eye position, then the range of movement was further limited.

In order to evaluate the effect on angular deviation of the observer moving off the design eye location, less detailed mappings were also performed at sighting positions to the left, right, and forward of the design eye position. The mapping series were performed as follows:

Series	Sighting Position	Azimuth Range	Elevation Range	Results
A	Design Eye	± 68°	± 14°	see Tables 5.1 & 5.2
B	2.5" Fwd of Design Eye	-44° to +36°	± 14°	see Table 5.3
C	1.25" Right of Design Eye	-68° to +44°	± 14°	see Table 5.4
D	2.56" Right of Design Eye	-68° to +36°	± 14°	see Table 5.5
E	1.25" Left of Design Eye	-44° to +68°	± 14°	see Table 5.6

Results. The results of these canopy mappings are given in Tables 5.1 to 5.6. Each of these tables shows the amount of canopy azimuth and elevation angular deviation in milliradians at each look angle. The look angles are the azimuth and elevation components of the pilot's line-of-sight vector, in the aircraft body frame coordinates. The pilot's line-of-sight originates at the design eye, or measurement position, and passes through the canopy. For example, using Table 5.1, at the design eye position, the canopy angular deviations when the azimuth look angle is -68 degrees and the elevation look angle is +14 degrees are:

Azimuth Angular Deviation: -1.61 milliradians

Elevation Angular Deviation: +5.53 milliradians

These angular deviation data were found to be repeatable at any time, within the accuracy limits of the equipment.

The azimuth deviation values from these tables were then plotted versus the azimuth look angle, and these plots are shown in Figures 5.10 to 5.14. Similarly the elevation deviation values were plotted versus

59

Table 5.2 Canopy Angular Deviation Mapping at the Design Eye Position (continued)

AZIMUTH LOOK ANGLE (DEG)

ELEVATION LOOK ANGLE		4°	8°	12°	16°	20°	24°	28°	32°	36°	40°	44°	48°	52°	56°	60°	64°	68°
14°	A	.49	.49	.84	.84	.84	.98	1.19	1.54	1.82	1.96	2.17	2.31	2.31	2.38	2.38	2.38	2.24
	E	5.88	6.09	6.09	6.02	6.02	5.88	5.60	5.39	5.04	5.11	5.04	5.18	5.18	5.32	5.25	5.53	5.60
12°	A	.56	.63	.91	.56	.63	.63	.70	1.12	1.14	1.75	1.89	1.96	2.03	2.03	2.10	2.10	2.03
	E	5.11	5.53	5.88	5.88	6.09	6.02	5.74	5.53	5.18	5.18	5.11	5.32	5.25	5.18	5.39	5.32	5.53
10°	A	.63	.84	.98	.63	.49	.42	.35	.77	1.05	1.47	1.68	1.68	1.75	1.75	1.82	1.82	1.82
	E	4.48	4.76	5.11	5.39	5.81	5.88	6.02	5.81	5.39	5.25	5.25	5.32	5.39	5.25	5.32	5.46	5.60
8°	A	.70	1.05	1.12	.70	.49	.14	.14	.28	.63	1.05	1.26	1.40	1.47	1.54	1.54	1.61	1.54
	E	4.13	4.20	4.41	4.83	5.18	5.60	5.95	5.95	5.67	5.39	5.32	5.39	5.39	5.32	5.39	5.46	5.67
6°	A	.49	1.12	1.12	.91	.56	.21	0.00	0.00	.28	.63	.91	1.12	1.12	1.19	1.33	1.40	1.26
	E	3.78	3.85	3.85	3.85	4.48	5.25	5.95	5.74	5.60	5.39	5.46	5.39	5.39	5.39	5.46	5.46	5.60
4°	A	.35	1.12	.84	.84	.77	.35	0.00	-.14	-.07	.28	.63	.84	.77	.84	1.05	1.05	1.05
	E	3.01	3.29	3.36	3.22	3.64	4.48	5.25	5.60	5.67	5.53	5.46	5.46	5.39	5.32	5.53	5.46	5.60
2°	A	.77	1.12	.91	.91	.84	.49	.07	-.35	-.42	-.28	.28	.49	.63	.56	.77	.84	.77
	E	1.75	2.31	2.80	2.87	3.22	3.92	4.83	5.25	5.46	5.53	5.39	5.32	5.46	5.46	5.53	5.39	5.60
0°	A	1.12	1.40	1.19	.91	.91	.70	.14	-.35	-.49	-.35	0.00	.14	.21	.28	.42	.56	.56
	E	.14	.98	1.89	2.52	2.94	3.57	4.27	4.90	5.32	5.39	5.25	5.39	5.39	5.46	5.53	5.46	5.53
-2°	A	1.26	1.89	1.75	1.19	1.05	.77	.21	-.35	-.70	-.63	-.21	-.07	0.00	0.00	.21	.28	.28
	E	-1.05	-.35	.49	1.75	2.66	3.15	3.85	4.41	4.97	5.11	5.11	5.18	5.39	5.39	5.53	5.39	5.53
-4°	A	1.33	2.17	2.24	1.75	1.26	.77	.35	-.21	-.84	-.84	-.49	-.28	-.07	0.00	0.00	0.00	0.00
	E	-2.03	-1.68	-.49	.63	2.03	2.87	3.43	3.99	4.69	4.97	4.97	5.18	5.39	5.39	5.46	5.39	5.46
-6°	A	1.68	2.80	2.87	2.45	1.75	.84	.35	-.28	-.91	-1.19	-.77	-.49	-.49	-.28	-.21	-.21	-.14
	E	-3.57	-2.73	-1.26	-.14	1.40	2.52	3.29	3.85	4.48	4.76	4.90	5.11	5.39	5.32	5.39	5.32	5.46
-8°	A	2.10	2.94	3.36	2.84	2.17	1.12	.35	-.14	-1.05	-1.40	-1.05	-.84	-.70	-.63	-.49	-.49	-.35
	E	-2.94	-2.24	-1.68	-.42	.84	2.24	3.01	3.64	4.34	4.48	4.83	4.97	5.25	5.18	5.32	5.25	5.53
-10°	A	1.89	3.15	3.22	3.50	2.59	1.47	.42	-.07	-1.05	-1.47	-1.40	-.98	-.98	-.91	-.77	-.70	-.56
	E	-1.66	-1.54	-1.05	-.49	.77	1.96	2.94	3.29	4.13	4.55	4.62	4.83	5.04	5.11	5.32	5.32	5.46
-12°	A	2.17	3.43	3.15	3.85	2.80	1.68	.42	0.00	-1.05	-1.75	-1.54	-1.19	-1.12	-1.19	-1.05	-.91	-.84
	E	-3.08	-2.31	-.91	-.77	.49	1.16	2.73	3.08	3.92	4.27	4.62	4.76	4.97	4.97	5.25	5.25	5.39
-14°	A	3.43	3.36	3.85	3.71	3.29	2.03	.49	-.77	-1.05	-1.82	-1.75	-1.40	-1.33	-1.40	-1.33	-1.21	-1.05
	E	-4.90	-2.10	-1.40	-.49	0.00	1.33	2.45	2.87	2.71	3.99	4.27	4.55	4.76	4.90	5.16	5.18	5.39

A: Azimuth Angular Deviation (mr)
E: Elevation Angular Deviation (mr)
Canopy: Sierrancin, S/N 0200

61

Table 5.1 Canopy Angular Deviation Mapping at the Design Eye Position

AZIMUTH LOOK ANGLE (DEG)

ELEVATION LOOK ANGLE		-68°	-64°	-60°	-56°	-52°	-48°	-44°	-40°	-36°	-32°	-28°	-24°	-20°	-16°	-12°	-8°	-4°	0°
14°	A	-1.61	-1.47	-1.40	-1.40	-1.26	-1.26	-1.26	-1.12	-.84	-.49	-.07	.28	.98	.91	.98	.77	1.05	.70
	E	5.53	5.53	5.39	5.46	5.46	5.32	5.25	5.18	5.25	5.39	5.60	5.95	6.09	6.51	6.23	6.30	6.02	6.02
12°	A	-1.33	-1.26	-1.12	-1.19	-1.12	-.98	-.98	-.98	-.63	-.28	.07	.63	1.26	1.19	1.05	.07	.98	.77
	E	5.53	5.53	5.46	5.53	5.60	5.46	5.32	5.39	5.46	5.67	5.95	6.16	6.02	6.16	5.74	5.74	5.46	5.25
10°	A	-1.12	-1.05	-.98	-.91	-.91	-.77	-.77	-.70	-.42	0.00	.42	.91	1.40	1.19	1.05	.63	.98	.63
	E	5.53	5.53	5.46	5.53	5.60	5.39	5.32	5.32	5.53	5.88	6.02	6.09	5.81	5.60	5.25	5.11	4.90	4.76
8°	A	-.91	-.84	-.70	-.63	-.63	-.63	-.56	-.42	-.14	.21	.70	.98	1.33	1.40	.77	.63	.84	.49
	E	5.60	5.53	5.53	5.53	5.60	5.46	5.46	5.46	5.74	6.02	6.09	5.81	5.46	5.11	4.76	4.62	4.48	4.55
6°	A	-.63	-.63	-.63	-.42	-.35	-.42	-.28	-.14	.14	.63	.91	1.05	1.12	1.40	.70	.56	.77	.56
	E	5.67	5.53	5.53	5.53	5.53	5.39	5.46	5.53	5.81	6.02	5.88	5.53	5.04	4.76	4.62	4.20	4.20	3.99
4°	A	-.42	-.35	-.28	-.21	-.14	-.21	0.00	.42	.56	.98	.98	.91	.98	1.26	.70	.56	.77	.70
	E	5.67	5.53	5.53	5.53	5.53	5.46	5.53	5.60	5.81	5.74	5.60	5.25	4.90	4.41	4.06	3.64	3.22	2.94
2°	A	-.21	-.14	-.14	0.00	0.00	.07	.07	.28	.84	1.19	1.05	.84	.91	1.05	.84	.28	.56	.63
	E	5.67	5.53	5.46	5.53	5.46	5.39	5.39	5.53	5.74	5.60	5.46	5.18	4.69	3.99	3.08	2.45	1.96	1.47
0°	A	0.00	-.63	0.00	.07	.14	.28	.42	.70	1.05	1.40	1.19	.91	.77	.70	.49	.07	.35	.70
	E	5.67	5.53	5.39	5.46	5.46	5.25	5.18	5.53	5.60	5.46	5.04	4.69	4.27	3.08	1.75	1.05	.42	0.00
-2°	A	.07	.14	.21	.28	.35	.49	.70	.98	1.47	1.47	1.19	.77	.42	0.00	0.00	-.35	.07	.35
	E	5.67	5.53	5.46	5.39	5.18	5.18	5.53	5.32	5.11	4.55	4.20	3.43	2.24	.70	0.00	-.42	-.84	-.96
-4°	A	.28	.35	.49	.49	.63	.70	.98	1.26	1.75	1.54	1.12	.70	.07	-.56	-.28	-.63	-.14	-.28
	E	5.67	5.53	5.39	5.39	5.18	5.32	5.39	5.25	4.62	4.13	3.64	2.73	1.40	0.00	-.56	-1.19	-1.82	-1.96
-6°	A	.56	.56	.70	.77	.84	.98	1.33	1.68	1.82	1.47	.91	.56	-.28	-1.26	-.84	-.91	-.28	.14
	E	5.67	5.53	5.46	5.32	5.32	5.18	5.32	5.25	4.83	4.27	3.71	3.22	2.10	.63	-.63	-1.47	-2.66	-3.85
-8°	A	.77	.77	.91	1.05	.98	1.19	1.68	1.89	1.89	1.40	.98	.28	-.84	-1.82	-1.40	-1.40	-.70	0.00
	E	5.67	5.53	5.46	5.32	5.32	5.11	5.32	5.11	4.62	3.92	3.43	2.73	1.40	.07	-.98	-1.75	-2.52	-2.80
-10°	A	.98	1.05	1.12	1.26	1.26	1.54	2.03	2.03	1.89	1.33	.91	0.00	-1.61	-2.31	-1.75	-1.33	-.84	.14
	E	5.67	5.46	5.39	5.25	5.32	5.25	4.90	4.90	4.55	3.85	3.15	2.45	.84	0.00	-1.12	-1.26	-1.96	-1.68
-12°	A	1.19	1.26	1.40	1.47	1.54	1.89	2.31	2.17	1.89	1.19	.84	-.28	-2.24	-2.38	-1.82	-2.10	-1.33	.77
	E	5.67	5.60	5.39	5.32	5.25	5.11	5.04	4.76	4.27	3.71	3.08	2.03	.70	.21	-.63	-2.24	-3.92	-4.41
-14°	A	1.40	1.54	1.68	1.68	1.82	2.10	2.38	2.44	1.96	1.19	.70	-.91	-2.31	-2.94	-2.73	-2.52	-1.75	.49
	E	5.67	5.53	5.32	5.32	5.32	5.18	4.83	4.55	4.06	3.57	2.94	1.75	.91	0.00	-1.26	-2.59	-3.99	-7.14

A: Azimuth Angular Deviation (milliradians)
E: Elevation Angular Deviation (milliradians)
Canopy: Sierracin, S/N 0200

Table 5.3   Canopy Angular Deviation Mapping 2.5 Inches Forward
of the Design Eye Position

AZIMUTH LOOK ANGLE (DEG)

		-44°	-36°	-28°	-20°	-12°	-4°	0.0°	4°	12°	20°	28°	36°
14°	A	-1.54	-.84	0.00	.84	.70	1.19	.98	.98	1.47	1.68	1.89	2.38
	E	5.81	5.88	5.95	5.67	5.46	5.18	5.11	5.04	5.60	5.95	6.09	5.81
10°	A	-.98	-.35	.35	1.05	.77	1.19	.77	1.05	1.75	1.61	1.40	1.68
	E	5.95	6.30	6.02	5.18	4.69	4.48	4.41	4.06	4.69	5.39	5.95	6.16
6°	A	-.42	.21	.42	.77	.56	1.12	.77	.84	1.82	1.75	1.26	1.05
	E	6.23	6.30	5.67	4.83	4.34	3.99	3.92	3.78	3.85	4.34	5.46	6.16
2°	A	0.00	.63	.42	.49	.35	.77	.77	1.19	1.54	1.89	1.40	.63
	E	6.23	6.09	5.60	4.48	2.94	1.89	1.54	1.82	2.94	3.50	4.76	5.88
0.0°	A	.42	.84	.49	.42	.14	.56	.77	1.47	1.89	1.82	1.47	.49
	E	6.16	6.09	5.39	4.13	1.89	.56	0.00	.28	1.89	3.43	4.48	5.74
-2°	A	.77	.91	.42	0.00	-.07	.42	.49	1.61	2.38	1.96	1.54	.42
	E	6.23	5.88	5.11	3.57	1.05	-.14	-.63	-.77	.77	3.01	4.20	5.39
-6°	A	1.33	1.12	.49	-.84	-.91	0.00	.28	1.89	3.29	2.66	1.40	.42
	E	6.16	5.39	4.34	2.31	-.21	-2.17	-3.43	-3.01	-.98	1.82	3.99	5.18
-10°	A	1.89	1.26	.35	-1.96	-1.96	-.63	.21	2.38	3.92	3.50	1.40	.21
	E	5.95	5.04	3.99	1.40	-.49	-1.47	-1.19	-1.47	-.63	1.33	3.71	4.83
-14°	A	2.24	1.40	.14	-2.52	-2.45	-1.33	.70	3.22	4.41	3.99	1.54	0.00
	E	5.67	4.98	3.64	1.75	-.63	-3.71	-5.32	-3.57	-.77	1.12	3.36	4.55

ELEVATION LOOK ANGLE

A: Azimuth Deviation (mr)

E: Elevation Deviation (mr)

Canopy: Sierrancin, S/N 0200

62

Table 5.4   Canopy Angular Deviation Mapping 1.25 Inches Right of the Design Eye Position

AZIMUTH LOOK ANGLE (DEG)

ELEVATION LOOK ANGLE		-68°	-60°	-52°	-44°	-36°	-28°	-20°	-12°	-4°	0.0°	4°	12°	20°	28°	36°	44°
14°	A	-1.07	-1.12	-.84	-.56	-.21	.47	1.42	2.52	2.85	2.66	1.76	1.75	1.96	2.03	2.51	2.47
	E	5.67	5.53	5.32	5.11	5.11	5.14	5.48	6.51	6.51	6.44	6.07	6.44	6.51	6.44	5.81	5.67
10°	A	-.48	-.70	-.45	-.21	0.00	1.05	2.31	2.80	2.24	2.52	2.17	2.10	1.64	1.12	1.40	1.76
	E	5.81	5.60	5.46	5.32	5.25	5.61	5.95	5.60	5.32	5.18	4.97	5.25	6.09	6.51	6.23	5.81
6°	A	-.56	-.35	-.87	-.63	.47	1.69	2.31	2.80	2.10	2.31	1.72	2.33	1.42	.40	.63	1.05
	E	5.95	5.67	5.53	5.39	5.60	5.75	5.32	4.76	4.48	4.41	4.20	4.34	4.49	5.81	6.16	5.95
2°	A	-.14	0.88	.21	.42	1.05	2.17	2.03	2.45	1.75	2.03	1.89	2.17	1.96	.98	0.88	.35
	E	5.95	5.74	5.46	5.32	5.67	5.60	4.97	3.74	2.52	2.03	1.89	2.87	3.50	4.93	5.91	5.89
0.0°	A	0.88	.21	.42	.70	1.47	2.31	2.03	1.89	1.54	1.75	2.10	2.31	1.89	1.12	-.07	0.00
	E	5.95	5.67	5.53	5.39	5.53	5.39	4.55	2.59	.48	.49	.35	1.48	3.36	4.27	5.46	5.60
-2°	A	.14	.42	.43	.91	1.75	2.31	1.42	1.33	1.33	1.47	2.10	2.80	1.56	1.12	-.14	-.21
	E	6.02	5.74	5.53	5.32	5.67	5.04	3.35	1.49	-.28	-.21	-.56	.49	2.17	3.45	5.25	5.53
-6°	A	.63	.84	1.05	1.47	2.31	2.17	1.12	-.14	.63	.91	2.24	3.17	2.73	1.05	-.21	-.49
	E	6.02	5.74	5.46	5.39	5.60	4.20	2.52	-.21	-2.24	-3.15	-3.50	-1.19	1.12	3.50	4.44	5.25
-10°	A	1.05	1.26	1.47	2.10	2.59	1.89	0.00	-1.33	-.07	1.12	2.03	3.57	3.24	1.05	-.35	-1.26
	E	6.09	5.81	5.39	5.46	5.11	3.64	1.61	-.91	-1.68	-1.68	-1.05	-.07	.73	3.01	4.06	4.70
-14°	A	1.54	1.75	1.96	2.59	2.60	1.54	-1.54	-2.24	-.91	.70	4.13	4.44	3.85	1.26	-.21	-1.68
	E	6.16	5.95	5.60	5.39	4.83	3.50	.91	-.98	-3.50	-6.44	-5.95	-.77	-.28	2.45	3.43	4.34

A: Azimuth Deviation (mr)

E: Elevation Deviation (mr)

Canopy: Sierrancin, S/N 0200

Table 5.5   Canopy Angular Deviation Mapping 2.56 Inches Right
of the Design Eye Position

AZIMUTH LOOK ANGLE (DEG)

ELEVATION LOOK ANGLE		-68°	-60°	-52°	-44°	-36°	-28°	-20°	-12°	-4°	0.0°	4°	12°	20°	28°	36°
18°	A	-1.05	-.77	-.35	0.00	.56	1.33	2.00	4.69	4.90	4.62	4.69	3.71	3.85	3.43	3.15
	E	4.34	4.06	3.97	3.57	3.36	3.43	4.06	4.03	5.39	5.46	5.46	5.79	6.37	6.44	5.94
10°	A	-.78	-.42	0.00	.28	.84	1.66	3.36	4.97	4.69	4.27	4.20	3.64	3.43	2.73	2.17
	E	4.08	4.34	4.06	3.78	3.58	3.85	4.55	4.62	4.01	4.27	4.27	4.34	5.46	6.16	6.23
6°	A	-.35	0.00	.21	.56	1.12	2.31	3.71	4.55	4.13	3.99	3.85	3.50	3.43	2.24	1.47
	E	4.69	4.34	4.20	3.78	3.78	4.34	4.08	3.78	3.29	3.36	3.50	3.64	4.20	5.00	6.02
2°	A	-.63	.28	.56	.91	1.61	3.08	3.64	4.06	3.64	3.57	3.50	3.50	3.08	2.38	1.12
	E	4.03	4.48	4.34	3.92	3.92	4.41	3.78	2.07	1.54	1.26	.91	2.38	3.29	4.06	5.18
0.0°	A	.21	.49	.77	1.12	1.82	3.15	3.43	3.64	3.22	3.22	3.29	3.78	2.99	2.31	1.05
	E	4.90	4.55	4.34	3.92	3.85	4.27	3.43	2.03	.07	-.14	-.49	.91	2.66	3.71	4.62
-2°	A	.42	.70	.98	1.26	2.10	3.50	3.50	2.07	2.59	3.15	3.08	4.27	3.15	2.17	.98
	E	4.90	4.55	4.34	3.92	3.92	4.06	2.07	1.05	-1.26	-1.54	-1.26	-.29	2.03	3.43	4.34
-6°	A	.91	1.12	1.47	1.68	2.87	3.57	2.87	1.05	1.68	2.45	2.52	4.76	3.99	2.17	.84
	E	5.04	4.69	4.34	4.06	4.27	3.43	1.68	-1.05	-3.15	-3.71	-4.03	-2.10	.49	2.90	3.78
-10°	A	1.33	1.61	1.96	2.10	3.03	3.15	2.10	-.70	1.33	2.03	2.87	4.77	4.62	2.38	.70
	E	5.11	4.69	4.48	4.34	4.06	3.01	.91	-2.38	-3.36	-3.50	-2.24	-.56	.35	2.17	3.22
-24°	A	1.82	2.03	2.31	2.88	3.85	2.87	.56	-2.03	-.21	1.19	4.34	5.11	4.13	2.05	.42
	E	5.11	4.90	4.62	4.34	3.92	2.73	.21	-2.31	-5.18	-6.31	-8.61	-.98	.35	1.68	2.73

A: Azimuth Deviation (mr)

E: Elevation Deviation (mr)

Canopy: Sierrancin, S/N 0200

64

Table 5.6 Canopy Angular Deviation Mapping 1.25 Inches Left of the Design Eye Position

AZIMUTH LOOK ANGLE (DEG)

ELEVATION LOOK ANGLE		-44°	-36°	-28°	-20°	-12°	-4°	0.0°	4°	12°	20°	28°	36°	44°	52°	60°	68°
14°	A	-1.61	-1.19	-.49	-.14	-.42	-.77	-.91	-1.05	-.63	-.21	.42	1.19	1.82	2.03	2.10	2.10
	E	6.02	6.09	6.51	6.79	6.65	6.30	6.23	6.44	6.23	5.74	5.04	4.62	4.83	5.04	5.39	5.67
10°	A	-1.05	-.56	0.00	.28	-.35	-.70	-.70	-.56	-.77	-.77	-.14	.77	1.26	1.54	1.68	1.68
	E	6.09	6.51	6.72	5.88	5.60	5.11	4.76	5.04	5.53	5.88	5.67	4.97	5.04	5.11	5.53	5.74
6°	A	-.49	.07	.28	.35	-.35	-.56	-.77	-.28	-.28	-.77	-.04	.14	.77	.98	1.19	1.26
	E	6.30	6.58	6.23	5.11	4.83	4.41	4.13	3.99	3.85	5.04	5.74	5.25	5.32	5.32	5.67	5.81
2°	A	0.00	.77	.28	.07	-.56	-.56	-.28	-.14	-.21	-.28	-1.19	-.49	.14	.35	.77	.70
	E	6.09	6.16	5.74	4.62	3.88	1.82	1.89	2.45	2.97	3.78	5.18	5.25	5.39	5.39	5.67	5.81
0.0°	A	.35	.91	.28	0.00	-.04	-.63	-.07	.07	-.21	0.00	-1.12	-.91	-.07	.07	.49	.49
	E	5.95	6.02	5.46	3.92	2.03	.28	.07	.91	2.31	3.08	4.76	5.32	5.32	5.53	5.74	5.88
-2°	A	.70	1.05	.35	-.56	-1.26	-.04	.07	.70	.14	0.00	-.91	-1.26	-.35	-.07	.28	.14
	E	5.95	5.74	4.97	3.22	1.05	-.21	-.98	-.70	1.26	2.40	4.41	5.04	5.32	5.53	5.81	5.88
-6°	A	1.47	1.26	.42	-1.54	-1.89	-1.33	0.00	1.26	1.61	.49	-.56	-1.68	-.77	-.56	-.21	-.14
	E	5.74	4.97	3.99	1.89	-.07	-3.01	-3.85	-3.15	-.98	2.03	3.71	4.76	5.11	5.53	5.74	5.81
-10°	A	1.96	1.26	.21	-2.38	-2.38	-.98	-.14	1.54	3.15	1.54	-.21	-1.89	-1.26	-1.75	-.77	-.63
	E	5.39	4.55	3.36	.98	0.00	-1.54	-1.40	-2.10	-1.54	1.12	3.08	4.62	5.04	5.39	5.74	5.88
-14°	A	2.38	1.40	-.21	-2.59	-3.22	-1.96	1.19	2.17	2.94	2.31	-.21	-2.17	-1.75	-1.54	-1.26	-1.05
	E	5.04	4.13	2.87	1.40	-1.05	-4.90	-7.07	-3.15	-1.12	.84	2.80	4.27	4.76	5.25	5.67	5.74

A: Azimuth Deviation (mr)

E: Elevation Deviation (mr)

Canopy: Sierrancin, S/N 0200

65

the azimuth look angle, as shown in Figures 5.15 to 5.19. The azimuth look angle was chosen as the abscissa of these plots for two reasons. The azimuth look angles vary over a much larger range than the elevation angles and the rate of change of the azimuth look angle is expected to vary more rapidly than the elevation angle during the LANA tracking task.

Conclusions. The plots of the angular deviation data, shown in Figures 5.10 to 5.19, illustrate a number of interesting properties of the F-16 canopy. The straight ahead look angle of 0.0 degrees azimuth and 0.0 degrees elevation has very little azimuth or elevation angular deviation. This straight ahead line-of-sight angle corresponds to looking through the center of the head-up display (HUD). The small angular deviation at this angle, despite the severe slope of the windscreen, indicates the design and manufacturing practice of adjusting the thickness of the canopy to minimize the angular deviation over the HUD field-of-view.

A careful study of the plots of the data taken at the design eye position illustrates the effect of canopy shape on the amount of angular deviation generated at that look angle. Figure 5.10, the elevation deviation plot shows that at the 0.0 degree azimuth look angle, the angular deviation varys from 6 mr, at +14° elevation look angle, to -7 mr, at -14°. This wide range in deviation values results from the high slope angle of the windscreen or canopy in this area. As the azimuth look angle moves out toward plus or minus 68 degrees, the angular deviation becomes a constant value of 5.6 mr at all elevation look angles. At 68 degrees azimuth look angle, the curvature of the canopy over the pilot is an almost constant radius curve, therefore the angle of incidence of the light ray (the angle between the windscreen normal and

66
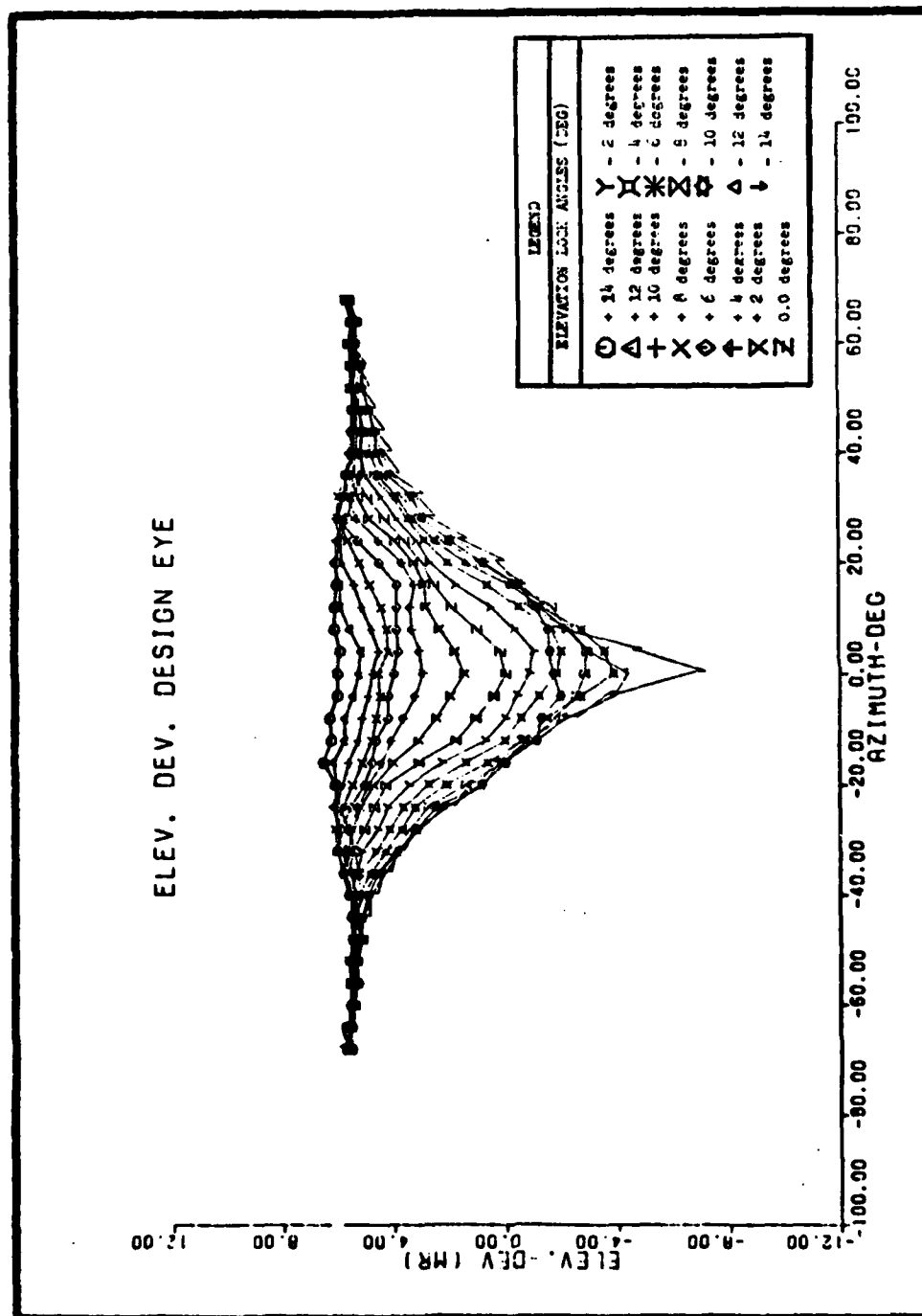
Figure 5.10   Canopy Elevation Deviation at the Design Eye Position
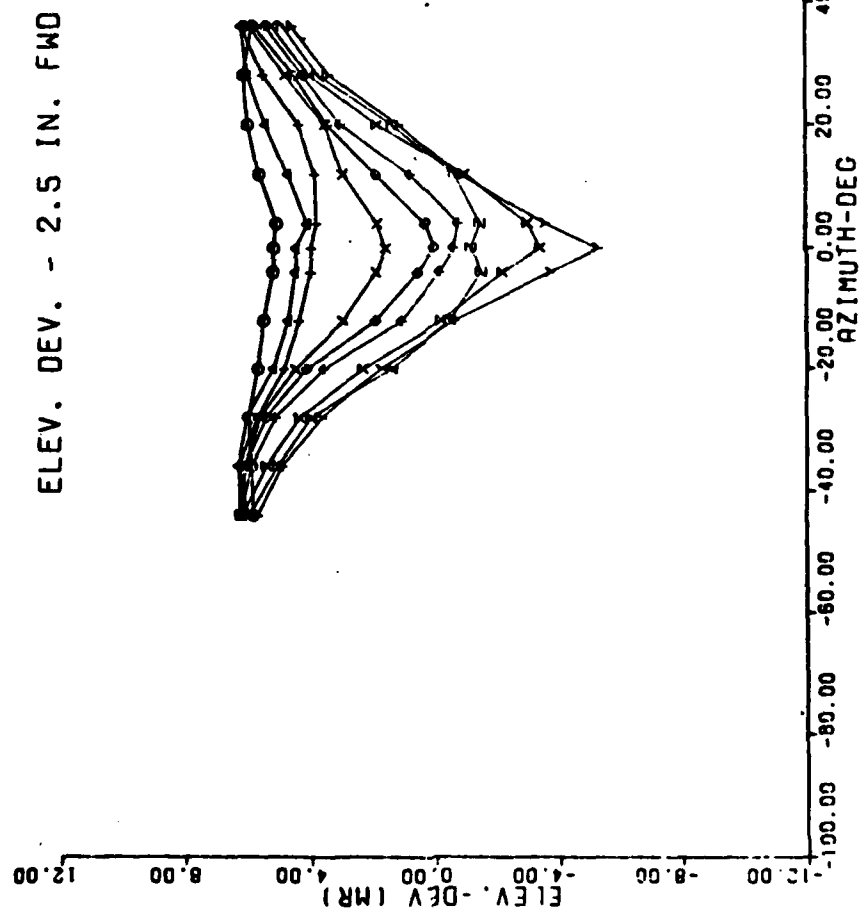
Figure 5.11   Canopy Elevation, 2.5 Inches Forward of Design Eye
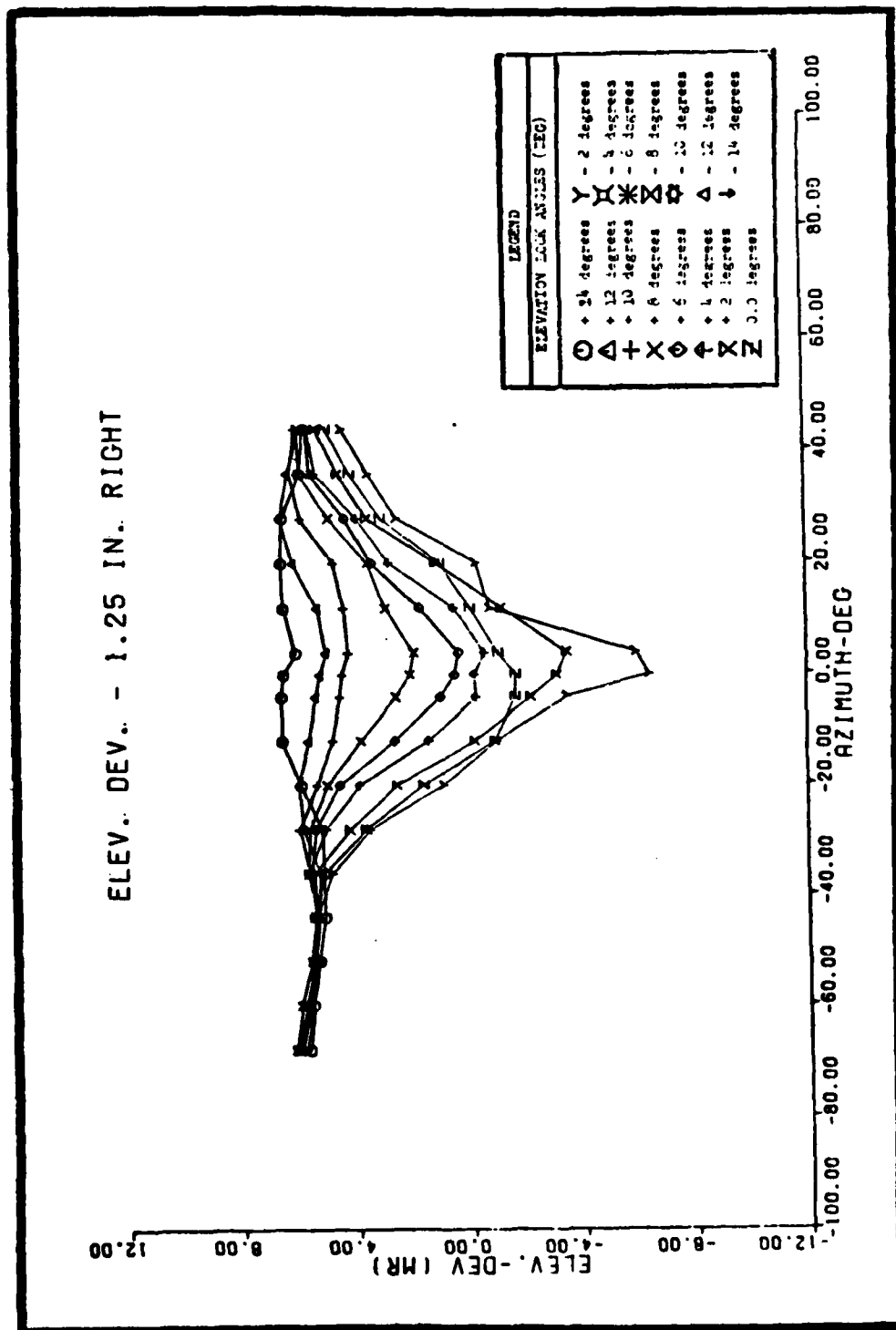
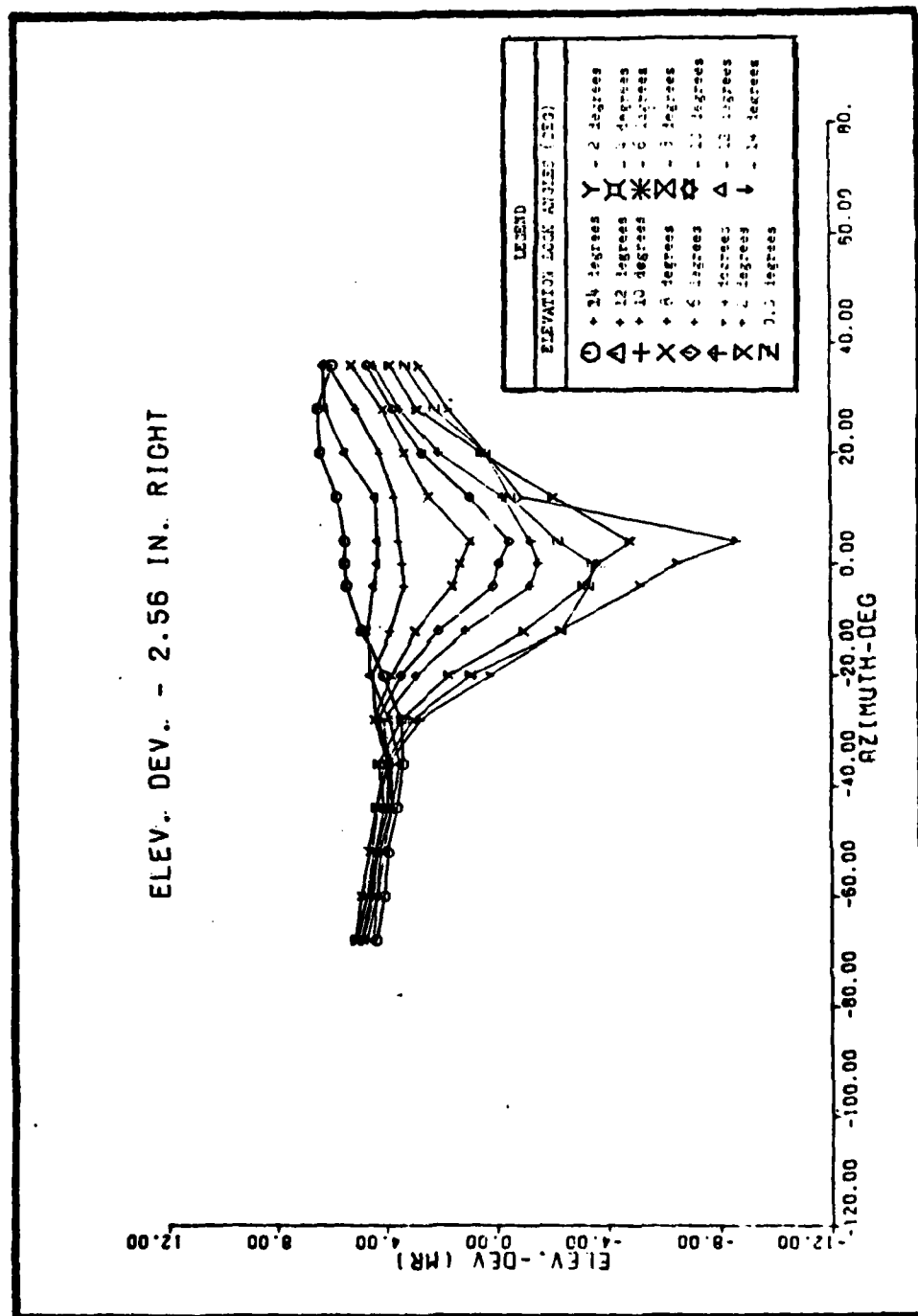Figure 5.12 Canopy Elevation Deviation, 1.25 Inches Right of Design Eye

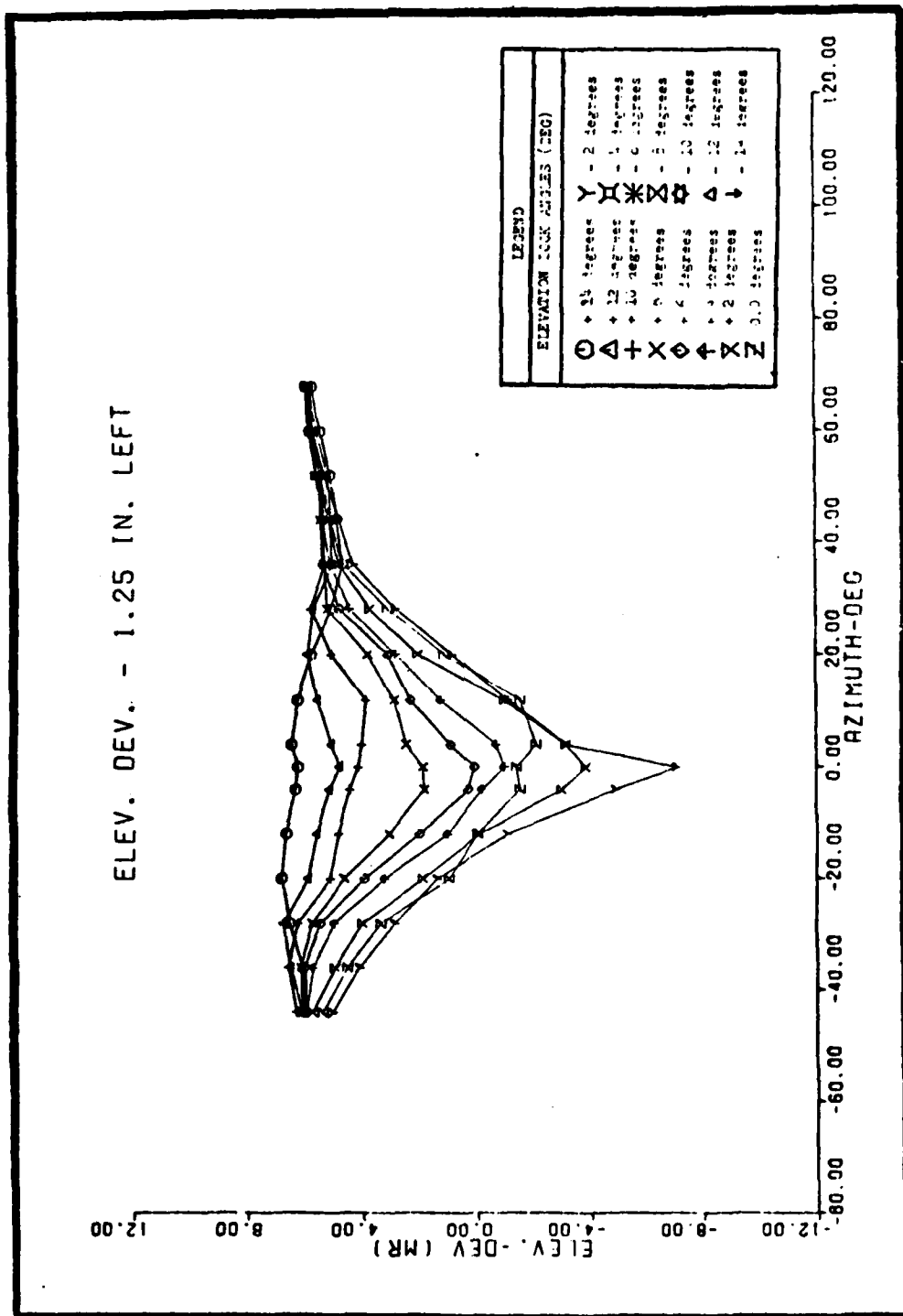Figure 5.13   Canopy Elevation Deviation, 2.56 Inches Right of Design Eye

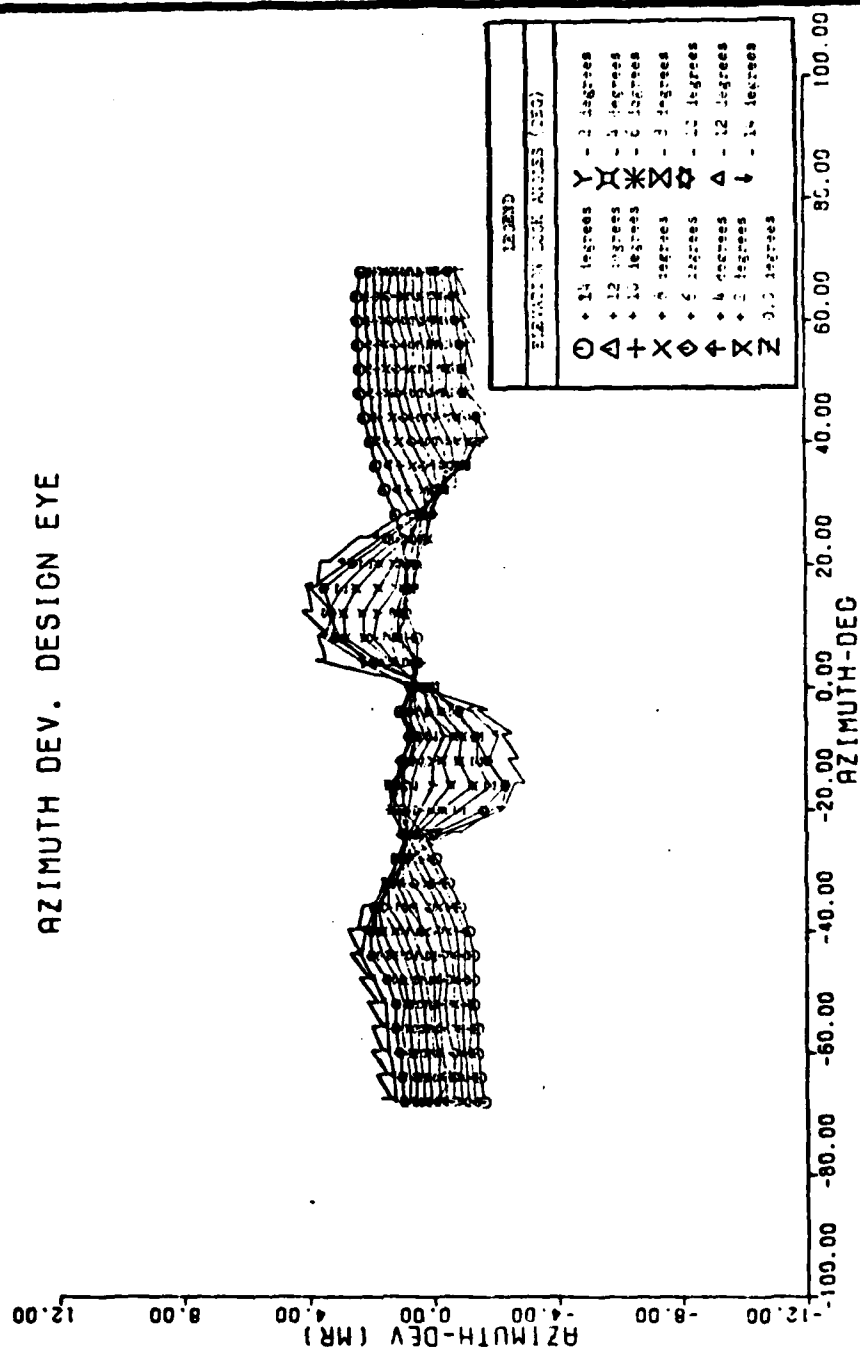Figure 5.14 Canopy Elevation Deviation, 1.25 Inches Left of Design Eye

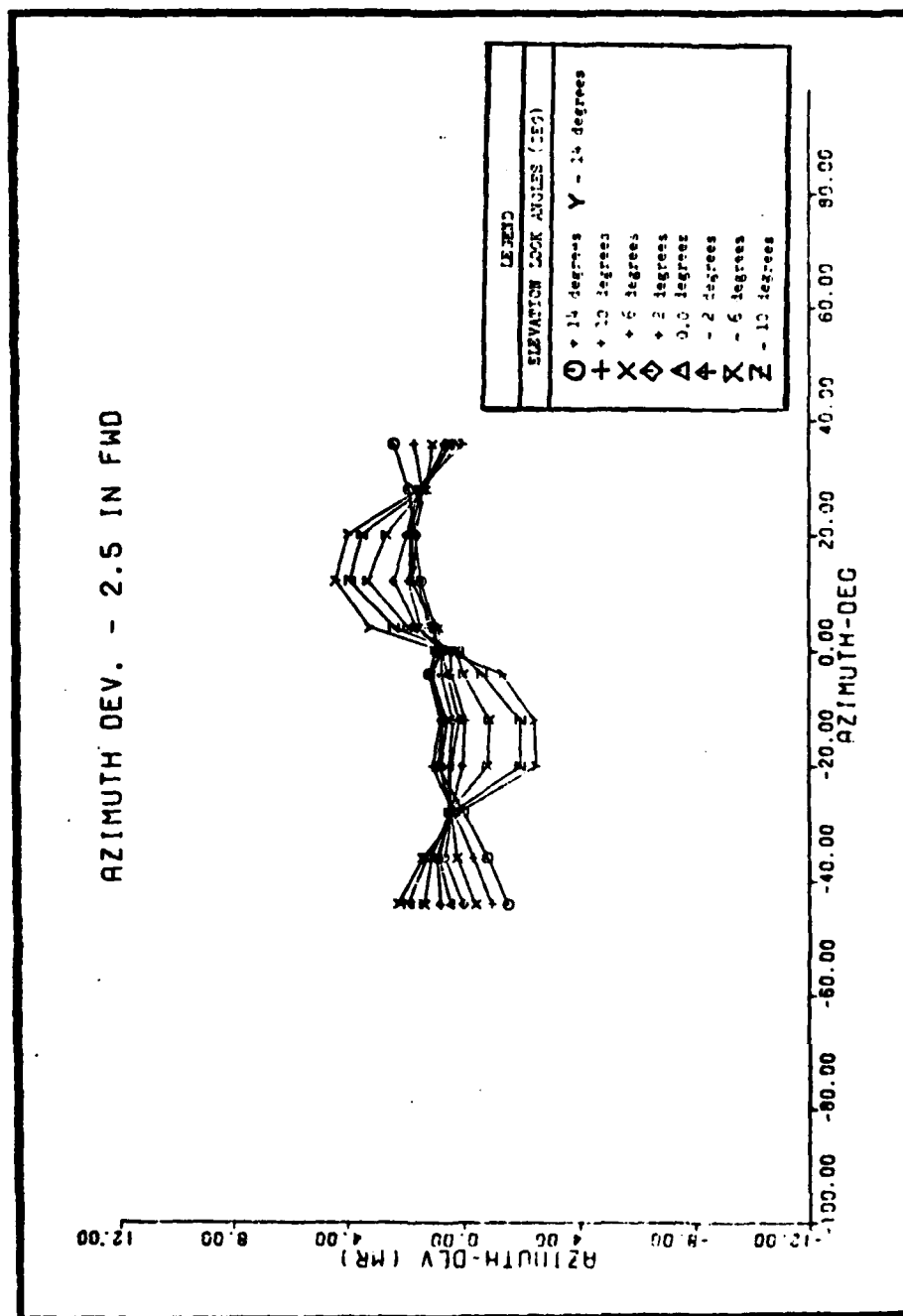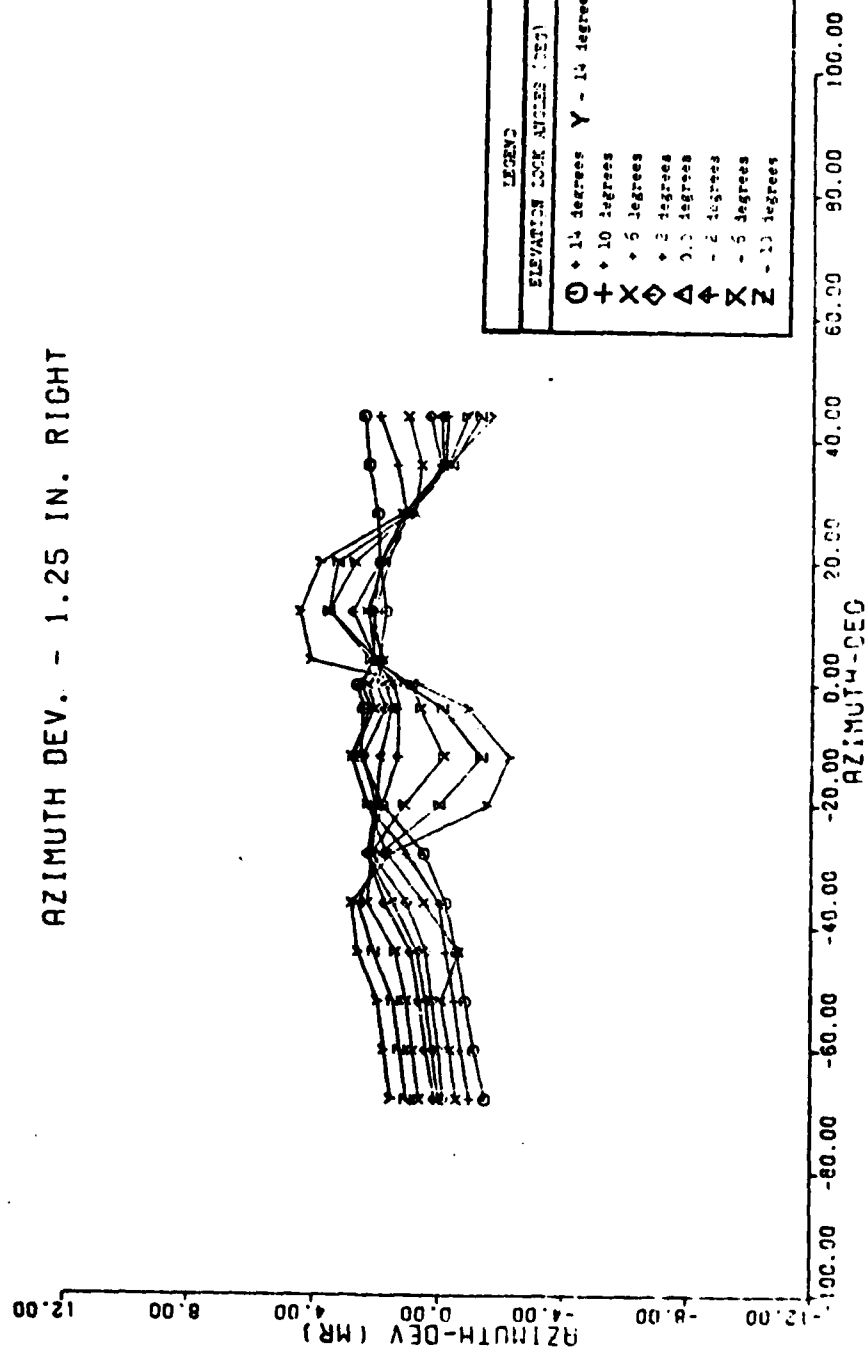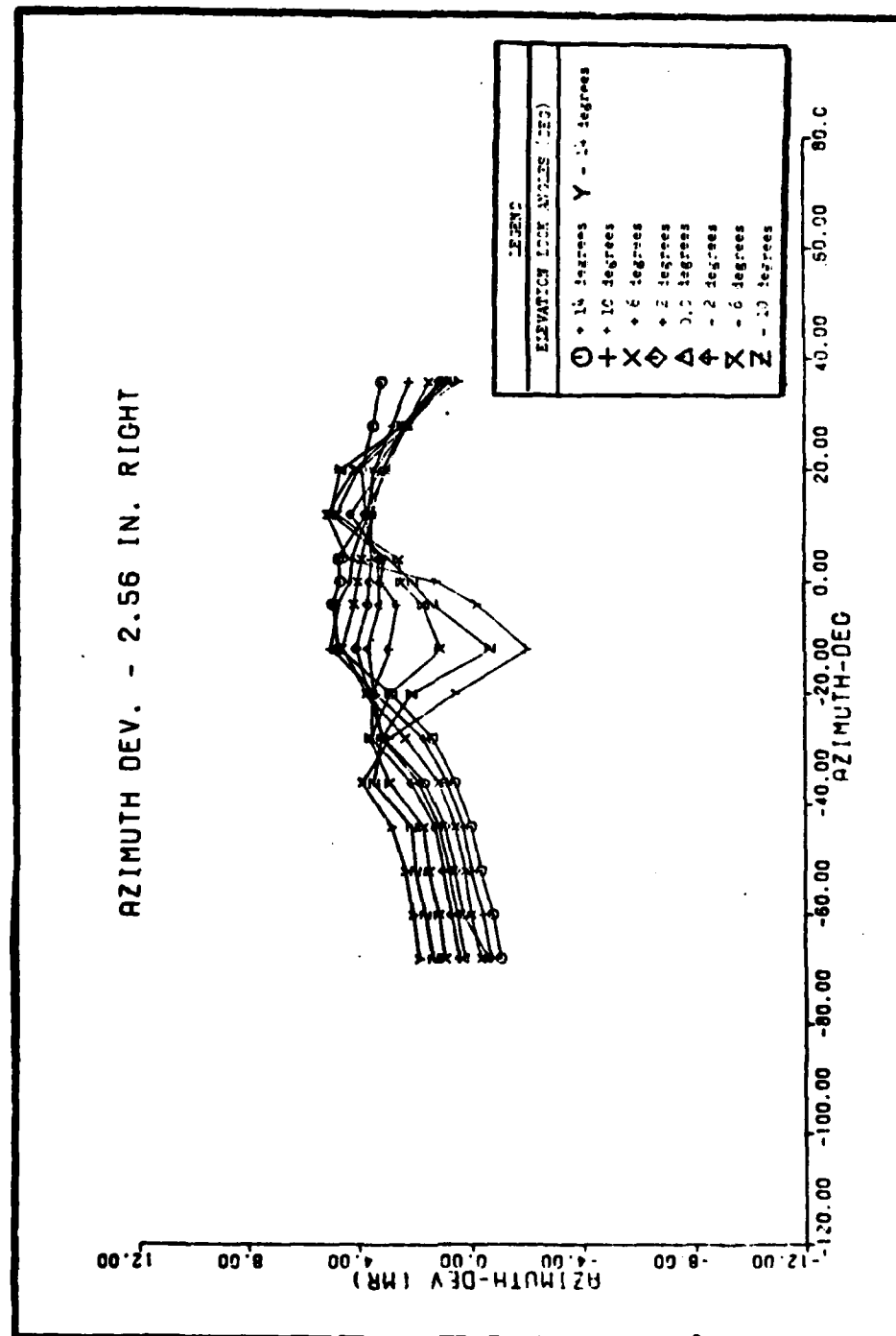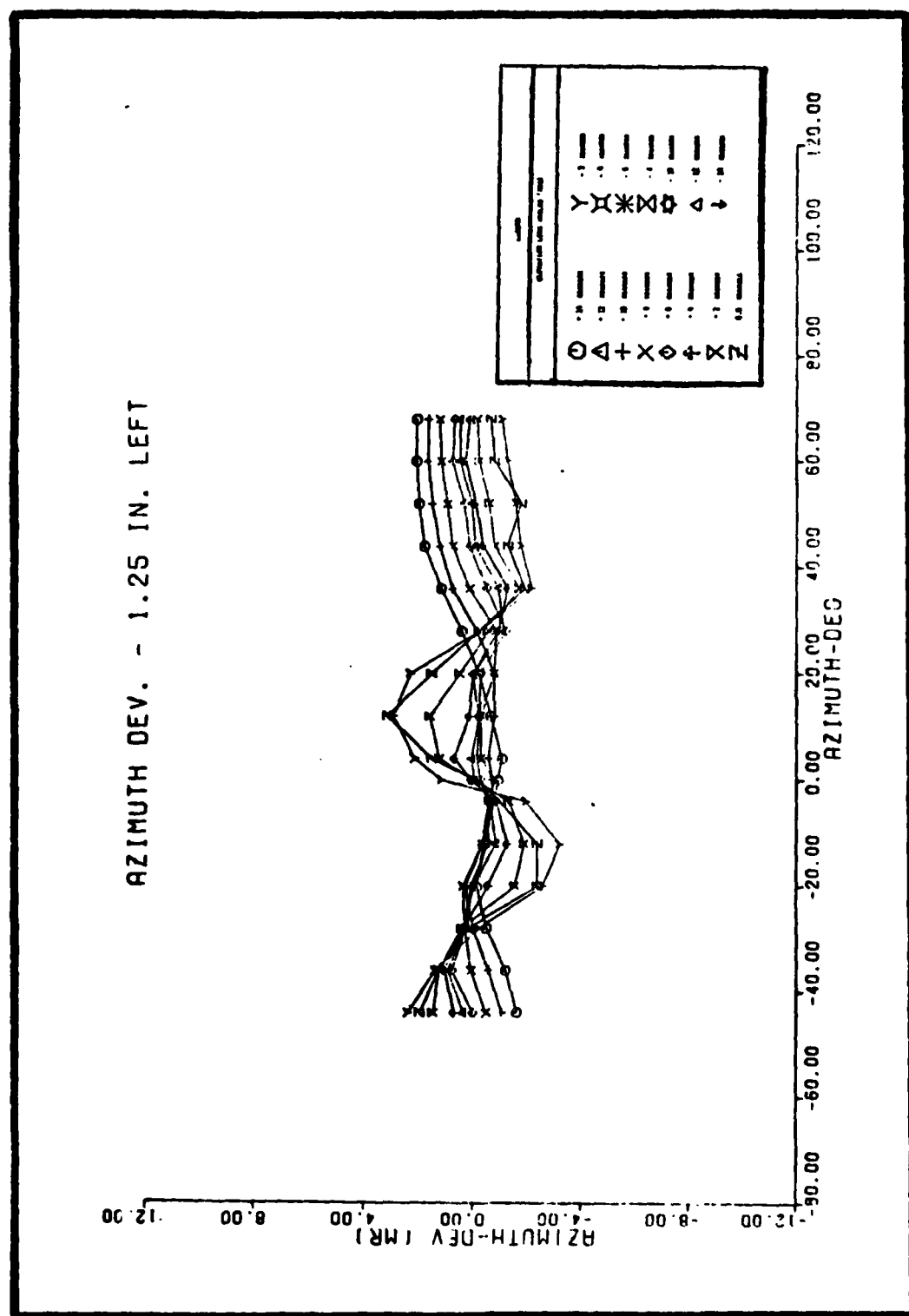Figure 5.15 Canopy Azimuth Deviation at the Design Eye Position

72

Figure 5.16 Canopy Azimuth Deviation, 2.5 Inches Forward of Design Eye

Figure 5.17 Canopy Azimuth Deviation, 1.25 Inches Right of Design Eye

74

Figure 5.18   Canopy Azimuth Deviation, 2.56 Inches Right of Design Eye

Figure 5.19   Canopy Azimuth Deviation, 1.25 Inches Left of Design Eye

the pilot's line-of-sight) is relatively constant over the range of elevation look angles. In Figure 5.15, the azimuth deviation plot, the two lobes centered at approximately the $+15^\circ$ and the -15° azimuth look angles, are caused by the "corners" of the canopy. It is in this area that the canopy has it's most severe bends as the transparency transitions from the windscreen portion to the long side areas of the canopy.

The changes in the amount of angular deviation that are shown in the plots of the mappings, taken at positions other than the design eye position, show an unexpectedly small amount of change. It was expected that as the sighting position was moved towards either side of the canopy that the measurements taken on that side of the canopy would be much larger than those taken at the design eye position. It was felt that the increased incidence angle would inflate the angular deviation values. From this it is concluded that the amount of angular deviation is relatively insenstivie to small movements of the pilot's head position.

Angular Deviation Model

From the results of the canopy mapping experiment the following properties of the angular deviation errors are evident:

1. The canopy refraction error has both an azimuth and an elevation component at each discrete look angle. The maximum elevation error is -7.12 mr and the maximum azimuth error is 3.85 mr.

2. The errors are spatially oriented; that is they are a function of their position. These errors were "built into" the canopy during the manufacturing process.

3. The changes in the angular deviation are relatively small for slight movements away from the design eye position. This means that while the LANA pilot may not always be holding his head exactly at the design eye sighting position, this model of the canopy induced sighting error will still be valid.

These properties and the numerical data from the experiment can be used to develop a practical model of the canopy angular deviation errors.

There are three possible ways that this error source can be addressed by the LANA designer. First, all the mapping data could be stored in the LANA navigation computer memory and used as a look-up table to completely remove the canopy induced sighting errors in the HMS. Alternatively, a curve fit to the data, similar to that routinely performed for HUD compensation, could be developed and used by the LANA on-board computer to remove the majority of the canopy refraction errors. Lastly, without any attempt to compensate for these errors, the full value of the angular deviation will be present to corrupt the sighting.

A simple model was developed which allows the LANA simulation to reproduce these three possible conditions. This model was constructed by taking the measurement data from the design eye position, and computing the mean and standard deviation at each sample azimuth measurement point. This has the effect of compressing the data in the elevation dimension. Although this does result in some loss in accuracy of the model, this is similar to the technique currently used to compute the compensations coefficients for the HUD fire-control computer and would be expected to be used if the LANA system wer actually constructed. Thus, the canopy angular deviation mean and standard deviation will be a function of only the azimuth look angle. The calculated values of the mean and standard

deviation of the azimuth and elevation angular deviation are given in Tables 5.7 and 5.8. The plots of the mean, the mean plus one sigma, and the mean minus one sigma values are shown in Figures 5.20 and 5.21.

The data from Tables 5.7 and 5.8 were curve fitted using the caubic regression program from the Hewlett-Packard HP-41CV statistical program. The HP-41CV program was employed because it is a fast and simple routine which could be manipulated to find the best fit to the data. The highest order polynomial available in this program was the cubic regression program. This program also provided a performance index as an indication of how well the selected curve actually matched the given data. From this curve fitting process, the following four curves were produced:

1. Mean Elevation Deviation (mr) $= a + b(AZ) + c(AZ)^2 + d (AZ)^3$

   where　　　AZ is the azimuth look angle

   $a = 0.0320478$

   $b = 0.186132$

   $c = 0.157798E-2$

   $d = 0.362369E-6$

2. Standard Deviation of Elevation Deviation (mr) $=$

   $e + f(AZ) + g(AZ)^2 + h(AZ)^3$

   where　　　$e = 4.0903391$

   $f = 0.11163114$

   $g = 0.3052673E-3$

   $h = 0.7218124E-5$

   Note: The symmetry of the elevation curves permits a fit to half the curve and the use of the absolute value of the azimuth look angle.
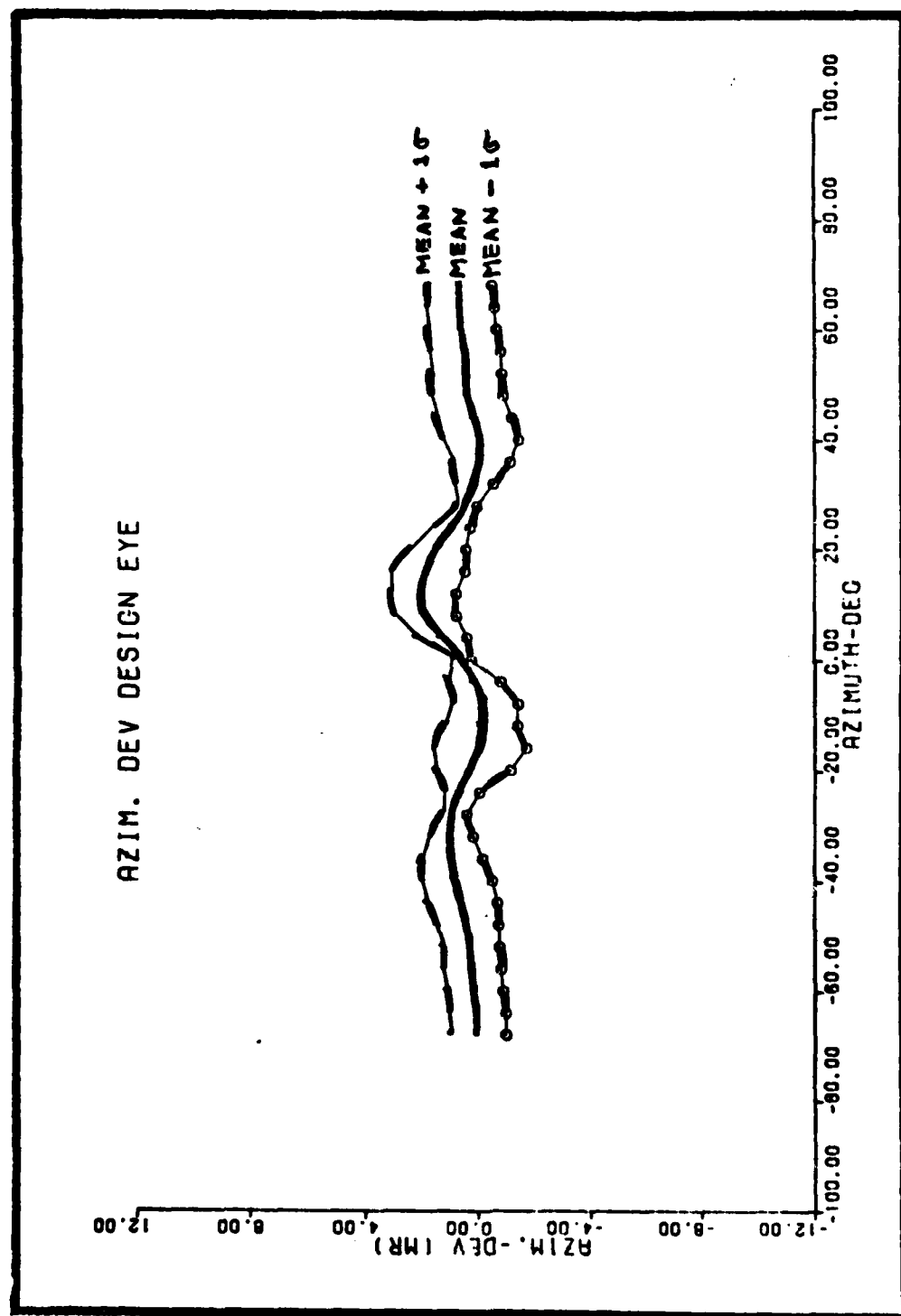
Figure 5.20   Mean Azimuth Angular Deviation (Solid Line) and
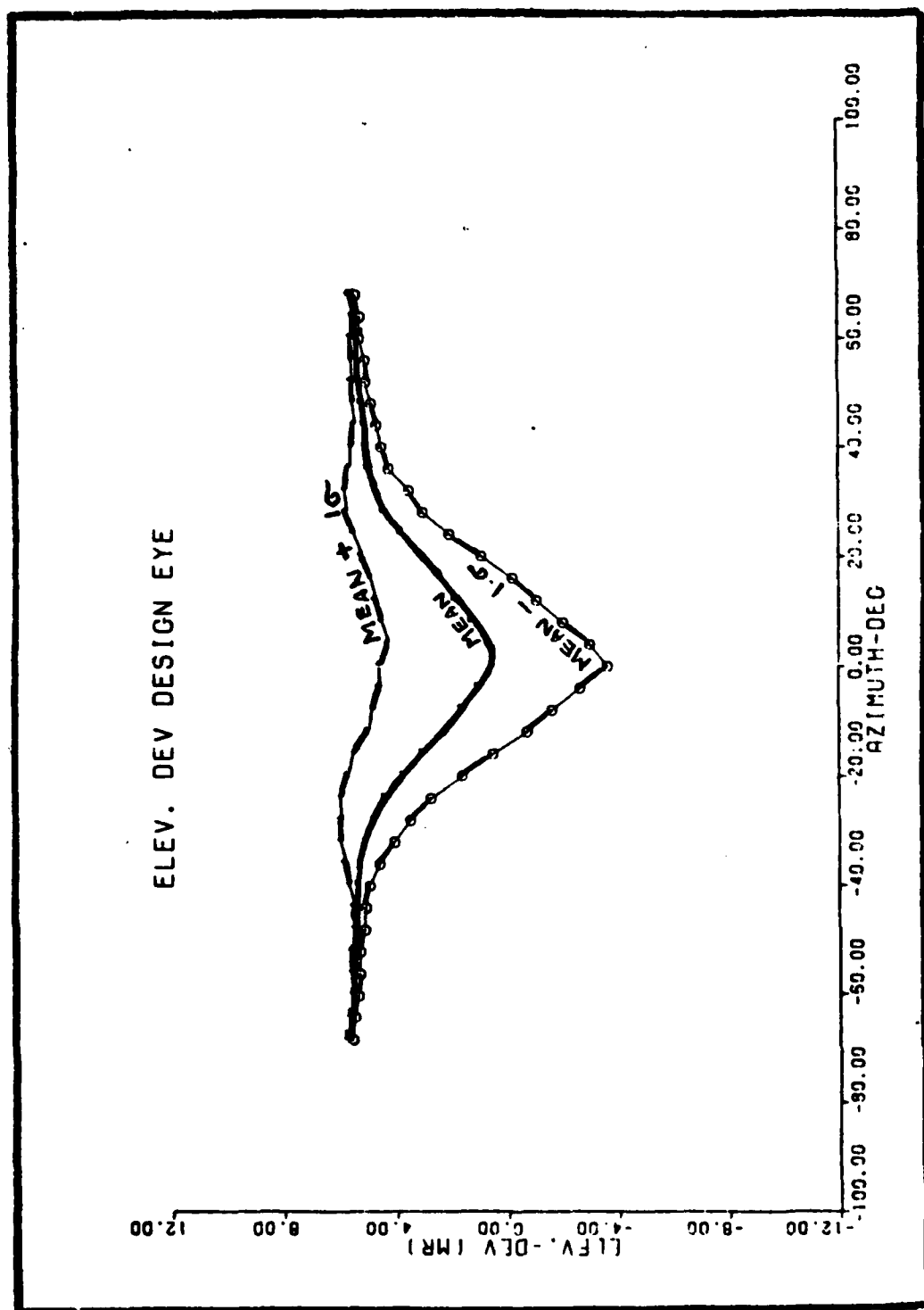Mean Plus and Minus One Sigma (Broken Lines)

Figure 5.21   Mean Elevation Angular Deviation (Solid Line) and
                Mean Plus and Minus One Sigma (Broken Lines)

Table 5.7

Azimuth Angular Deviation, Mean and Standard Deviation Values

Azimuth Look Angle (Deg)	Mean Azimuth Angular Deviation (mr)	Standard Deviation (mr)
-68	-0.065	0.938
-64	-0.047	0.948
-60	0.075	0.961
-56	0.149	0.970
-52	0.210	0.965
-48	0.327	1.059
-44	0.537	1.212
-40	0.700	1.197
-36	0.882	1.030
-32	0.882	0.691
-28	0.793	0.380
-24	0.509	0.550
-20	0.131	1.297
-16	-0.__5	1.588
-12	-0.149	1.251
-8	-0.336	1.093
-4	0.107	0.897
0.0	0.490	0.251
4	1.265	0.858
8	1.834	1.051
12	1.890	1.105
16	1.713	1.226
20	1.363	0.926
24	0.840	0.542
28	0.345	0.303
32	0.070	0.618
36	-0.163	0.975
40	-0.154	1.293
44	0.107	1.287
48	0.313	1.198
52	0.359	1.190
56	0.406	1.194
60	0.523	1.162
64	0.574	1.136
68	0.574	1.063

Table 5.8

Elevation Angular Deviation, Mean and Standard Deviation Values

Azimuth Look Angle (Deg)	Mean Azimuth Angular Deviation (mr)	Standard Deviation (mr)
-68	5.637	0.058
-64	5.530	0.026
-60	5.437	0.057
-56	5.432	0.102
-52	5.437	0.117
-48	5.287	0.129
-44	5.269	0.180
-40	5.189	0.582
-36	5.189	0.582
-32	4.989	0.905
-28	4.709	1.195
-24	4.312	1.562
-20	3.626	2.017
-16	2.945	2.430
-12	2.105	2.816
- 8	1.549	3.173
- 4	0.933	3.578
0.0	0.429	4.062
4	0.607	3.600
8	1.204	3.226
12	1.806	2.861
16	2.310	2.502
20	3.038	2.113
24	3.752	1.670
28	4.354	1.328
32	4.620	1.085
36	4.905	0.655
40	4.979	0.466
44	5.040	0.345
48	5.157	0.268
52	5.269	0.201
56	5.250	0.171
60	5.395	0.111
64	5.357	0.095
68	5.525	0.o81

3. Mean Azimuth Deviation (mr) = $a_n + b_n(AZ) + c_n(AZ)^2 + d_n(AZ)^3$

where   AZ is the azimuth look angle, and

from AZ = 0.0° to AZ = 40°

a_1 = 0.2405565

b_1 = 0.19723107

c_1 = -0.1248514E-1

d_1 = 0.453723E-4

from AZ = 40° to AZ = 68°

a_2 = -10.60448854

b_2 = 0.52329675

c_2 = -0.835924E-2

d_2 = 0.453723E-4

from AZ = 0.0° to AZ = -36°

a_3 = 0.53565464

b_3 = 0.17800193

c_3 = 0.1152084E-1

d_3 = 0.17507E-3

from AZ = -36° to - 68°

a_4 = 4.37913787

b_4 = 0.14575087

c_4 = 0.155768E-2

d_4 = 0.553691E-5

Note: The azimuth curves were broken into four segments
to obtain a more accurate fit over each segment, than
could be achieved over a single interval. The 0° to -68°
interval was split at the -36° point rather than the -40°
point because these intervals provided the highest degree

84
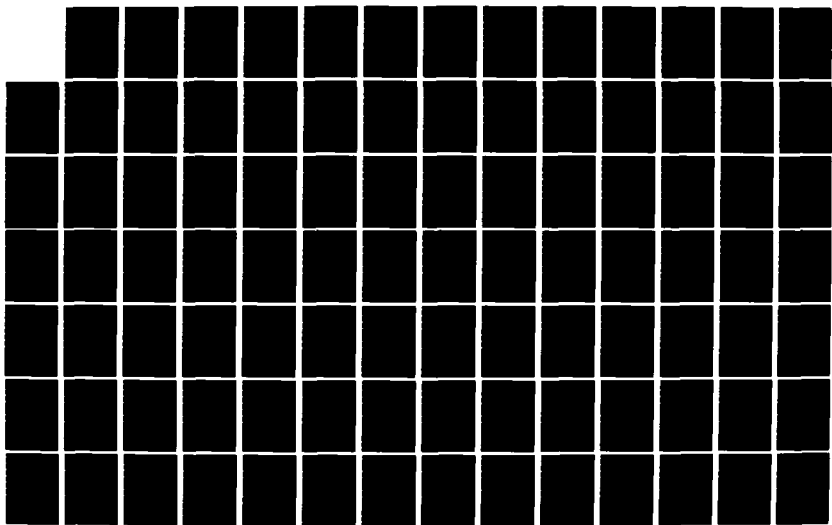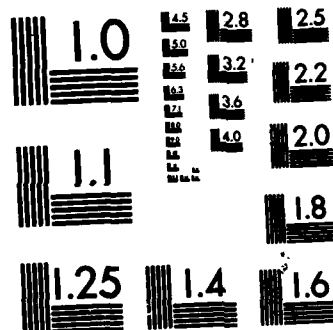
MICROCOPY RESOLUTION TEST CHART

NATIONAL BUREAU OF STANDARDS-1963-A

of file to the data.

4. Standard Deviation of Azimuth Deviation (mr) =

$$e_n + f_n (AZ) + g_n (AZ)^2 + h_n (AZ)^3$$

where

from AZ = 0.0° to AZ = 40°

e_1 = 0.45551742

f_1 = 0.28659151

g_1 = -0.1673922E-1

h_1 = -0.23010E-3

from AZ = 40° to AZ = 68°

e_2 = 5.12449424

f_2 = -0.21260816

g_2 = 0.389924E-2

h_2 = -0.2426457E-4

from AZ = 0.0° to AZ = -36°

e_3 = 0.15079704

f_3 = -0.25583577

g_3 = -0.1585122E-1

h_3 = -0.26044102E-3

from AZ = -36° to AZ = -68°

e_4 = -6.5591175

f_4 = -0.47127730

g_4 = -0.934396E-2

h_4 = -0.59443843E-4

These four curves can be used to simulate three possible canopy compensation schemes as follows:

1. No Canopy Compensation. This condition represents the errors that are generated by the canopy refraction and not removed by any compensation techniques. In this case both the mean and standard deviation data is used as

$$N \text{ (mean, standard deviation)}$$

and used by the subroutine GAUSS to generate an error value to be added to the measurement.

2. Partial Canopy Compensation, similiar to that performed with the HUD, can be simulated. If only the standard deviation curves are used to generate the errors for the azimuth and elevation angular deviation, then this is equivalent to having the major error removed, and the residual error after compensation is represented by the standard deviation values. These standard deviation values are calculated using the same technique as described above.

3. Complete canopy compensation can be simulated by simply not including the mean or standard deviation errors in the LANA simulation. This is equivalent to the LANA designer using a look-up table to completely compensate for the canopy refraction errors.

Model Implementation in LANA. This model was implemented in the LANA measurement equations by the use of four subroutines, one for each of the computed curves. The values of mean and standard deviation of angular deviation for the azimuth or elevation components of the update measurement were added during each update cycle. An input flag (switch) is set by the programmer to choose the no compensation, the partial compensation, or the complete compensation simulation.

86

VI Errors Due to Vibration

Vibration is an environmental condition common to all types of aircraft, and is particularly severe in high performance military aircraft where the operational mission necessarily produces high vibration environments for both crew and avionics. As would be expected, whole body vibration affects human aiming performance; the unwanted motion of the head or eyes significantly impairs individual performance scores. This section is concerned with studying these effects and with modeling them as one of the error sources which contributes to the accuracy of the LANA helmet-mounted sight (HMS) system. Only the effects of whole body vibration on the human operator's ability to aim the HMS are of concern, since the vibrational effects on the equipment performance are included with the HMS hardware model.

It is customary to express vibration in terms of frequency (Hz), peak acceleration (g), and the direction of motion relative to the body. Vibration induced acceleration is indicated by the symbol g, to avoid confusion with linear acceleration which uses the symbol G. The subscripts x, y, and z are used to designate the axis or direction of the motion relative to the human body, as shown in Figure 6.1. Thus, for example, the notation $-0.4g_x$ indicates back to check vibration at a magnitude of 0.40 times the value of earth gravity, taken as 32.2 ft/sec^2.

Nature of the Airborne Vibration Environment

The vibration forces in an aircraft are complex, consisting of a mixture of deterministic and random components acting in three orthogonal axes with 6 degrees of freedom: three translational -- X axis, Y axis,

87
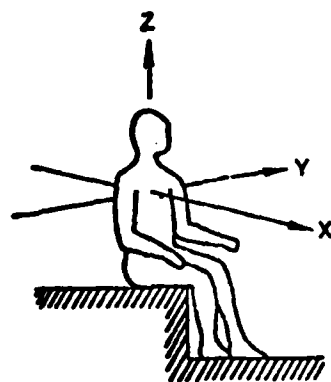
X AXIS = BACK-TO-CHEST

Y AXIS = RIGHT-TO-LEFT SIDE

Z AXIS = FOOT(OR BUTTOCKS)-TO-HEAD

Figure 6.1 Directions of Coordinate System for Mechanical Vibration Influencing Humans (Ref 21:101)

and Z axis, and three rotational -- pitch, roll, and yaw. These forces are a result of internal and external influences. The internal sources include the engine, the aeroelasticity of the structure, and the response of the control system. The external influences result from the interaction between the aircraft and the atmostphere in which it flies (Ref 21:94).

The vibration characteristics are dependent upon the type and size of the aircraft. Rotary-wing and fixed-wing aircraft have entirely different characteristics due to the differences in their propulsion system and airframe structure. In 1971, Speakman (Ref 22) compared the vibration of the B-52 with the F-4C. He found that the magnitude and frequency distribution of the power within the power spectral density plots were different for each aircraft, with the average magnitude of the B-52 about ten times less than the F-4C. He attributes the differences to the greater size and weight of the B-52, although the F-4C trials were performed at very low altitudes and high speeds and therefore more susceptible to gust inputs.

In addition, the power spectral density curves do not always realistically represent the vibration behaviour of the aircraft. For example, time history records of a fighter aircraft flying at low altitude and high speeds generally show that there were frequency "quiet" periods with low amplitude broadband vibration interspersed with large amplitude "bumps" or "shudders" (Ref 21:97).

It is apparent that aircraft type, flight parameters, terrain, and weather are important in determining the nature of the vibration environment in which the LANA pilot must function.

Biodynamic Response to Whole-Body Vibration

The human body response to forced oscillations is very complex. The response cannot be treated as that of a single mass. Von Gierke and Clark (1971) have summarized the effects of vibration on the body as follows:

> ". . . the body when exposed to mechanical forces or motions does not react as a solid mass but is deformed and undergoes elastic changes in shape. When excited with certain input frequencies, resonances of body parts can occur, i.e. the deformation or displacement of the organ is much larger at its resonance frequency than at the other frequencies. For large masses combined with very soft elastic structures, these resonances are at low frequencies; for smaller masses or stiffer suspension, they shift to higher frequencies. The biologic effects of mechanical forces are to a large extent dependent upon the dynamic response of the system, which makes the effect of an input force dependent upon its time course or frequency. Small deformation of tissue can result in the stimulation of receptors; larger deformation body segments or organs can influence their functional capacity. These larger deformations, such as head or eye motions or arm or hand vibrations, are also the ones that interfere with normal task performance." (Ref 23:204)

Transmissibility of Vibration to the Head. Since in most aircraft the aircrew are seated in an upright position, and as shown in Figure 6.2(b), the predominant vibration force is acting in the Z axis direction, it is appropriate to study those experiments where vertical vibration has been applied to the Z axis direction of seated subjects. Furness (Ref 21) compared the results of a number of experiments for subjects experiencing vertical sinusoidal vibration. Although conducted under a number of different seating and instrumentation conditions, as shown in Figure 6.2(a), there is agreement in the form of the data. Generally, the amplitudes of head-to-seat movement are greater than 1 for vibration frequencies between 2 and 7 Hz, and apparently the body is amplifying the vibration transmitted from the seat to the head. Almost all the experimenters have identified a resonance frequency between 4 and
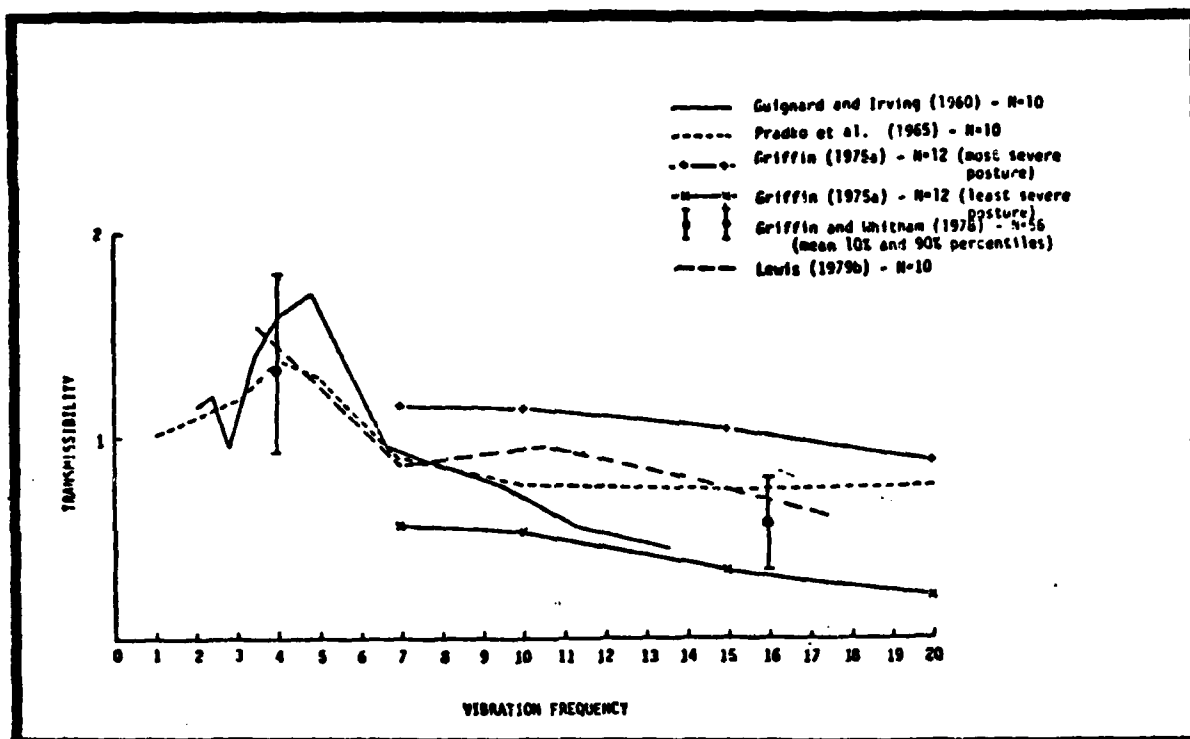
90

Figure 6.2(a)   Comparison of Seat-to-Head Vibration
                Transmissibilities (Ref 21:103)
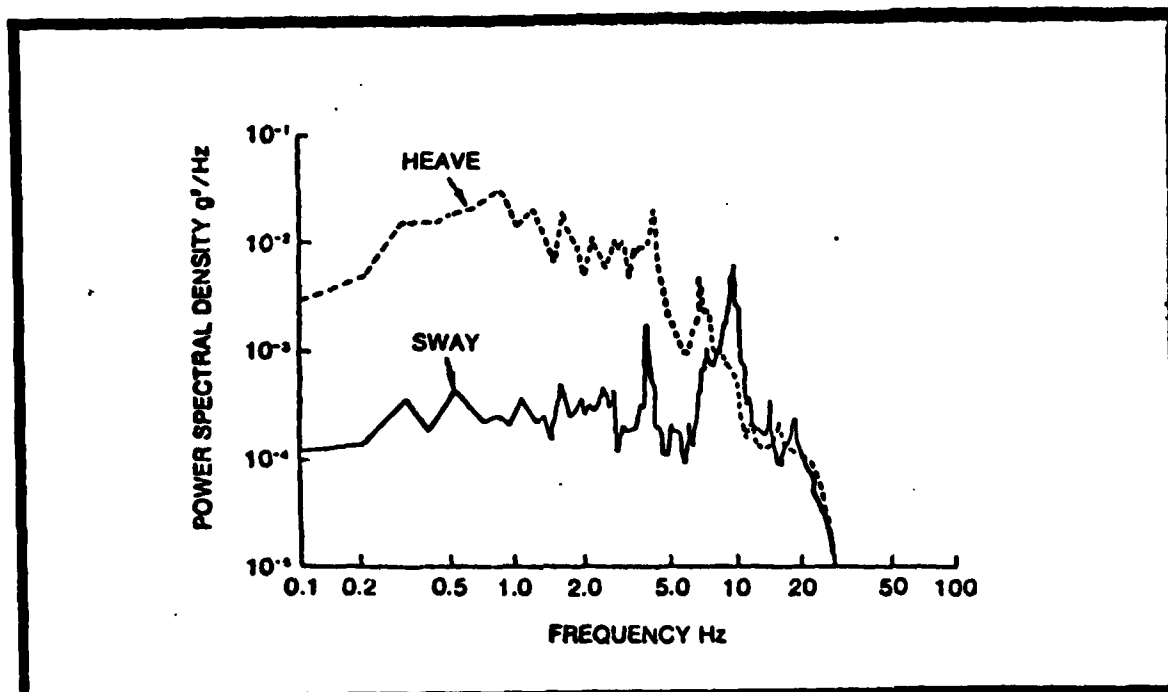

Figure 6.2(b)   Power Spectral Densities for Vibration Acceleration in the
                Vertival "Heave" (Z Axis) and Lateral "Sway" (Y Axis) of
                a Canberra Aircraft Flown at 450 kts at 250 ft Above the
                Ground Level (Ref 25)

6 Hz. These resonance effects are probably a combination of the individual resonances of the pectoral girdle, thorax, and abdominal regions (Ref 21:103). At frequencies below 1 to 2 Hz, the body behaves as a single mass (Ref 24). At the higher frequencies the vibration is absorbed in the buttocks and abdominal cavity.

The posture of the subject, the degree of muscle tension and the head position were found to influence the seat to head transmissibility of vibration. The stiffening of muscles in the abdomen, spine, and neck change the stiffness and subsequently the damping ratio of the resonance within the 4 to 6 Hz frequency range (Ref 21:104).

Experimental Results

Linearity. In order for the biomechanical system to exhibit linearity, the ratio of head motion to seat motion should remain constant over a range of seat vibration amplitudes (at one frequency). Pradko et al. (Ref 26) found that for vertical Z axis sinusoidal vibration of the seat, the head Z axis acceleration was reasonably linear for vibration amplitudes from 0.1 to 0.8 g_z (rms) at discrete frequencies from 3 to 60 Hz. Although nonlinearities in this and other experiments have been observed, Griffen et al. (Ref 27) argued that the magnitude of the nonlinearities were really insignificant when compared to the variabilities due to other factors, such as the intersubject differences. In any case, that linearity is a valid approximation, has been demonstrated.

Operational Experiments. Up to this point only the body's response to sinusoidal vibration occuring in one axis has been discussed. Aircraft vibration has been shown to be multiaxial and dependent upon

92

aircraft type, and is a combination of deterministic and random motion. The most useful biodynamic response data for multiaxial broadband vibration is that measured under actual operational settings.

In 1978, Jarret (Ref 25) recorded vibration data from a Canberra and a Phantom aircraft during low altitude, high speed flight. The recorded levels were 0.25 g_z rms and 0.1 g_y rms for the Canberra and 0.18 g_z rms and 0.1 g_y rms for the Phantom. The recorded vibration times histories were reproduced by a dual-axis vibrator with the subject seated and restrainted in a Canberra ejection seat. Tatham (Ref 20) used this vibrator apparatus to simulate the vibration levels during actual flight conditions, and measured the angular displacement tracking errots of subjects using a helmet-mounted sight. A helmet position sensing system was used to measure the angular deviation of the subject's helmet line-of-sight against a collimated (earth referenced) target located straight ahead and at a fixed line-of-sight. The subject's task was to superimpose a helmet-mounted collimated reticle over the target while being presented with whole-body vibration in Z axis (vertical) and Y axis (lateral). For vibration levels simulating actual flight conditions in the Canberra aircraft (i.e. 0.25 g_z rms, 0.10 g_y rms) the angular displacement tracking errors were about 1.0 deg. rms in azimuth and 2.0 deg. rms in elevation. The power spectral densities (PSD) of the tracking errors in the azimuth and elevation axis are shown in Figure 6-3 (Ref 21:127). Although only the PSDs for the Canberra aircraft were presented in the report, the author indicates that the vibration levels decreased by a factor of about 2.5 in the Phantom. According to Furness (Ref 6), the vibration levels in the Canberra aircraft are more severe than most other military aircraft and can be considered a "worst case"
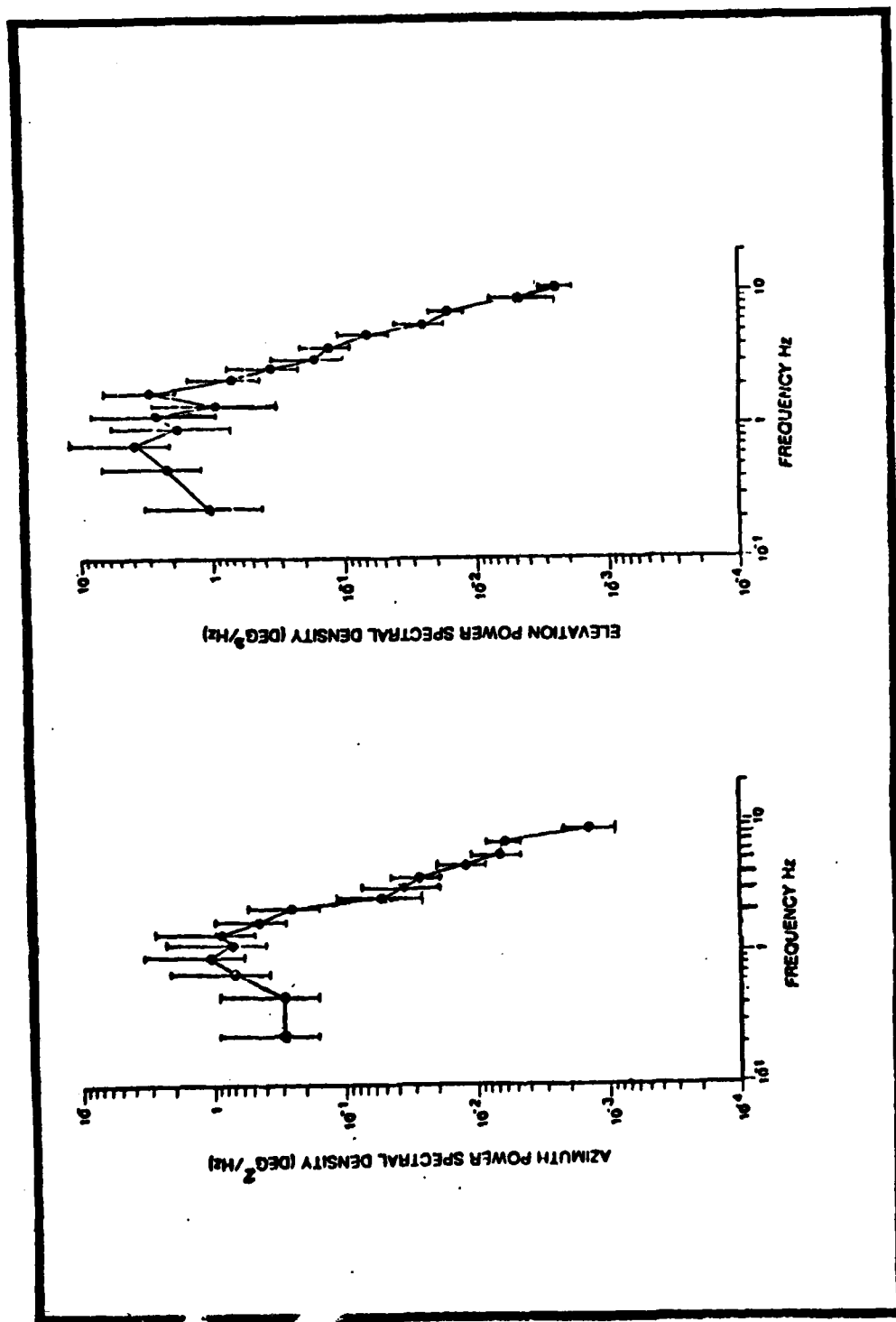
Figure 6.3   Mean Power Spectral Densities of Helmet Tracking Error in the
Pitch (Elevation) and Yaw (Azimuth) Axes Due to Simulated Vertical
(Z Axis) and Lateral (X Axis) Motion From a Canberra Aircraft (Ref 28)

model. The vibration levels in the F-4 aircraft are more typical of the levels encountered in most medium to large fighter aircraft of the type expected to be used for LANA applications. If the linear properties of vibration transmission are valid, then the power spectral densities of the F-4 aircraft can be approximated by reducing the Canberra PDS's by the 2.5 factor.

Vibration Modeling

The elements of interest in this section of the study are LOS displacement in azimuth and elevation resulting from the vibration generated in a typical fighter aircraft. The power spectral density information provides an ideal means of modeling these errors. The process can be envisioned as a white gaussian noise driving a single plant, or transfer function, the output of which is the tracking errors represented by the PSDs of Figure 6-3. The transfer function shown in Figure 6.4 accounts for the vibration forces in the aircraft, generated by the previously mentioned internal and external sources, and the transmission of these vibrations through the human, resulting in the aiming errors. Therefore given the power spectral density of the sighting errors $\bar{\Psi}_{yy}$, we have

$$\bar{\Psi}_{yy} = G(s) \, G(-s) \, \bar{\Psi}_{ww}, \tag{6-1}$$

where $G(s)$ is the system transfer function,

$\bar{\Psi}_{ww}$ is the PDS of the white Gaussian noise.

A second order Markov process provides a good model of oscillatory random phenomena, such as vibration (Ref 29:185). The general form of the power spectral density for a second order Markov process is given as

$$\bar{\Psi}_{yy}(\omega) = \frac{-2 \, \omega^2 + b^2}{\omega^4 + 2\omega_n^2 (2\zeta^2 - 1) \, \omega^2 + \omega_n^4} \tag{6-2}$$
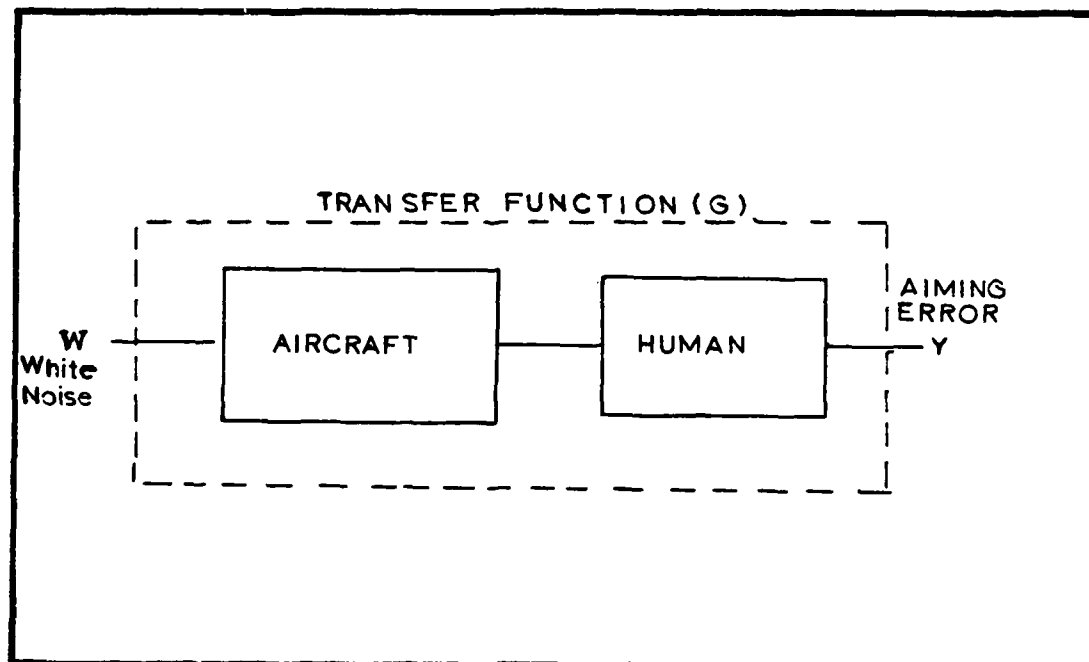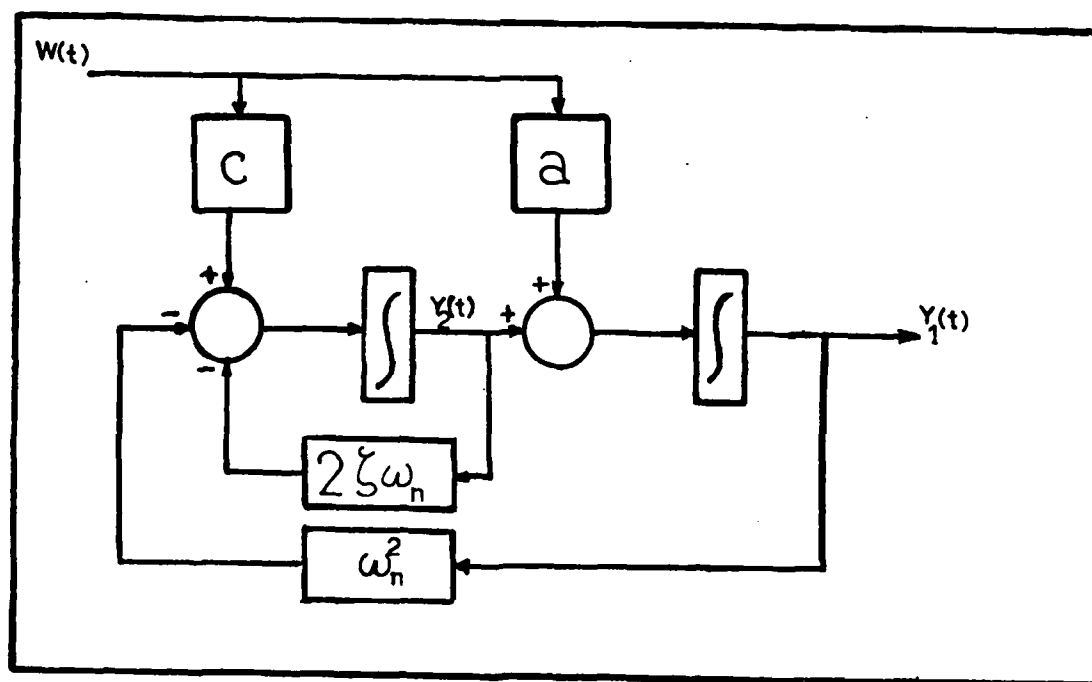
Figure 6.4   Vibration Transfer Function

Figure 6.5   Second Order Markov Block Diagram (Ref 29:183)

This can be generated by pa... ...g a stationary while Gaussian noise of strength $Q = 1$ through a second order system, having a transfer function expressed as

$$G(s) = \frac{as + b}{s^2 + 2\zeta\omega_n s + \omega_n^2} \qquad (6\text{-}3)$$

or a state description as shown in Figure 6.5:

$$\begin{bmatrix} \dot{y}_1(t) \\ \dot{y}_2(t) \end{bmatrix} = \begin{bmatrix} 0 & 1 \\ -\omega_n^2 & -2\zeta\omega_n \end{bmatrix} \begin{bmatrix} y_1(t) \\ y_2(t) \end{bmatrix} + \begin{bmatrix} a \\ c \end{bmatrix} W(t). \qquad (6\text{-}4)$$

where $y_1(t)$ is the vibration induced error, and

$$c = b - 2a\,\zeta\omega_n.$$

To generate this Markov model the values of a, b, ω_n, and ζ are needed. These values are those which generate the best fit of Eq.(6-2) to the power spectral densities of Figure 6.3 (Ref 29:185).

Curve Fitting. In order to determine the appropriate values for a, b, ζ, and ω_n, to be used in Eq. (6-4), a means of curve fitting the power spectral densities of the helmet sighting errors is required. The data taken from the azimuth and elevation PSDs of Figure 6.3 are shown in Tables 6.1 and 6.2 respectively. Since the LANA simulation requires units in radians, seconds, and feet, the data was converted as shown.

A least square regression to fit the PSD data to the form of Eq. (6-2) can be accomplished by generating the following cost function

$$J(a,b,\zeta,\omega_n) = \sum_{i=1}^{k} \left[f\bar{\psi}_{yy}(\omega_i,a,b,\zeta,\omega_n) - f_{DATA}(\omega_i) \right]^2 \qquad (6\text{-}5)$$

and

$f\bar{\psi}_{yy}(\omega_i,a,b,\zeta,\omega_n)$ is the power spectral density function of Eq. (6-2) as a function of frequency

$F_{DATA}(\omega_i)$ is the PSD values from the data of Table 6.1 and 6.2 at each frequency

This cost function was used in conjunction with the IMSL library

97

Table 6.1

Mean Azimuth Power Spectral Data Points
Extracted From Figure 6.3

Original Data		Converted Data	
Frequency (Hz)	PDS Data (Deg^2/Hz)	Frequency (Rad/Sec)	PDS Data (Rad^2/Rad/Sec)
0.24	0.29	1.51	0.141E-4
0.48	0.28	3.02	0.136E-4
0.70	0.69	4.39	0.335E-4
0.91	1.00	5.72	0.485E-4
1.10	0.70	6.91	0.339E-4
1.40	0.84	8.79	0.407E-4
1.80	0.43	11.31	0.208E-4
2.20	0.24	13.82	0.116E-4
2.60	0.05	16.34	0.242E-5
3.20	0.34E-1	20.11	0.165E-5
4.00	0.26E-1	25.13	0.126E-5
4.50	0.12E-1	28.27	0.582E-6
5.30	0.64E-2	33.30	0.310E-6
7.00	0.58E-2	43.98	0.281E-6
8.80	0.13E-2	55.29	0.630E-7

Table 6.2

Mean Elevation Power Spectral Data Points as Extracted from Figure 6.3.

Original Data		Converted Data	
Frequency (Hz)	PSD Points (Deg^2/Hz)	Frequency (Rad/Sec)	PSD Points ($Rad^2/Rad/Sec$)
0.23	1.05	1.45	0.51E-4
0.45	2.20	2.83	0.11E-3
0.67	3.80	4.21	0.18E-3
0.99	1.80	6.22	0.87E-4
1.20	2.80	7.54	0.13E-3
1.30	0.91	8.17	0.44E-4
1.80	2.95	11.31	0.14E-3
2.20	0.70	13.82	0.34E-4
2.80	0.34	17.59	0.17E-4
3.10	0.16	19.48	0.78E-5
4.00	0.12	25.13	0.58E-5
5.00	0.064	31.42	0.31E-5
5.80	0.023	36.44	0.11E-5
7.00	0.016	43.98	0.78E-6
9.00	0.54E-2	56.55	0.26E-6
10.00	0.25E-2	62.83	0.12E-6

subroutine ZXMIN (Ref 36) to determine optimal values of the parameters
a, b, ζ and ω_n. The subroutine ZXMIN finds the minimum of a function of
N variables using a Quasi-Newton method. The search routine ZXMIN was
selected because it requires no explicit gradient information from the
user (it computes the gradient internally). The convergence condition is
satisfied if on two successive iterations, the parameter estimates (i.e.
a, b, ζ, ω_n) agree component by component with the number of significant
digits specified (3 digits for this study). By calculating the values of
the four variables that minimizes the cost function of Equation (6-5),
the best possible least squares fit to the power spectral density data is
ensured. The results of this parameter optimization are shown below in
Table 6.3.

Table 6.3

Azimuth and Elevation PSD Curve Fit Parameters,
from Curve Fit Program

Parameters for Equation (6-4)	Azimuth PSD Curve	Elevation PSD Curve
a : $[a^2=(rad/sec)^3(sec)^2]$	0.0468	0.0998
b : $[b^2=(rad^2)(rad/sec)^3]$	0.00	0.00
ζ : dimensionless	0.575	0.977
ω_n: $[\omega_n = rad/sec]$	6.076	4.265
c = b - 2a$\zeta\omega_n$	-.327	-.831

From the azimuth and elevation PSD curves in Figure 6.3 it is clear that
there is more power or large error in the elevation direction. This
result is consistent with the finding that the vibration fores from the
control and interaction of the aircraft with the air is in the
Z-direction. Thus, the largest errors are expected to be in the size of

100

the a, b, and c coefficients for the elevation data when compared to the azimuth results. The 0.0 value of the variable b for the azimuth and elevation data indicates that the zero of Eq. (6-3) is located at the origin which renders this transfer function insensitive to a step input. This result is consistent logically since the helmet-mounted sight operator, the pilot, does not have his sighting ability degraded by a step input disturbance. For example, if a sudden updraft increases the aircraft altitude by 200 feet, once the transient effects of the motion subside the pilot sighting accuracy is as good as it was at the lower altitude.

Model Description

The second order Markov processes for both the azimuth and elevation helmet sighting errors can be generated by substituting the values from Table 6.3 into Eq. (6-4). The state description of the azimuth sighting errors then becomes

$$\begin{bmatrix} \dot{y}_1(t) \\ \dot{y}_1(t) \end{bmatrix} = \begin{bmatrix} 0 & 1 \\ -36.92 & -6.98 \end{bmatrix} \begin{bmatrix} y_1(t) \\ y_2(t) \end{bmatrix} + \begin{bmatrix} 0.0468 \\ -0.327 \end{bmatrix} W_1(t) \qquad (6\text{-}6)$$

and the elevation sighting errors are

$$\begin{bmatrix} \dot{x}_1(t) \\ \dot{x}_2(t) \end{bmatrix} = \begin{bmatrix} 0 & 1 \\ -18.19 & -8.33 \end{bmatrix} \begin{bmatrix} x_1(t) \\ x_2(t) \end{bmatrix} + \begin{bmatrix} -0.998 \\ -0.831 \end{bmatrix} W_2(t) \qquad (6\text{-}7)$$

Thus by passing a stationary white Gaussain noise of strength Q = 1 through these second order systems the desired model of the Canberra vibration can be generated. By reducing the strength of Q by the 2.5 conversion factor to Q = 0.4, the model of the F-4 aircraft can be generated with the model structure of Eqs. (6-6) and (6-7).

Discrete Model. Since the continuous-time models described above

101

must be implemented in the LANA discrete-time simulation, with discrete-time noise corrupted measurements, discrete versions of the vibration models are required. A general representation of the continuous-time system of Eq. (6-4) is given by the following stochastic, ordinary differential equation

$$\dot{\underline{X}}s(t) = \underline{f}(\underline{X}s, t) + \underline{W}s(t) \tag{6-8}$$

where

  t is time

  $\underline{x}_s(t)$ is the truth system state vector

  $\underline{f}(\cdot,\cdot)$ is the truth system dynamics vector

  $\underline{w}_s(t)$ is a zero mean white Gaussion random process with

  $$E\{\underline{w}_s(t)\underline{w}_s^T(t+T)\} = Q_s(t) \cdot \delta(T) \tag{6-9}$$

  $Q_s(t)$ is the truth system noise strength and

  $\delta(t)$ is the Dirac delta function.

Since $f(\underline{x}_s, t)$ is potentially nonlinear, $\underline{x}_s$ is included in the argument list rather than as a multiplicative term.

SOFE solves the differential equation of Eq. (6-8) in two stages. The first stage propagates the homogenous part of (6-8), while in the second stage the effect of $\underline{w}_s$ is accounted for after propagation. A typical method of doing this involves computing the following "delta covariance" matrix

$$Q_d(t_i) = Q_s(t_i) \cdot (\text{time interval } t_i \text{ to } t_i + 1) \tag{6-10}$$

If the time interval is small compared to the Shannon sampling period associated with $\underline{f}(\cdot,\cdot)$, then $Q_d(t_i)$ approximates the growth in covariances of the $\underline{x}_s$ process caused by the random system disturbance $\underline{w}_s(t)$ over the time interval t_i to $t_i + 1$. The random noise is injected

102

in $\underline{x}_s$ by generating a Gaussian sample $\underline{w}_d(t_i)$ having covariance $Q_d(t_i)$, and adding this sample to the homogeneously propagated $\underline{x}_s$ at $t_i + 1$ (Ref 3:14).

For the linear case, $Q_d(t_i)$ may be computed by solving the following equation

$$Q_d(t_i) = E\left\{\underline{w}_d(t_i)\underline{w}_d^T(t_i)\right\} = \int_{t_i}^{t_i+1} \Phi(t_{i+1},\Upsilon)G(\Upsilon)Q(\Upsilon)\,G^T(\Upsilon)\Phi^T(t_{i+1},\Upsilon)d\Upsilon \quad (6-11)$$

Using Leibnitz's rule to express the differential equation whose solution over $[t_i, t_{i+1}]$ is the right-hand side of (6-4) and omitting the time arguments on all terms but the state transition matrix, the result is

$$\frac{dQd}{dt} = \Phi(t,t)GQG^T\Phi^T(t,t)\ dt/dt$$

$$- \Phi(t,o)GQG^T\Phi^T(t,o)\ do/dt$$

$$+ \int_o^t F\ \Phi\ (t,\Upsilon)GQG^T\Phi^T(t,\Upsilon)\ d\Upsilon$$

$$+ \int_o^t \Phi(t,\Upsilon)GQG^T\Phi^T(t,\Upsilon)\ F^T\ d\Upsilon \quad (6-12)$$

and this simplifies to

$$\frac{dQ_d}{dt} = GQG^T + FQ_d + Q_dF^T \quad (6-13)$$

From the form of Eq. (6-4), Q_d is known to be a 2 by 2 matrix. Therefore to solve for the values of Q_d let

$$Q_d = \begin{bmatrix} q_1 & q_2 \\ q_2 & q_3 \end{bmatrix} \quad , \quad G = \begin{bmatrix} G_1 \\ G_2 \end{bmatrix} \quad , \quad F = \begin{bmatrix} F_1 & F_2 \\ F_3 & F_4 \end{bmatrix}$$

and $Q = [Q]$ (scalar)

Therefore Eq. (6-13) becomes

$$\frac{dQ_d}{dt} = \begin{bmatrix} G_1^2 Q & G_1 G_2 Q \\ G_1 G_2 Q & G_2^2 Q \end{bmatrix} + \begin{bmatrix} F_1 q_1 + F_2 q_2 & F_1 q_1 + F_2 q_3 \\ F_3 q_1 + F_4 q_2 & F_3 q_2 + F_4 q_3 \end{bmatrix} + \begin{bmatrix} F_1 q_1 + F_2 q_2 & F_3 q_2 + F_4 q_2 \\ F_1 q_2 + F_2 q_3 & F_3 q_2 + F_4 q_3 \end{bmatrix}$$

which reduces to the following three equations

$$\dot{q}_1 = 2F_1 q_1 + 2F_2 q_2 + G_1^2 Q$$

$$\dot{q}_2 = F_3 q_1 + (F_1 + F_4)\ q_2 + F_2 q_3 + G_1 G_2 Q$$

$$\dot{q}_3 = 2F_3 q_2 + 2F_4 q_3 + G_2^2 Q$$

103

and expressed in matrix form these become

$$
\begin{bmatrix} \dot{q}_1 \\ \dot{q}_2 \\ \dot{q}_3 \end{bmatrix} = \begin{bmatrix} 2F_1 & 2F_2 & 0 \\ F_3 & (F_1+F_4) & F_2 \\ 0 & 2F_3 & 2F_4 \end{bmatrix} \begin{bmatrix} q_1 \\ q_2 \\ q_3 \end{bmatrix} + \begin{bmatrix} G_1^2 \\ G_1 G_2 \\ G_3^2 \end{bmatrix} \begin{bmatrix} Q \end{bmatrix}
$$

Therefore the values of q_1, q_2 and q_3 can be found by solving these three differential equations. Using the appropriate values for the F and G matrices from Eqs. (6-6) and (6-7) with $Q = 0.4$, the Q_d matrix for the azimuth and elevation processes were found using the CC6600 library subroutine ODE to solve the differential equations of (6-14).

The results are, for the azimuth case

$$
Q_{d(AZ)} = \begin{bmatrix} 0.2123E-4 & -0.15998E-3 \\ -0.15998E-3 & 0.69244E-2 \end{bmatrix} \qquad \text{(units of radians}^2\text{)}
$$

and for the elevation case

$$
Q_{d(EL)} = \begin{bmatrix} 0.9350E-4 & -0.8044E-3 \\ -0.8044E-3 & 0.69244E-2 \end{bmatrix} \qquad \text{(units of radians}^2\text{)}
$$

Model Implementation in LANA. Now to implement this noise injection process in the LANA simulation program, the following technique was used:

$$
E \{ \underline{w}_d \underline{w}_d^T \} = Q_d = \begin{bmatrix} q_1 & q_2 \\ q_2 & q_3 \end{bmatrix}
$$

Let $\underline{w}_d = \sqrt{Q_d}\, \underline{z}$ where $\sqrt{Q_d} \cdot \sqrt{Q_d}^T = \sqrt{Q_d}$

and Q_d is any square root - in this study $\sqrt{Q_d}$ is the Cholesky square root matrix (Ref 29:370).

Therefore $\quad E \{ \underline{w}_d w_d^T \} = E \{ \sqrt{Q_d}\, \underline{z}\underline{z}^T \sqrt{Q_d}^T \}$

$$
= \sqrt{Q_d}\; E \{ \underline{z}\underline{z}^T \} \sqrt{Q_d}^T
$$

Then select $\underline{z}$ such that

$$
E \{ \underline{z}\underline{z}^T \} = I \qquad \text{the identity matrix}
$$

104

For example $\underline{z}_1 \quad \Sigma \quad N(0,1)$ where $\underline{z}_1$ and $\underline{z}_2$ are independent,

$$\underline{w}_2 \quad \Sigma \quad N(0,1) \quad \text{and thus } E\left[\underline{z}_1 \, \underline{z}_2\right] = 0 \tag{6-15}$$

Then $\quad \underline{w}_d = \sqrt{Q_d} \, \underline{z}$

where $\quad E\{\underline{w}_d \, \underline{w}_d^T\} = Q_d$

In the LANA truth model the azimuth and elevation vibration second order Markov processes will each require two truth states. Let these be indicated as

$$\begin{bmatrix} X_{s_1(AZ)}(t) \\ X_{s_2(AZ)}(t) \end{bmatrix} \quad \text{for the azimuth truth states}$$

and

$$\begin{bmatrix} X_{s_1(EL)}(t) \\ X_{s_2(EL)}(t) \end{bmatrix} \quad \text{for the elevation truth states.}$$

Now for the homogenous parts of Eqs. (6-6 and 6-7) are implemented as

$$\text{AZIMUTH} \quad \begin{bmatrix} \dot{X}_{s_1(AZ)}(t) \\ \dot{X}_{s_2(AZ)}(t) \end{bmatrix} = \begin{bmatrix} 0 & 1 \\ -36.92186 & -6.98288 \end{bmatrix} \begin{bmatrix} X_{s_1(AZ)} \\ X_{s_2(AZ)} \end{bmatrix}$$

and

$$\text{ELEVATION} \quad \begin{bmatrix} \dot{X}_{s_1(EL)}(t) \\ \dot{X}_{s_2(EL)}(t) \end{bmatrix} = \begin{bmatrix} 0 & 1 \\ -18.186917 & -8.33252 \end{bmatrix} \begin{bmatrix} X_{s_1(EL)} \\ X_{s_2(EL)} \end{bmatrix}$$

The effect of w_d is added at discrete points, t_i, to the truth states in the following manner:

$$\begin{bmatrix} \dot{X}_{s_1(Az)}(t_i) \\ \dot{X}_{s_2(Az)}(t_i) \end{bmatrix} = \begin{bmatrix} X_{s_1(Az)}(t_i) \\ X_{s_2(Az)}(t_i) \end{bmatrix} + \begin{bmatrix} \sqrt{Q_{d(Az)}} \end{bmatrix} \begin{bmatrix} z_1 \\ z_2 \end{bmatrix} \tag{6-16}$$

where the time argument t_i means the time before discrete noise addition. The random noise is added to the elevation truth states using the same technique. The time interval between calls to the noise injection subroutine was set at 0.03 seconds. This value was based upon the time constant of the azimuth and elevation second order Markov processes which

105

are 0.28 and 0.24 seconds respectively. Where the time constant T_c was computed as

$$T_c = \frac{1}{|\zeta\omega_n|}$$

Using Shannon's sampling theorm to set the noise injection interval at 1/10 of .28 or approximately 0.03 seconds.

VII   Errors Due to the Helmet-Mounted Sight Hardware

The concept of a sighting system which integrates the natural visual and motor skills of the pilot's head to direct a weapon system is documented as far back as 1940. Between 1940 and 1960 behavioral scientists were attempting to analyse the movements of the pilot's eyes to determine his instrument scan and visual search patterns (Ref 31:vi). Since the early 60's, the Army, Navy, Air Force and industry have pursued parallel programs aimed at developing an accurate and operationally useful Helmet-Mounted Sight (HMS).

There are many potential applications for such a sight, and by adding a helmet-mounted display, the effectiveness of the pilot can be significantly increased. The helmet-mounted sight takes advantage of the human head's natural aiming ability to provide a means of easing the pilot's manual workload and supplies an additional means of controlling a sensor or weapon. The application that has driven the HMS development was the potential to aim weapons and sensors. The wide field-of-view of the HMS is ideal for providing course pointing information to narrow field-of-view sensors. One of the proposed uses for the HMS, is with the LANA system, to enable to the pilot to take off-set position fixes or sightings which are used to update the inertial navigation system. Since the helmet-mounted sight is the principle hardware element in the LANA system, it is important that any simulation of this system has an accurate error model.

Modeling Discussion

There are a number of different types of helmet-mounted sights available commercially. While they all perform basically the same

function, that of measuring the position and orientation of the head, there are at least four entirely different techniques in use today. Since a particular HMS type has not been selected for use with the LANA concept, the creation of a model for the helmet aiming errors is complicated by the variety of possible candidates. All of the available HMS's use a differnt form of measurement technology; one type uses infrared light, another electro-magnetic radiation, a third uses a mechanical linkage, while the last employs ultrasound.

Without elaborating on each of these sights, a detailed review of the open literature, and discussions with HMS engineers at the Aerospace Medical Research Laboratory (AMRL), indicates that the electromagnetic concept has emerged as the pre-eminent system available at this time. This HMS has been shown to be superior to all other candidates, both in terms of accuracy and potential for further improvement (Ref 14).

Polhemus Helmet Mounted Sight

Polhemus Navigation Sciences Inc. (PNSI) has developed an advanced HMS using electromagnetic techniques called the SPASYN Helmet-Mounted Sight (SHMS). The term SPASYN is derived from the words Space Synchronized. The space synchro concept uses an electromagnetic closed-loop transducing and computing scheme which provides precise and continous measurement of the relative position and orientation between two independent coordinate frames (Ref 31:400). The electromagnetic radiator for the SHMS are isotropic core structures wound with three identical orthogonal coils, giving uniform sensitivity in all directions over the unit sphere. (A more detailed description of the SHMS operation is presented in Appendix A.) The radiator is mounted at some convenient

location inside the cockpit. The sensor is mounted on the helmet as shown in Figure 7.1. This closed loop system tracks the position of the sensor relative to the radiator, and resolves 6 measurements to compute the position and orientation of the sensor and helmet (Ref 31:402).

Accuracy

There are currently two versions of the SHMS system commercially available, the SHMS II and the SHMS III; a third advanced version, the SHMS IV is currently undergoing static accuracy test at Wright-Patterson AFB, in the Aerospace Medical Research Laboratories (AMRL). Each successive version has demonstrated greater accuracy than that of its predecessor and added such functions as turbulence filtering and rate aiding. Approximate accuracy results are shown in Table 7.1 for the three versions of the SHMS system. These accuracy data have been estimated using the references shown and these estimates have been reviewed by the engineers who are engaged in HMS accuracy measurements experiments at AMRL.

The SHMS III and SHMS IV versions have been equipped to supply rate aiding and turbulence filtering during the processing of the measurement information in the microprocessor of the electronics unit. With the turbulence filtering function activated, a digital moving window filter is applied to the LOS output. This filter reduced high frequency LOS jitter that results from aircraft vibration, internal electronic noise and external environmental noise (Ref 32:3-6). The sight is also capable of supplying rate aiding or filtering, where again a digital-averaging filter, implemented in software, is used to increase or decrease the width of the window depending upon the rate of head motion. At high

109

A CLOSED-LOOP TRANSDUCING/COMPUTING SCHEME USING A VECTOR
FIELD COUPLING BETWEEN AIRFRAME & HELMET MOUNTED SIGHT

3 AXIS SENSOR

STRAP-DOWN 3 AXIS RADIATOR

RADIATOR
EXCITATION

SENSED
INFORMATION

SYSTEM
ELECTRONIC
UNIT

LOS

SYSTEM
CONTROL
PANEL
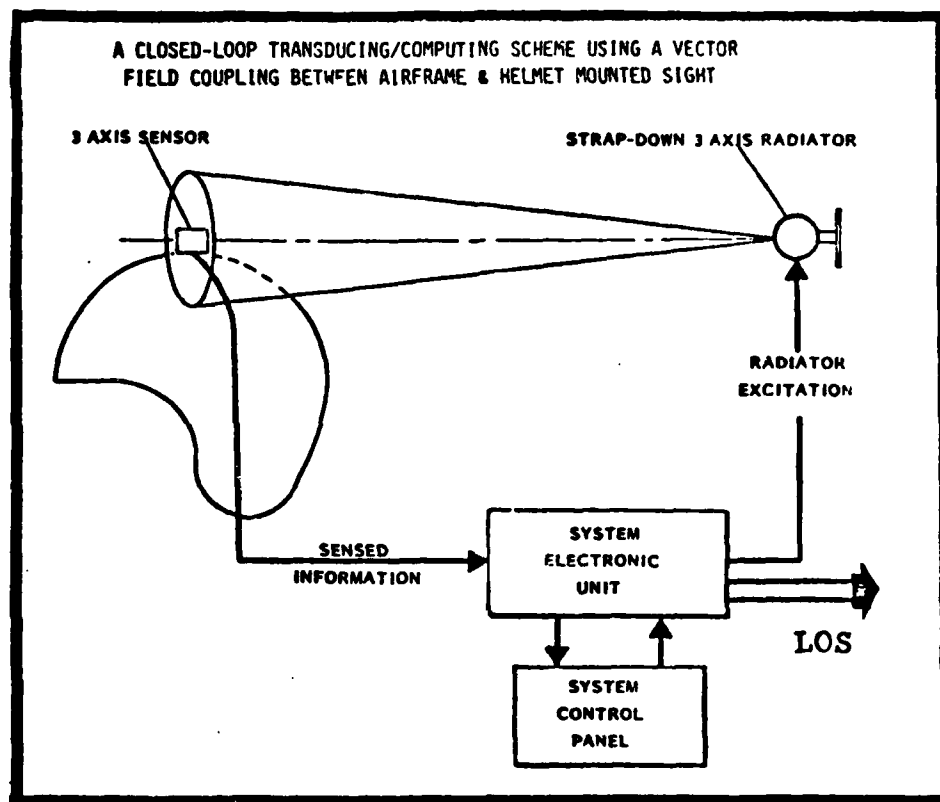
Figure 7.1   Space Synchro Helmet-Mounted Sight Concept (Ref 12:16)

TABLE 7.1

Aiming Accuracy Data for the Three Versions of the Polhemus SHMS.
Accuracy Results are Expressed as the Standard Deviation of Radial Error.
(Ref 32:29, Ref 14, Ref 6)

Test Condition	Aiming Accuracy Standard Deviation of Radial Error		
	SHMS II	SHMS III	SHMS IV
Laboratory	0.25 deg.	0.20 deg.	0.15 deg.
Static Grd. (installed in aircraft)	0.40 deg.	0.30 deg	**
Dynamic Grd. (installed in aircraft)	0.70 deg.	0.40 deg.*	**
Flight Test	0.80 deg.	**	**
* with rate aiding and turbulence filtering			
** not available			

rates of head movement more of the high frequency components are passed
(Ref 32:3-6). This adaptive filtering is responsible for the improvement
in dynamic accuracy of the SHMS III version over the SHMS II.

Since the best possible accuracy is desired for the navigation
update application of the helmet-mounted sight, it is reasonable to
expect that the SHMS IV version of the Polhemus HMS would be used in a
future LANA system. In order to construct a model for the SHMS IV HMS,
an estimate of the systems errors once the helmet is placed in
operational use must be derived. This value can be estimated by using
the data from Table 7.1 and extrapolating from the SHMS II and SHMS III
results to predict the accuracy of the SHMS IV. After examining the
accuracy data and from discussions with the AMRL engineers the magnitude
of the SHMS IV operational aiming error was estimated to be approximately

0.4 degrees standard deviation of radial error (Ref 6).

To develop a complete model it is necessary to have more information about the nature of the helmet-mounted sight aiming errors, in addition to a figure for the magnitude of the errors. To define the nature of these errors it is necessary to look at their source(s) and determine the means used to compensate for them.

Cockpit Mapping and Compensation. The accuracy data shown in Table 7.1 for the laboratory test conditions indicates that in a magnetically clean environment the SHMS system is extremely accurate. The laboratory accuracy data represents the resolution limits of the system, i.e. the finite wordlength of the processor is one limit. Since the SHMS system is based upon an electromagnetic sensing concept, the stray magnetic fields produced by metallic objects in the cockpit will further degrade the system's accuracy.

To overcome this problem, the cockpit is surveyed or mapped to determine it's magnetic field characteristics. This mapping procedure is performed when the radiator is first installed. The mapping information is used to generate a compensation polynomial, similiar to that used to compensate for canopy distortion as discussed earlier. This polynomial is used in the SHMS microprocessor to compensate the LOS measurements for the stray magnetic fields. If it were possible to map the cockpit and generate a perfect compensation polynomial, then accuracy equivalent to that seen in the laboratory could be expected.

Modeling the Helmet-Mounted Sight Hardware

The mapping and compensation performed when the helmet-mounted sight hardware, principally the radiator, is installed in a particular

112

aircraft, removes the bulk of the aiming errors. The remaining or residual azimuth and elevation hardware errors result from our inability to map perfectly and compensate for stray magnetic fields in the cockpit.

The stray or ambient magnetic fields are a result of the magnetic materials present in the cockpit. It is assumed that the magnetic field present in the cockpit are constant for all time as long as the equipment configuration in the cockpit does not change. Magnetic materials carried into the cockpit by the pilot are not accounted for by the compensation procedure.

Unfortunately, the information to describe the residual errors is not available in the open literature. The magnitude of these residual errors are known to have a radial error standard deviation of approximately 0.4 degrees. The actual residual error data and compensation polynomial is propriatory information and the USAF has not conducted sufficient tests to estimate these errors (Ref 33).

However, the following information is known about the residual errors:

1. The residuals are spatial functions, i.e. they are time invariant, rather the error is a function of the sighting angle.

2. Over small angular segments in look angle, the errors are correlated; i.e. a measurement at -45° azimuth and a second measurement at -47° azimuth can be expected to have errors which have some degree of correlation. Tests conducted at the Aerospace Medical Research Laboratory at Wright-Patterson AFB indicate that the azimuth errors can be correlated over segments of up to 6 degrees in azimuth, while elevation errors appear correlated over segments of approximately 2 degrees in elevation (Ref 14). More

details regarding the nature of the correlation are not available at this time.

3. The errors are repeatable at each look angle, i.e. if a measurement is taken at the look angle 23° in azimuth and 8° in elevation and the helmet sight error had a value x, then at any point in time another measurement taken at that same look angle would produce exactly the same error x.

4. From the literature the overall accuracy of the state of the art HMS, expressed as a standard deviation of the radial aiming error is 0.4 degrees. Although this information does not completely describe the helmet errors it is known to be a good estimate of the magnitude of the error.

Before a model is developed from the available data it is useful to propose a method which could be used to model the helmet errors if the residual data were available in the form of a spatial power spectral density (PSD). Lacking hard data with which to develop a model the magnetic field effects satisfy the Laplace function, similiar to other field effects such as the gravitational field. As a first approximation the magnetic field effects are assumed to be adequately represented by this first order linear system (Ref 40:87). The model could then be developed as follows:

1. Curve fit the PSD data to a transfer function which is a function of angle (azimuth or elevation), in a manner similiar to that used for the vibration PSD's of the previous chapter.

2. The correlation angle Θ_c could be selected to produce a best fit to the empirical PSD data, and a linear (spatial) filter driven by

114

white Gaussian (spatial) noise as shown below:
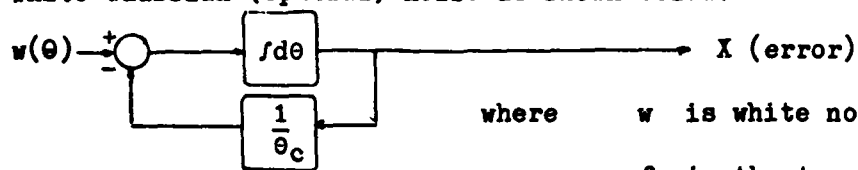
where

w is white noise

f is the transfer function

Θ is the look angle

Where the model is described by

$$\frac{dx}{d\Theta} = -\frac{1}{\Theta c} x(\Theta) + w(\Theta).$$

and

$$E\left[w(\Theta)w(\Theta + \Delta\Theta)\right] = \frac{2\sigma^2}{\Theta c} \delta(\Theta).$$

4. The discrete approximation to the linear filter can then be generated as $x_i = e^{\frac{\Delta\Theta}{\Theta_c}} x_{i-1} + w_d i$.

5. At the beginning of each LANA Monte Carlo run, the discrete approximation to the linear filter can be used to generate a sequence of azimuth and elevation errors over the entire field of view.

6. These sequences of errors can be stored as a look-up table and a linear interpolator could be used to produce the true azimuth and elevation errors for each look angle at the time of measurement update. The azimuth and elevation errors for that look angle would be added to the other errors corrupting the measurement.

7. This technique provides the desired features of repeatability at any given look angle, preserves the correlation properties of the errors, and over a sufficient number of Monte Carlo runs the results would approach, in the limit, the power spectral density functions of the original data.

Model Description. Since insufficient information exists to develop the type of model described above, an alternative method must be found

115

which uses the available information and preserves as much of the known characteristics as possible. The magnitude of the radial error, as noted earlier, is modeled as 0.4 degrees standard deviation of radial aiming error. Assuming an isotropic distribution of the residual, and using the conversion from radial errors to the bivariate normal distribution of Chapter III the value of σ is:

$$\sigma = \sigma_{AZ} = \sigma_{EL} = 0.61 \text{ deg., or } 10.65 \text{ milliradians}$$

From the preliminary experimental data the residual errors are estimated to have the following correlation intervals:

Azimuth correlation interval: 6 degrees

Elevation correlation interval: 2 degrees

Therefore the error model was constructed by generating two sequences of errors; one sequence was based on the σ_{AZ} value over the azimuth field-of-view of ± 90 degrees with a six degree correlation interval. The second sequence was based upon the value of σ_{EL} over the elevation field-of-view of ± 45 degrees, with a correlation interval of two degrees. The Polhemus HMS sight is capable of tracking the pilot LOS over $\pm 180^{\circ}$ in azimuth and $\pm 75^{\circ}$ in elevation. The field-of-view used in this model are based on the limits set in the LANA simulation. The azimuth and elevation field-of-view limits are those set by the LANA simulation. The two sequences were generated at the beginning of each Monte Carlo run by using the value of σ_{AZ} or σ_{EL} to generate two seqences of Gaussian random numbers, which have statistics such that they are of zero mean and have a standard deviation matching σ_{AZ} or σ_{EL}. These discrete number sequences were used as look-up tables, on which a linear interpolator was used over a 6 degree interval or 2 degree interval respectively to determine the azimuth or elevation error for each discrete look angle. Thus the

116

magnitude of the residual error is based upon the standard deviation
value, and the correlation between the errors drops to zero after two
sample intervals. In the case of the azimuth residual error two errors
separated by more than 12 degrees have zero correlation. Lacking hard
data these correlation interval approximations are believed to
approximate the shape of the actual autocorrelation function. Figure 7.2
is an example of what the sequences of numbers might appear like if
plotted as error magnitude versus look angle.
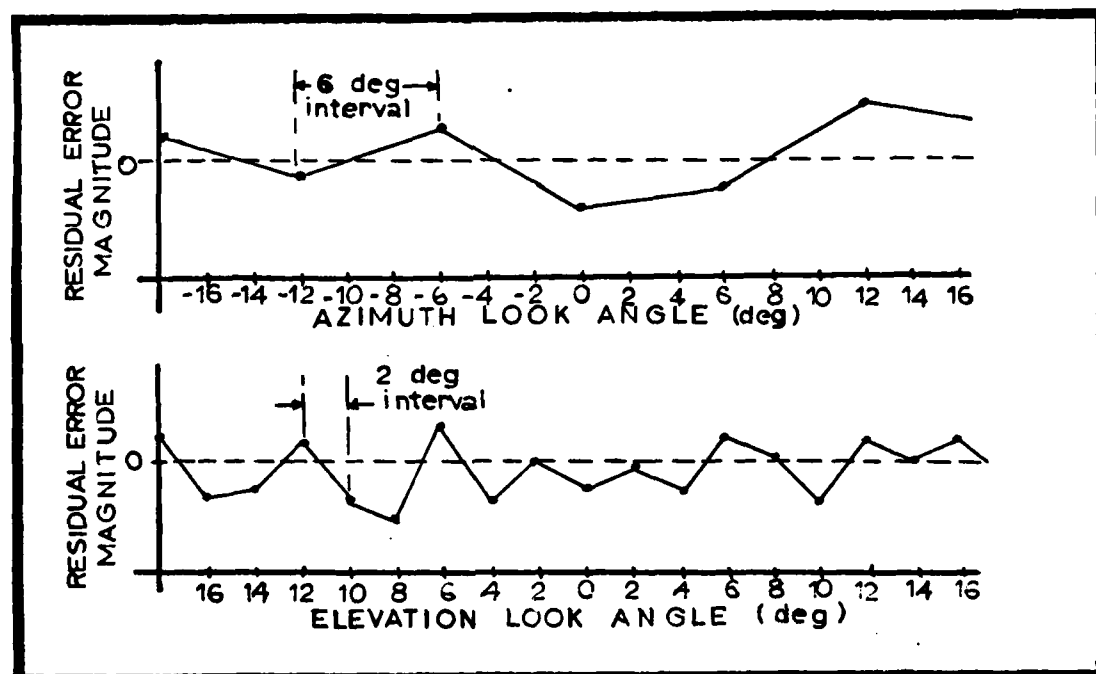
Figure 7.2   Sample Discrete Number Sequences Generated by Subroutine GAUSS

This modeling technique accurately simulated the magnitude of the
errors while preserving the correlation property that exists over the
small angular intervals. By using a look-up table, the spatial
repeatability of the errors is retained since any discrete look angle
will consistently return the same value of azimuth and elevation error to
be added to the combined measurement errors in the LANA simulation.

117

Errors Due to Boresighting the HMS

Prior to each mission the helmet-mounted sight is "boresighted"; this initialization procedure is a calibration of the system in which it derives a rotation sequence that converts values then measured by the system to zero. To boresight the helmet the operator superimposes the reticle on a reference, which is normally put on the Heads-Up Display (HUD) or the Lead Computing Optical Sight (LCOS). When the operator is satisfied with the reticle alignment with the boresight reference, the operator depresses the auto-acquisition switch on the control stick, and the system resets or calibrates this LOS as the 0 degree reference angle (Ref 32:3-4).

The boresight procedure has a radial alignment accuracy of approximately 1 milliradian, Circular Error Probable. This error is set at the instant the operator presses the auto-acquisition switch and remains constant over the duration of the mission (Ref 6). Thus the boresight error can be modeled as a random constant with 1 mr. CEP. Assuming the errors are isotropic the azimuth and elevation bivariate normal distribution one sigma values are 0.85 mr.

This boresight error model was implemented in the LANA simulation by generating an azimuth random constant truth state and an elevation random constant truth state, both of which had initial one sigma values of 0.85 mr. For each Monte Carlo run the initial one sigma values for the two boresight states were set by using the value of .85 mr in calls to the SOFE subroutine GAUSS to generate the actual initializing value.

line-of-sight bearing angle, or the target angular rate.

$$\tilde{Z}_{Az} = Z_{Az} + E_{Hu_{Az}}(\omega) + E_{Vib_{Az}}(t) + E_{Can_{Az}}(\theta) + E_{Hel_{Az}}(\theta) + E_{BS_{Az}}(t) + v_{Az} \qquad (8\text{-}1)$$

$$\tilde{Z}_{El} = Z_{El} + E_{Hu_{El}}(\omega) + E_{Vib_{Az}}(t) + E_{Can_{El}}(\theta) + E_{Hel_{El}}(\theta) + E_{BS_{El}}(t) + v_{El} \qquad (8\text{-}22)$$

where $\tilde{Z}_{Az}$ and $\tilde{Z}_{El}$ are the azimuth and elevation measurements.

Z_{Az} and Z_{El} are the sines of the true azimuth and elevation angles.

$E_{Hu_{Az}}$ and $E_{Hu_{El}}$ are the azimuth and elevation components of the human sighting error as a function of target angular rate (ω),

$E_{Vib_{Az}}$ and $E_{Vib_{El}}$ are the azimuth and elevation components of the vibration error as a function of time,

$E_{Can_{Az}}$ and $E_{Can_{El}}$ are the azimuth and elevation components of the canopy refraction error as a function of the LOS bearing angle (θ).

$E_{Hel_{Az}}$ and $E_{Hel_{El}}$ are the azimuth and elevation components of the helmet hardware error as a function of the LOS bearing angle (θ).

$E \ E_{BS_{Az}}$ and $E_{BS_{El}}$ are the azimuth and elevation components of the boresight error; this is a time dependent error model.

V_{Az} and V_{El} are the fictious noises added to each measurement to account for unmodeled errors.

121

The vibration and boresight error models, Eqs (8-1) and (8-2), are time dependent. As described in Chapter VI the vibration error is modeled as a second order Markov process for both the elevation and azimuth components of the error. The boresight error model is modeled in Chapter VII as independent random constants for the azimuth and elevation components. As shown in Table 8-1, the measurement truth states numbers 48 and 49 of the original LANA truth model (see Table 2-1) have been replaced with new truth states which represent the boresight and vibration error models. The new truth model has allocated states number 48 and 49 to the boresight random constant model, while the states numbered 50 through 53 have been used for the vibration second order Markov models. The detailed descriptions of these models are presented in Chapters VI and VII. The helmet, canopy, and human error models have each been implemented in the LANA program as function subroutines. For example, the model of the human operator supplies the value of the target's angular rate to a subroutine which determines a value of human operator error from the curves of Fig 4.5. This error is added to the measurement at each update cycle. These function subroutines are called during each measurement update cycle to contributed the appropriate value for each error source. The additive white measurement noise (v) in Eqs (8-1) and (8-2) is intended to account for the measurement errors that remain unmodeled in one of the five error components of the model. These unmodeled errors were either too small to be considered significant or there was not enough information from which to develop a model. The effects of in-flight g-forces on the human aiming accuracy is an example of the unmodeled errors. The HMS error model presented here is believed to be a reasonably accurate representation of the actual HMS errors.

Table 8.1 Original LANA Truth Error States (Ref 35)

Truth State Index	Error Source	Error Model	Initial One Sigma Value	Noise Spectral Density	Correlation Parameter
			. . . . Input Parameters		
1	East Longitude	Dynamic	221.8 Cos(LT)FT.		
2	North Latitude	Dynamic	191.1 Feet		
3	Altitude	Dynamic	30.0 Feet		
4	East Velocity	Dynamic	0.1 FT/SEC		
5	North Velocity	Dynamic	0.1 FT/SEC		
6	Vertical Velocity	Dynamic	0.1 FT/SEC		
7	East Attitude	Dynamic	0.5E-01 MRAD		
8	North Attitude	DYnamic	0.5E-01 MRAD		
9	Vertical Attitude	Dynamic	0.4 MRAD		
10	Vertical Acceleration	Dynamic	0.6E-02 FT/SEC^2		
11	X Gyro Drift	Random Walk	0.6E-02 DEG/HR	0.3E-02 (deg/Hr)^2	
12	Y Gyro Drift	Random Walk	0.3E-02 DEG/HR	0.3E-02 (Deg/Hr)^2	
13	Z Gyro Drift	Random Walk	0.5E-02 DEG/HR	0.3E-02 (Deg/Hr)^2	
14	X Gyro G-Sens Drift, Input (X)	Random Constant	0.3 DEG/HR/G		

Truth State Index	Error Source	Error Model	Initial One Sigma Value	Noise Spectral Density	Correlation Parameter
			• • • • • • Input Parameters • • • • • •		
15	Y Gyro G-Sens Drift, Spin (Y)	Random Constant	0.3 DEG/HR/G		
16	Y Gyro G-Sens Drift, Spin (X)	Random Constant	0.3 DEG/HR/G		
17	Y Gyro G-Sens Drift, Input (Y)	Random Constant	0.3 DEG/HR/G		
18	Z Gyro G-Sens Drift, Spin (Y)	Random Constant	0.3 DEG/HR/G		
19	Z Gyro G-Sens Drift, Input (Z)	Random Constant	0.2E-01 DEG/HR/G		
20	X Gyro G*G-Sens Drift	Random Constant	0.4E-01 DEG/HR/(G*G)		
21	Y Gyro G*G-Sens Drift	Random Constant	0.4E-01 DEG/HR/(G*G)		
22	Z Gyro G*G-Sens Drift	Random Constant	0.2E-02 DEG/HR/(G*G)		
23	X Gyro Scale Factor	Random Constant	300.0 PPM		
24	Y Gyro Scale Factor	Random Constnat	300.0 PPM		
25	Z Gyro Scale Factor	Random Constant	1000.0 PPM		
26	X Gyro Misalignment About Y	Random Constant	40.0 ARC SEC		
27	X Gyro Misalignment About Z	Random Constant	40.0 ARC SEC		
28	Y Gyro Misalignment About X	Random Constant	40.0 ARC SEC		
29	Y Gyro Misalignment About Z	Random Constant	40.0 ARC SEC		
30	Z Gyro Misalignment About X	Random Constant	40.0 ARC SEC		

124

Truth State Index	Error Source	Error Model	Input Parameters		
			Initial One Sigma Value	Noise Spectral Density	Correlation Parameter
31	Z Gyro Misalignment About Y	Random Constant	40.0 ARC SEC		
32	X Accelerometer Bias	Random Walk	50.0 UGEE	$(10. \text{ UGEE})^2/\text{HR}$	
33	Y Accelerometer Bias	Random Walk	50.0 UGEE	$(10. \text{ UGEE})^2/\text{HR}$	
34	Z Accelerometer Bias	Random Walk	100.0 UGEE	$(10. \text{ UGEE})^2/\text{HR}$	
35	X Accelerometer Scale Factor	Random Constant	150.0 PPM		
36	Y Accelerometer Scale Factor	Random Constant	150.0 PPM		
37	Z Accelerometer Scale Factor	Random Constant	150.0 PPM		
38	X Accel Misalignment About Y	Random Constant	30.0 ARC SEC		
39	X Accel Misalignment About Z	Random Constant	180.0 ARC SEC		
40	Y Accel Misalignment About X	Random Constant	30.0 ARC SEC		
41	Y Accel Misalignment About Z	Random Constant	180.0 ARC SEC		
42	Z Accel Misalignment About X	Random Constant	30.0 ARC SEC		
43	Z Accel Misalignment About Y	Random Constant	30.0 ARC SEC		
44	Baro Altimeter Bias	First Order Markov	100.0 FT	$0.2\text{E}+04 \text{ FT}^2/\text{NM}$	0.25E+03 NM
45	X Gimbal Misalignment	First Order Markov	4.0 MR	$0.18\text{E}-1 \text{ MR}^2/\text{NM}$	0.18E+04 SEC
46	Y Gimbal Misalignment	First Order Markov	4.0 MR	$0.18\text{E}-1 \text{ MR}^2/\text{NM}$	0.18E+04 SEC

| Truth State Index | Error Source | Error Model | . . . . Input Parameter . . . . | | |
			Initial One Sigma Value	Noise Spectral Density	Correlation Parameter
47	Z Gimbal Misalignment	First Order Markov	4.0 MR	0.18E-1 MR^2/NM	0.18E+04 SEC
48	Azimuth Boresight Bias	Random Constant	0.85E-3 RAD		
49	Elevation Boresight Bias	Random Constant	0.85E-3 RAD		
50	Azimuth Vibration Error	Second Order Markov	0.79E-2 RAD	Output State	
51	Azimuth Vibration Error	Second Order Markov	0.71E-2 RAD	Internal State	
52	Elevation Vibration Error	Second Order Markov	0.15E-1 RAD	Output State	
53	Elevation Vibration	Second Order	0.13E-1 RAD	Internal State	

126

Therefore, the one sigma value of the additive measurement noise (v) per axis. In the simulation program the value of one milliradian is used by the SOFE subroutine GAUSS to generate the additive white measurement noise that is added to the azimuth and elevation measurements at each update cycle.

Error Budget

The following error budget was developed to indicate the relative magnitudes of each of the individual error terms. The budget values are estimates of the effect of each term based upon data derived from the development of the separate error models. For example, the estimate of the vibration error (E_{Vib}) was found by solving

$$\dot{P} = FP + PF^T + GQG^T$$

with $\dot{P}$ set equal to zero. Where the P-matrix is the 2x2 covariance matrix of the azimuth or elevation vibration process. The diagonal terms of the P-matrix represent the steady-state variance values for each of the vibration states. Other terms were average values; since the human error is a function of the target angular rate, the average target rate was estimated from the simulation trajectory data to be approximately 4 degrees/second. By using the plot of Figure 4.5 the error value of 6.0 milliradians was selected for the error budget. The following are the estimates of the circular distribution standard deviation values for each of the error terms, estimated using the quantitative values from the models previosly developed. When only a single sigma is mentioned, it applies to both axes:

Helmet Hardware Error - $E_{Hel}(\Theta)$, $\sigma = 10.66$ mr

Helmet Boresight Error - $E_{BS}(t)$, $\sigma = 0.85$ mr

127

Human Error - $E_{Hu}(\omega)$,

$$\text{Errors range from } \sigma = 2.6\text{mr at 0 deg/sec to}$$
$$\sigma = 15 \text{ mr at 15 deg/sec (Figure 4.5).}$$
$$\text{Based upon an average estimated target}$$
$$\text{angular rate of 4 deg/sec}$$
$$\sigma = 6.0 \text{ mr}$$

Canopy Refraction Errors - $E_{Can}(e)$

$$\sigma_{Az} = 1.2 \text{ mr estimated from Table 5.7}$$
$$\sigma_{El} = 3.2 \text{ mr estimated from Table 5.8}$$

Vibration Errors - $E_{Vib}(t)$, by solving $\dot{P} = FP + PF^T + GQG^T$

$$\sigma_{Az} = 8.0 \text{ mr}$$
$$\sigma_{El} = 15.0 \text{ mr}$$

Additive Noise - V, $\sigma = 1.0$ mr

The cumulative effects of these errors in the simulation can be approximated by computing the Root Sum Square values as follows:

Azimuth	Elevation
$E_{Hel} = 10.66$	$E_{Hel} = 10.66$
$E_{BS} = 0.85$	$E_{BS} = 0.85$
$E_{Hu} = 6.0$	$E_{Hu} = 6.0$
$E_{Can} = 1.2$	$E_{Can} = 3.2$
$E_{Vib} = 8.0$	$E_{Vib} = 15.0$
$V = 1.0$	$V = 1.0$
RSS $\sigma_{Az} = 14.69$ mr	RSS $\sigma_{El} = 19.64$ mr
$= 0.84$ deg	$= 1.125$ deg

Filter Revision

The original fifteen state filter shown in Table 2-2 was revised by retuning to account for the changes to the truth model from the new HMS error model. The original LANA filter modeled two biases being present, one in each axis and each uses a first order Markov process with an 1800 second correlation time constant. Before considering the addition of more states to the filter, it was decided to attempt to re-tune the existing filter states. The filter measurement noise statistics on states numbers 14 and 15 were revised as shown in Table 8-2. The correlation time constant was set to 0.3 seconds, to match the time constant of the vibration second order Markov states. As shown in the error budget, the vibration error terms are the largest single error source. They also have the shortest time constant of all the errors.

The intial one-sigma values for the two filter measurement states were made equal to the RSS values of the error budget. The noise spectral density was calculated using the state time constant and the RSS error budget values as follows: (Ref 29:185)

$$Q = \frac{2\sigma^2}{T}$$

where Q is the noise spectral density

T is the correlation time constant

σ is the RSS one sigma value

Thus, the measurement dynamics model is tuned by revising the time constant and the RSS error budget one sigma value to match the noise spectral density generated by the five error terms. The measurement noise matrix (R) was revised by matching it to the RSS one sigma values.

Performance and Sensitivity Analysis

In order to illustrate the effects of the new helmet-mounted sight

129

Table 8.2 Revised Filter Error States

Filter State Index	Error Source	Error Model	Initial One Sigma Value	· · · · · · Input Parameters · · · · · · Noise Spectral Density	Correlation Parameter
1	East Longitude	Dynamic	221.8 Cos(LT)FT		
2	North Latitude	Dynamic	191.1 FT		
3	Altitude	Dynamic	30.0 FT		
4	East Velocity	Dynamic	0.1 FT/SEC		
5	North Velocity	Dynamic	0.1 FT/SEC		
6	Vertical Velocity	Dynamic	0.1 FT/SEC		
7	East Attitude	Dynamic	0.5E-1 MR		
8	North Attitude	Dynamic	0.5E-1 MR		
9	Vertical Attitude	Dynamic	0.4 MR		
10	Baro Altimeter Bias	First Order Markov	100.0 FT	$0.24E+4$ FT^2/NM	$.25E+3$ NM
11	X Gyro Drift	Random Walk	0.3E-2 DEG/HR	$(.36E-2$ DEG/HR$)^2$/HR	
12	Y Gyro Drift	Random Walk	0.3E-2 DEG/HR	$(.36E-2$ DEG/HR$)^2$/HR	
13	Z Gyro Drift	Random Walk	0.5E-2 DEG/HR	$(.6E-2$ DEG/HR$)^2$/HR	
14	Azimuth Measurement Bias	First Order Markov	0.842 DEG	$.47E+01$ DEG^2/SEC	0.3 SEC
15	Elevation Measurement Bias	First Order Markov	1.124 DEG	$.84E+01$ DEG^2/SEC	0.3 SEC

error model on the original and revised LANA filter performances, the following series of Monte Carlo studies were conducted:

Number of Monte Carlo Runs	Truth Model	Filter Model	Comments
A. 30	Original	Original	Free inertial performance test with all measurements turned off.
B. 30	Original	Original	
C. 30	New	Original	Illustrates effects of new errors
D. 30	New	Revised	Revised filter performance

Studies B, C, and D are HMS aided inertial studies with both azimuth and elevation measurements simulated. The following series of Monte Carlo studies were also performed to illustrate performance sensitivity to each of several individual error sources.

Number of Monte Carlo Runs	Truth Model	Filter Model	Error source studied and percentage of nominal error value
20	New	Revised	Helmet errors (E_{Hel}), one sigma at 100% of normal value. All other errors at normal values.
20	New	Revised	Human errors (E_{Hu}), one sigma at 110% of normal value. All other errors at normal values.
20	New	Revised	Canopy errors (E_{Can}), one sigma at 110% of normal value. All other errors at normal values.
20	New	Revised	Boresight errors (E_{BS}), one sigma at 110% of normal value. All other errors at normal values.
20	New	Revised	Vibration errors (E_{Vib}), one sigma at 110% of normal value. All other errors at normal values.
20	New	Revised	Measurement noise (V), one sigma at 150% of normal value. All other errors at normal values.

20		New	Revised	All errors set to zero; this gives the performance of the system as if it were receiving perfect measurements.
20		New	Revised	All errors at their normal values, to be used as a baseline to compare with the above studies.

The five error states described in the previous chapters were all subjected to a sensitivity study as shown above. The one sigma value of the particular error term being studied was increased to 110 percent of its normal value. The remaining error terms were left at their normal values. The white measurement noise value was increased to 150 percent of it's normal value to evaluate the sensitivity of the model and filter to very large changes in the noise value, since the strength of the unmodeled error could be much larger than assumed.

The sensitivity studies were performed using only 20 Monte Carlo runs versus the standard 30 runs to conserve computer resources and speed the run time of the programs. Therefore it is necessary to demonstrate that 20 runs are still a valid statistical representation of the system performance. To check this assumption a plot program was written to overplot on the same graph the system performance index, in this case the CEP of RMS position error was used. Using the data file from the 30 run study performed with the new truth and filter models, plots of the CEP values for the 10, 15, 20, 25, and 30 runs were generated. For the ensemble of error realizations over 30 runs, Figure 8-1 shows the five CEP plots. The lower plot line is the 10 run plot, while the upper line is the 30 run plot. From these plots it is apparent that the 20 and 25 run studies produce results which are consistent with those obtained from the full 30 run study. It is therefore acceptable and practical, in this case, to use only 20 Monte Carlo runs to perform the sensitivity studies.
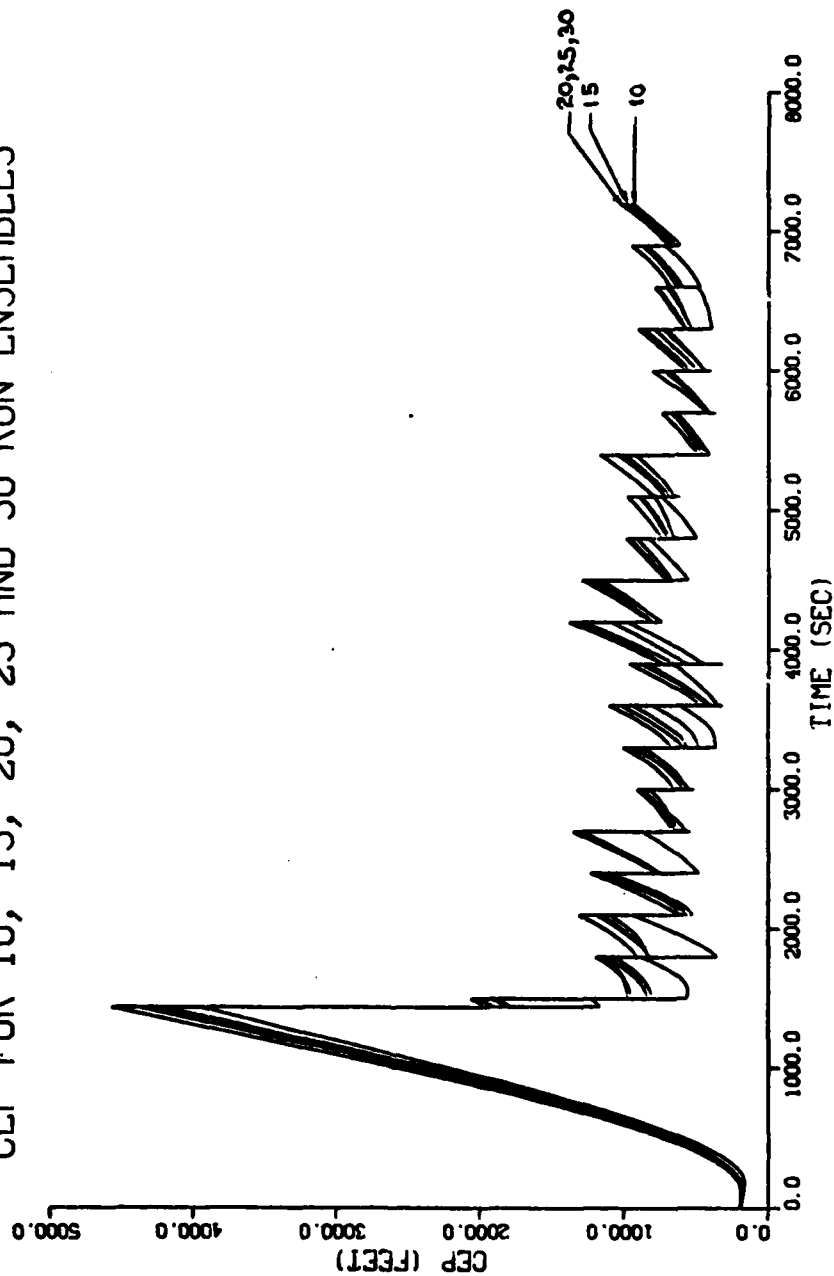
Figure 8.1 Overplots of the CEP of Actual RMS Position Errors for 10, 15, 20, 25, and 30 from the Same 30 Run Study.

IX Results

This chapter presents the results from the performance and
sensitivity studies described in Chapter VIII. At this point it is
important to emphasize that the actual results of this thesis are and
were intended to be the development of the error models for the
Helmet-Mounted Sight system. The performance and sensitivity analysis
was not intended to be a rigorous demonstration of the tuning of a Kalman
filter or the implementation of these error models in a simulation
program. Rather these analyses were performed to illustrate some of the
effects that a more realistic error model can have upon the performance
of a navigation system simulation.

Performance Index

In order to show the results of the performance and sensitivity
studies some form of performance indicator or index was required. Two
indices of performance were chosen based upon the nature of the LANA
mission. During the LANA mission simulation, the pilot must accurately
navigate his aircraft to the target area. In this phase of the flight
the aircraft position estimate is the critical measure of performance.
Theefore, the Circular Error Probable (CEP) plot of the aircraft actual
and estimated Root Mean Square (RMS) horizontal position errors was
chosen as one of the performance indexes. Upon arrival at the target
zone, the pilot makes visual or sensor contact with the target and at
this time the critical factor for weapon delivery becomes the estimates
of the aircraft velocity. Therefore, the second performance index was
chosen to be the plot of the Root Sum Square (RSS) of the actual east,
north, and vertical velocity error one sigma values.

134

The plots shown in this section were generated by using the SOFE companion plotting program called SOFEPL, "A Plotting Postprocessor for SOFE" (Ref 46). Both the CEP and RSS of velocity plots are SOFEPL type 18 plots. The CEP plot is based on latitude (Lat) and longitude (Long) position errors and has two curves. One curve is the CEP as computed from actual RMS position errors which are formed by differing the truth and filter states. The other curve is CEP as computed from Lat. and Long. sigmas from the filter covariance matrix; this curve represents the filter estimate of the horizontal position error. The plot of the RSS of the velocity error was computed using the difference of the truth and filter states to calculate one sigma values in each of three axes and then finding the RSS of the three velocity sigmas.

Free-Inertial Performance

The simulated flight profile extends over a period of 7200 seconds. For the first 1440 second the flight is over water during which time no position updates are available. Landfall occurs at 1440 seconds at which time the aircraft enters a terrain following mode and begins to take updates. The flight profile approaching and exiting the target zone contains a number of turns and jinking maneuvers. Plots of the flight profile are shown in Figure 9.1.

To demonstrate the unaided or free-inertial performance of the LN-15 local-level inertial navigation platform, a 30 run Monte Carlo study was conducted without measurement updates. The baro-altimeter model was retained to stabilize the vertical channel, but no HMS position updates were provided. The results of this study are shown in Figures 9.2(a) and 9.2(b). The CEP position error plot of Figure 9.1 shows that after only

135
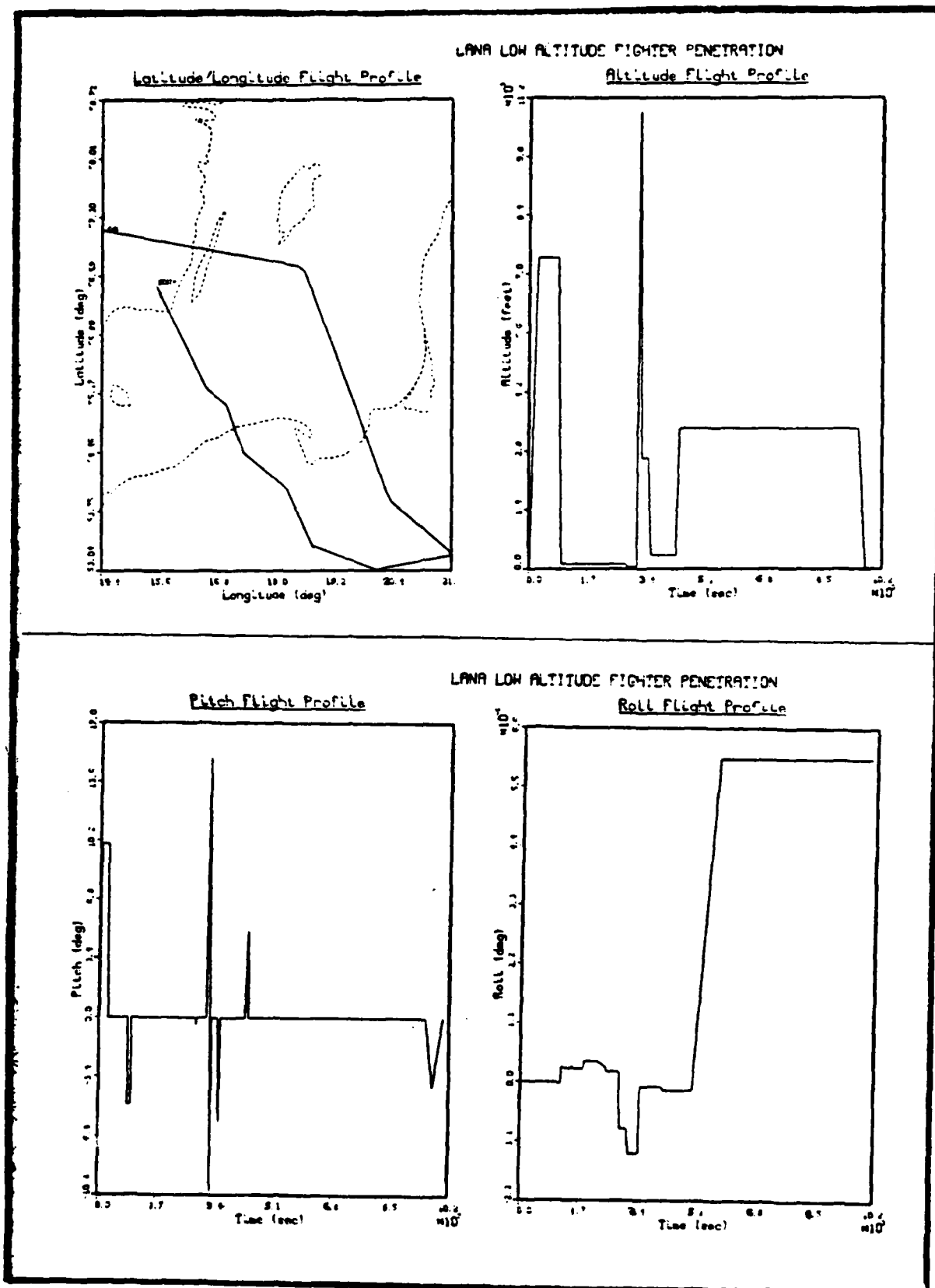
Figure 9.1   LANA Flight Trajectory

CEP FROM ACTUAL RMS ERROR AND COVARANCE DATA
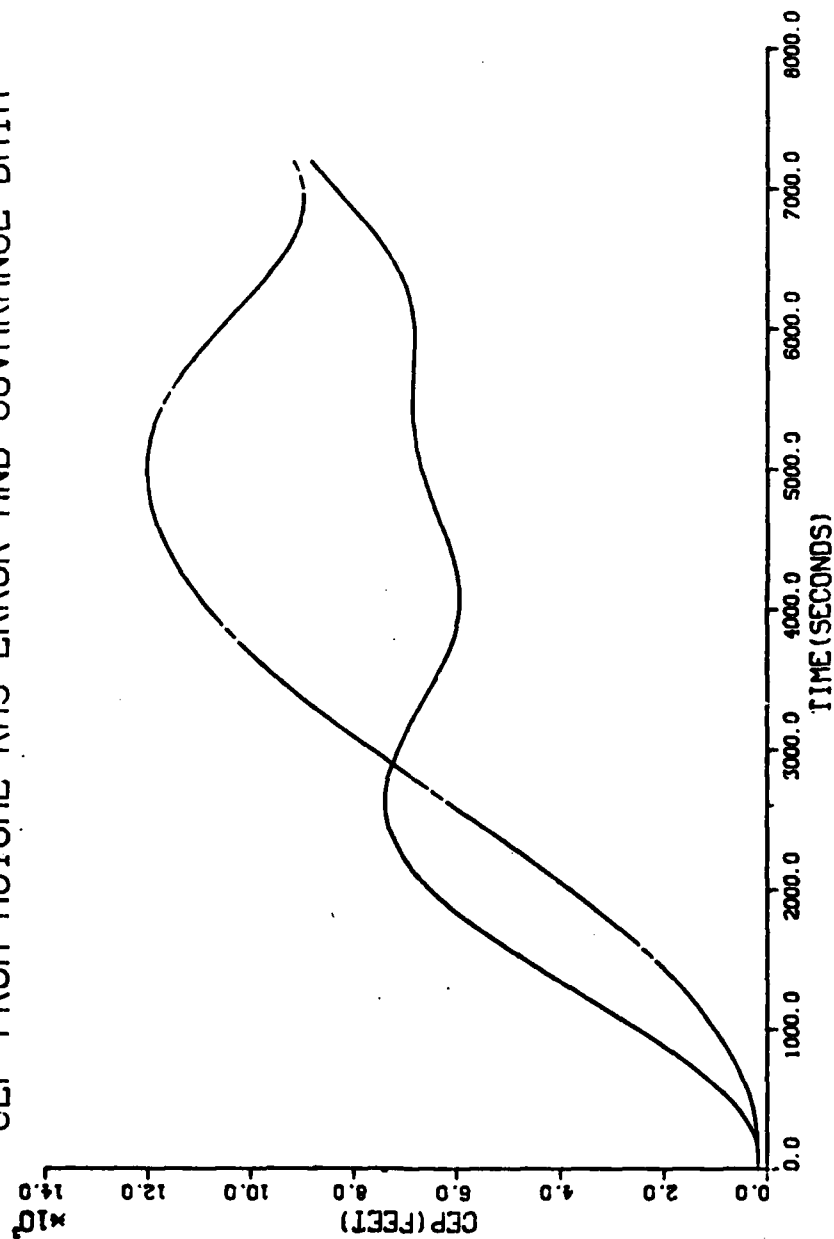
Figure 9.2(a) Free Inertial Performance - Actual CEP (solid line) and Predicted CEP (broken line)
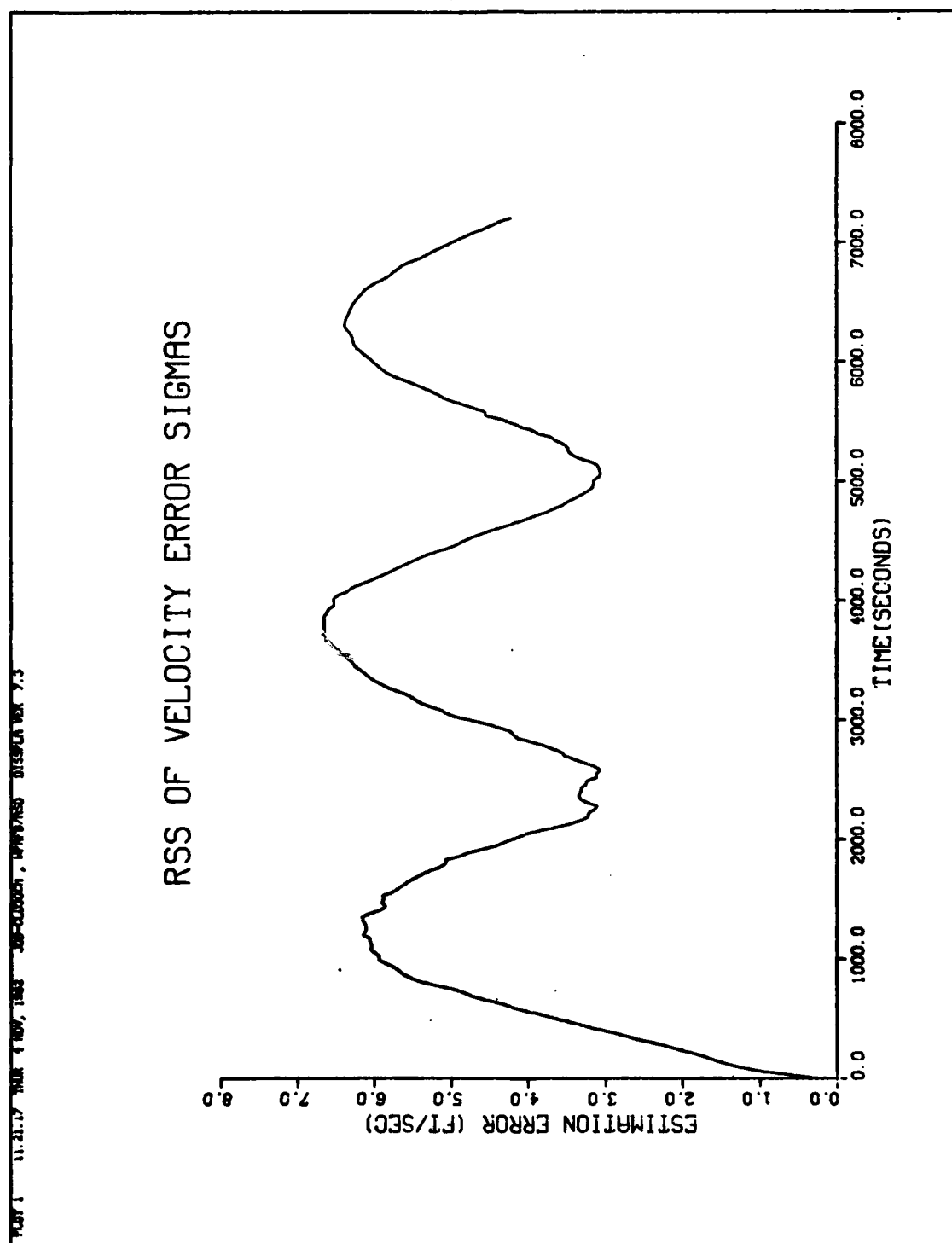
Figure 9.2(b) Free Inertial Performance – RSS of Actual East, North, and Vertical Velocity One Sigma Values

138

2500 seconds (43 minutes) the CEP value is about 7600 feet. By the end
of the mission the error has grown to 8800 feet. The CEP plot of the
filter covariance values indicates that the free inertial filter estimate
follows the acutal error growth reasonably well.

The plot of the Root Sum Squared values of the east, north, and
vertical velocity error one sigma values, is shown in Figure 9.2. These
velocity errors rapidly climb to 6 feet per second and then oscillate
between 3 and 6 feet per second for the remainder of the mission. The
position CEP and the RSS of velocity error plots demonstrate the need for
some method of position aiding for this inertial platform to improve it's
accuracy.

Original LANA Performance

The performance of the original filter against the old or original
helmet-mounted sight truth model is shown in Figures 9.3 and 9.4. The
original LANA system employs a simplified model for the HMS errors. The
original LANA truth and filter models for the HMS measurement errors uses
two first order Markov processes, one for each of the azimuth and
elevation components. These Markov processes head a correlation time
constant of 300 seconds and an initial one sigma value of 0.28 deg (see
Table 2.2). These urdocumented measurement models were "best guess"
estimates of the measurement errors. The plot of the CEP of the RMS
position errors, shown in Figure 9., indicates the growth in position
error from the beginning of 'he mission until the 1440 second point. At
this time position updates from the HMS begin and the position error
settles down to an approximate average value of 600 feet. The plot of
the RSS velocity error values, shown in Figure 9.4, also show a growth in
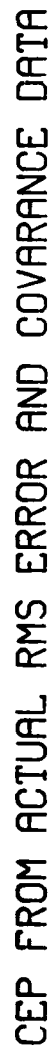
139

CEP FROM ACTUAL RMS ERROR AND COVARIANCE DATA

Figure 9.3 Original LANA Performance — Actual CEP (solid line) and Predicted CEP (broken line)
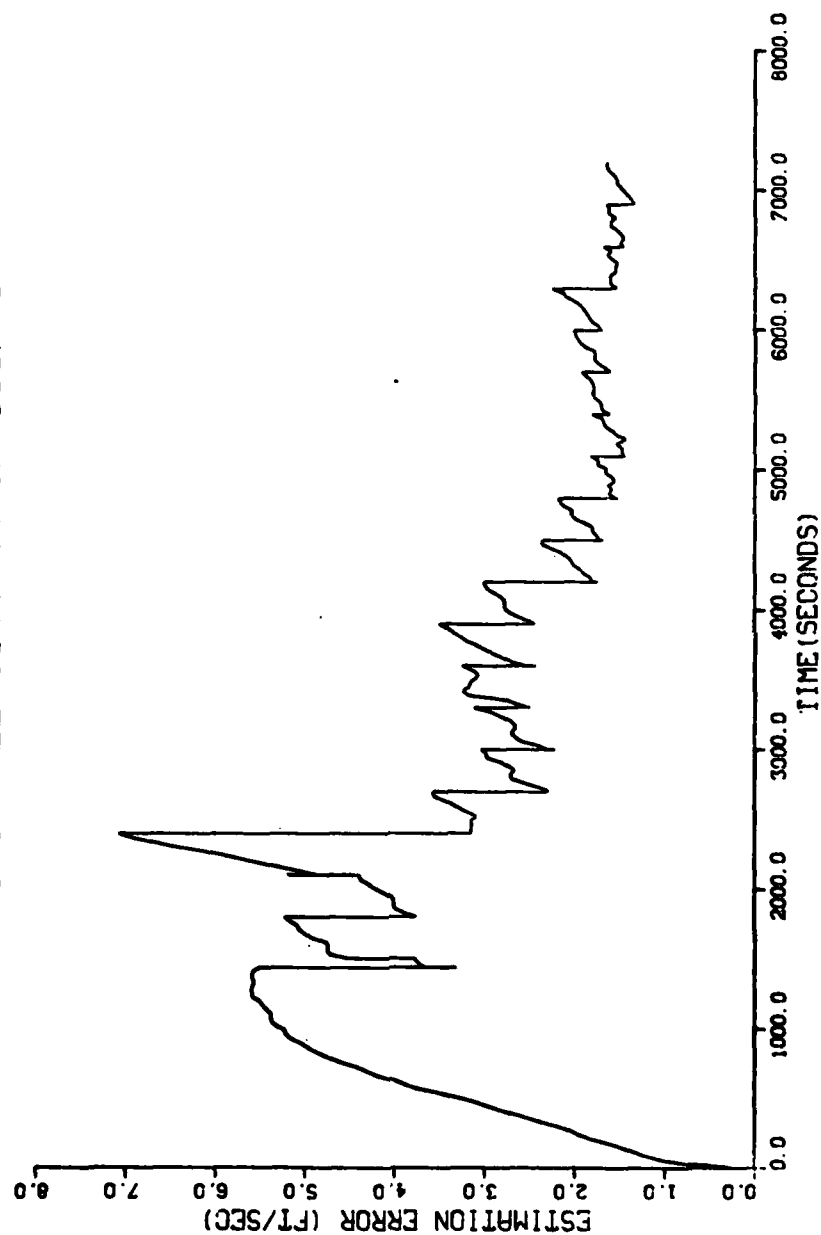
Figure 9.4 Original LANA Performance - RSS of Actual East, North, and Vertical Velocities
One Sigma Value

the error until the beginning of position updates at the 1440 second

point. Thereafter, the velocity error value stabilizes at approximately

1.5 feet/second.

New HMS Truth Model and Original Filter

The change in the performance of the LANA system, when the original

HMS truth model is replaced by the models developed in the previous

chapters, is shown in Figures 9.5 and 9.6. This 30-run Monte Carlo study

was intended to illustrate the effect of more realistic truth model upon

the original filter's performance. The plot of the CEP of the actual RMS

position error, shown in Figure 9.5, indicates the growth in error when

compared with Figure 9.3. The average CEP values grows from 600 ft to

approximately 2600 ft or a 300% increase. The RSS of actual velocity

errors increases from 1.5 to 3.5 ft/sec for a 130% increase. Despite the

different truth model, the CEP of the filter position covariance values

still dominates the actual position error from the 2000 second point in

the mission onward. The plot of the RSS of velocity error one-sigma

values, shown in Figure 9.6, indicates that the new HMS truth model has

caused the velocity errors to increase to between three and five feet per

second.

New HMS Truth Model and Revised Filter Model

The plots of Figure 9.7 and 9.8 show the improvement in the LANA

system performance when the Kalman filter is revised to account for the

new HMS truth model. Recall that the following actions, given in Chapter

VIII were performed to return the filter model:

     a. Revise the values of the dynamical model

        1. $T = 0.03$ sec
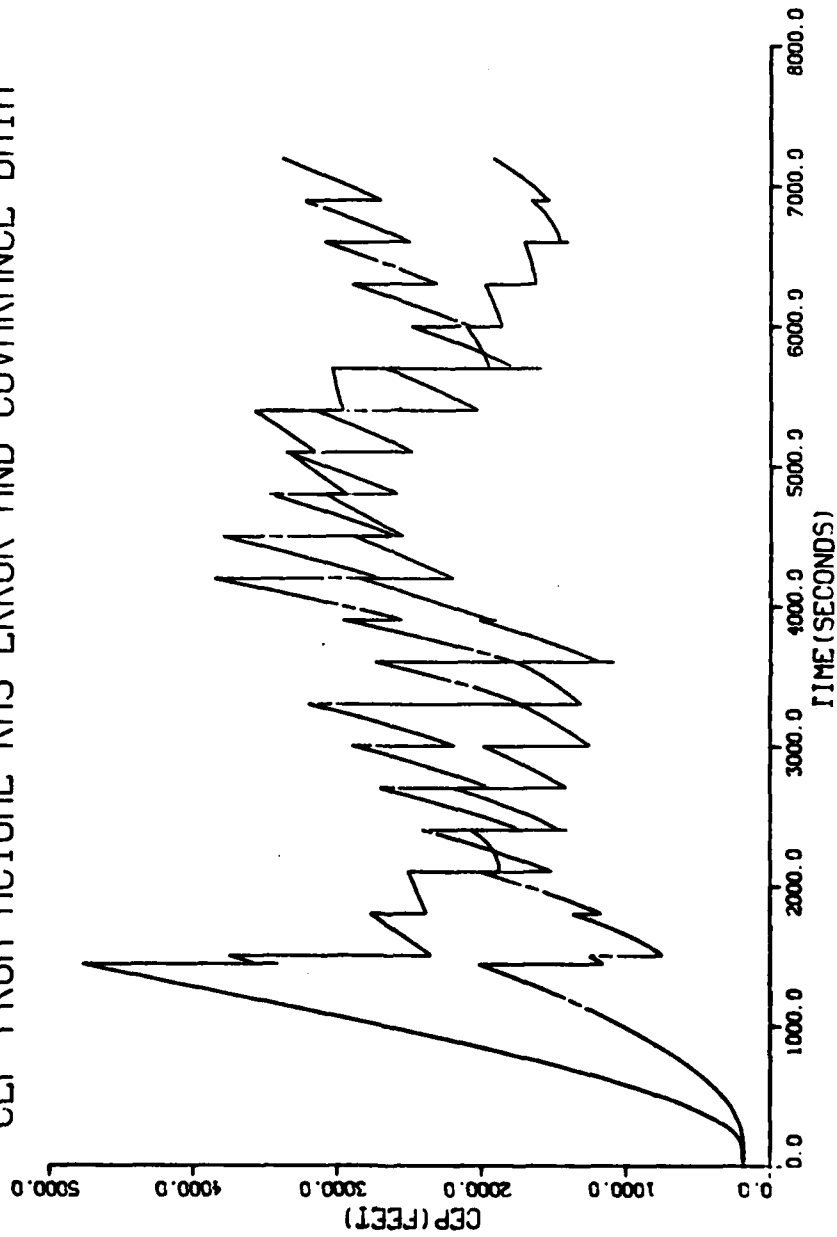
Figure 9.5 New HMS Truth and Original Filter Models - Actual CEP (solid line) and Predicted CEP (broken line)
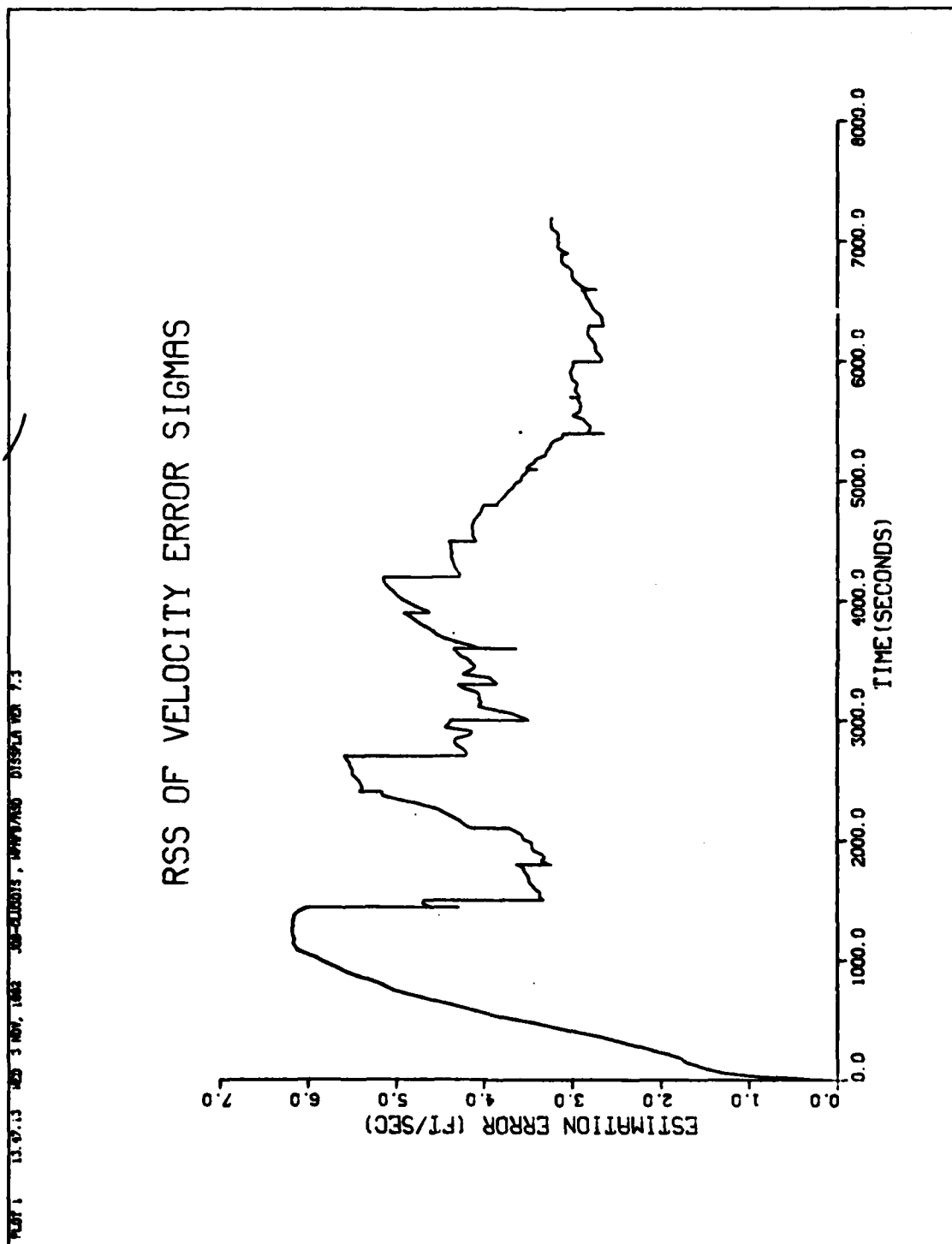
Figure 9.6 New HMS Truth and Original Filter Models – RSS of Actual East, North, and Vertical Velocity Errors, One Sigma Values

CEP FROM ACTUAL RMS ERROR AND COVARANCE DATA
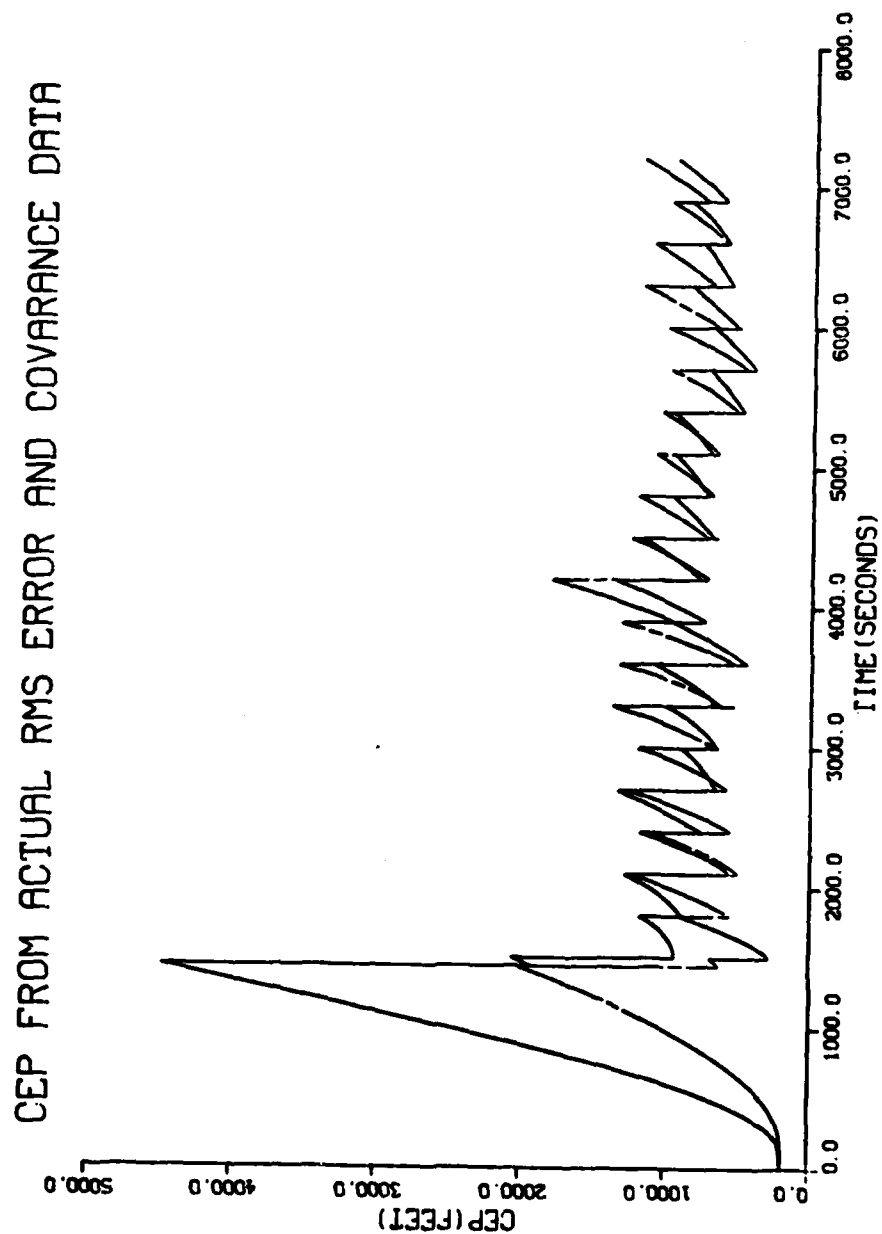
Figure 9.7   New Truth and Revised Filter Models – Actual CEP (solid line) and
Predicted CEP (broken line)
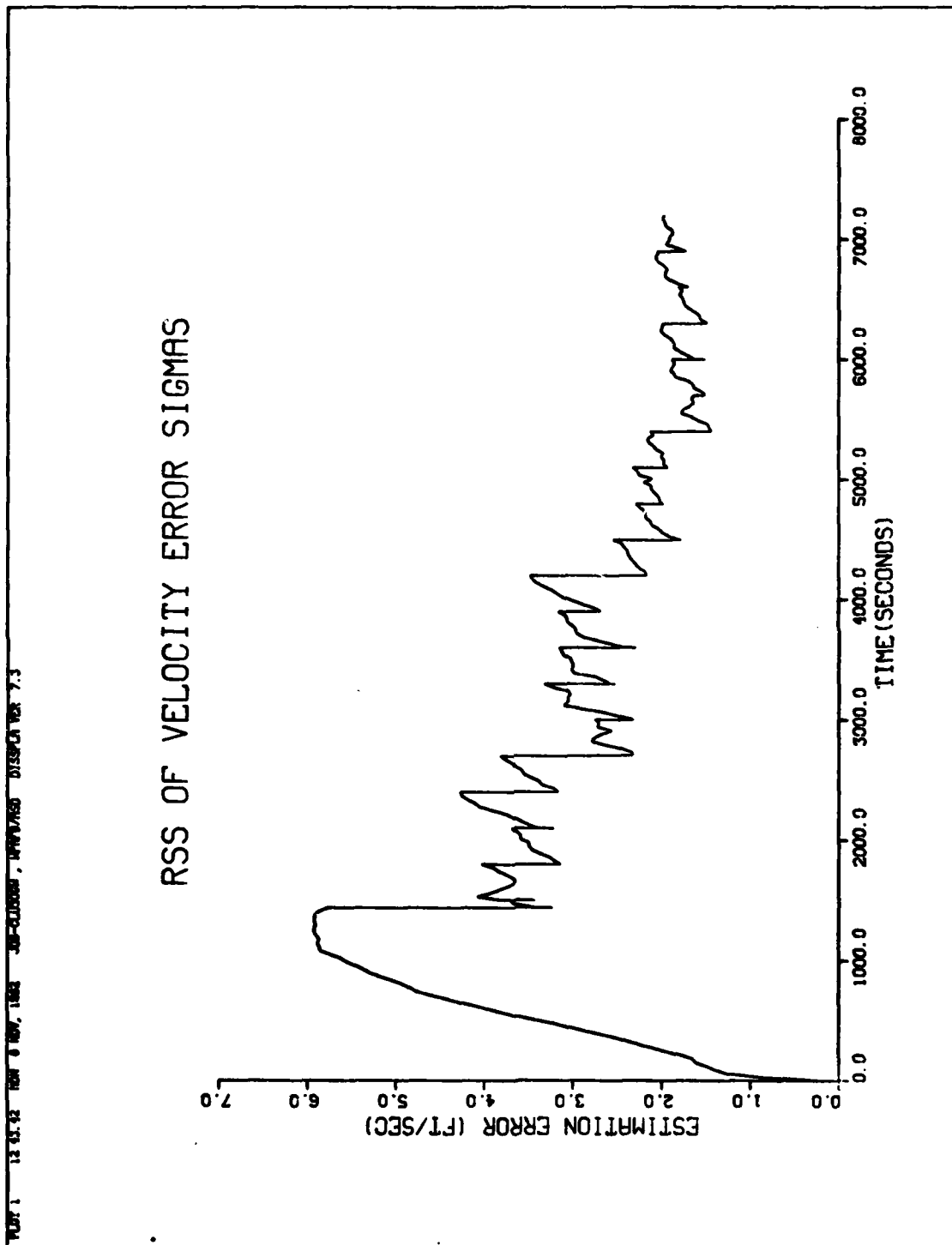
Figure 9.8 New Truth and Revised Filter Models - RSS of Actual East, North, and Vertical Velocity Errors, One Sigma Values

2. Matched Q $-\sigma\,\mathrm{RSS}_{Az}$ = 0.84 deg.

$-\sigma\,\mathrm{RSS}_{El}$ = 1.12 deg.

b. Alter the measurement noise matrix (R) by matching it to RSS error budget values.

The plot of the CEP of actual position errors, shown in Figure 9.7, demonstrates that the filter revision has reduced the average position error to approximately 670 feet. The actual RSS of velocity errors now has an average value of approximately 2.0 ft/sec. It is not necessarily surprising that the position error is still larger than that seen in the original filter performance with the original truth model. Since we are now trying to estimate larger and more complex HMS errors with exactly the same number of filter states, the filter may not perform as well. However, a·uming that the new HMS truth model is much closer to the real world errors, then the original filter if used in a real system would be expected to have performance values closer to those shown in Figure 9.7 than to those in Figure 9.3.

Once again the growth in position error is rapid during the first 1440 seconds of the mission until position updates begin. After the 2000 second point in the mission, the plot of the filter covariane values for position error indicates that the actual position errors are closely tracked by the filter. The plot of the RSS of the velocity error component one sigma values, shown in Figure 9.8, indicates that once the position updates begin the velocity errors decrease, and after the 5000 second point in the mission they stabilize at approximately 1.5 feet/second.

To demonstrate that the revised filter has been properly tuned, an

147

ensemble of additional plots have been included in this section. These
plots, Figures 9.9 to 9.16, were intended to verify that the filter
states track the truth states. To illustrate that the filter is tuned,
the north position, velocity, and tilt plots from a specific case (run
number 14) are presented. Figures 9.9 and 9.10 show that for a single
Monte Carlo run the filter estimate of the north position closely tracks
the actual position error. The same close tracking performance of the
filter is shown for the velocity and tilt states in Figures 9.11 through
9.14. Figures 9.15 and 9.16 shows that the actual covariance values are
bounded by the filter covariance estimates.

Sensitivity Analysis

To provide an indication of how sensitive the filter may be to
changes in any of the individual HMS error terms, an abbreviated
sensitivity analysis was performed. It is an abbreviated analysis in the
sense that the sensitivity of each error source was only studied at one
value, that being 110% of the normal one sigma value. This was done to
conserve computer resources and because this was not intended to be a
detailed study. Normally a full 30 run Monte Carlo study would be
performed at possibly 80%, 90%, 95%, 105%, 110%, and 120% of the normal
value, for each error term. The single value analysis of each term is
intended to give a preliminary indication of filter sensitivity. The
sensitivity study for the additive white measurement noise (v) was done
at 150% of its normal one sigma value. This figure was chosen because
the estimate of the additive noise to account for unmodeled errors has
the highest probability of being inaccurate. The results of these
sensitivity studies are discussed later in this chapter.

148
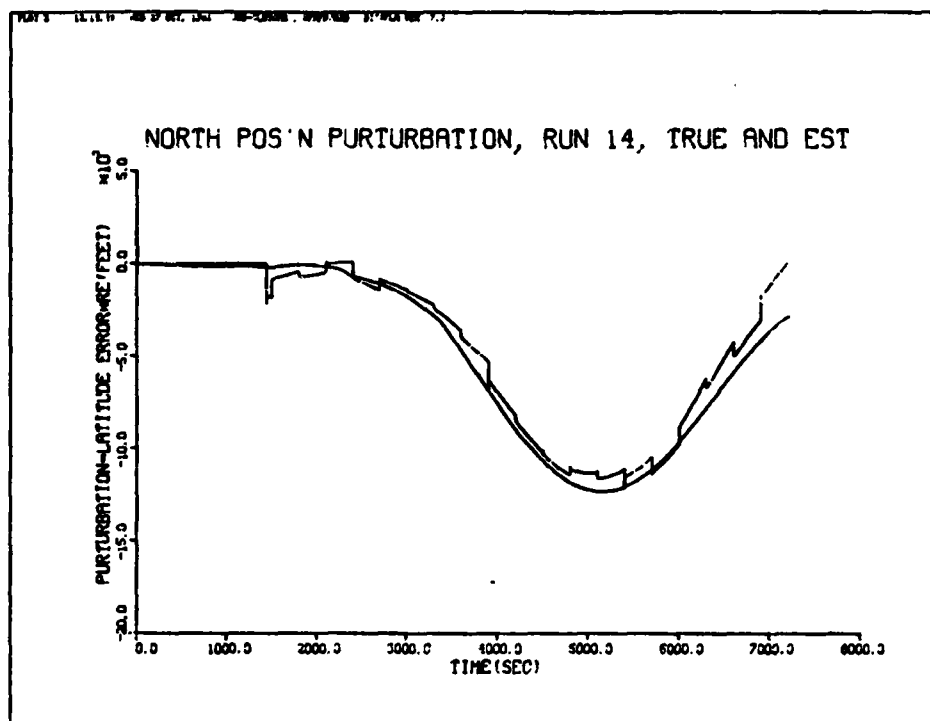
Figure 9.9 New Truth and Revised Filter Models Plot of Latitude
Truth State (solid line) and Latitude Filter State
(broken line) SOFEPL Plot Type 3
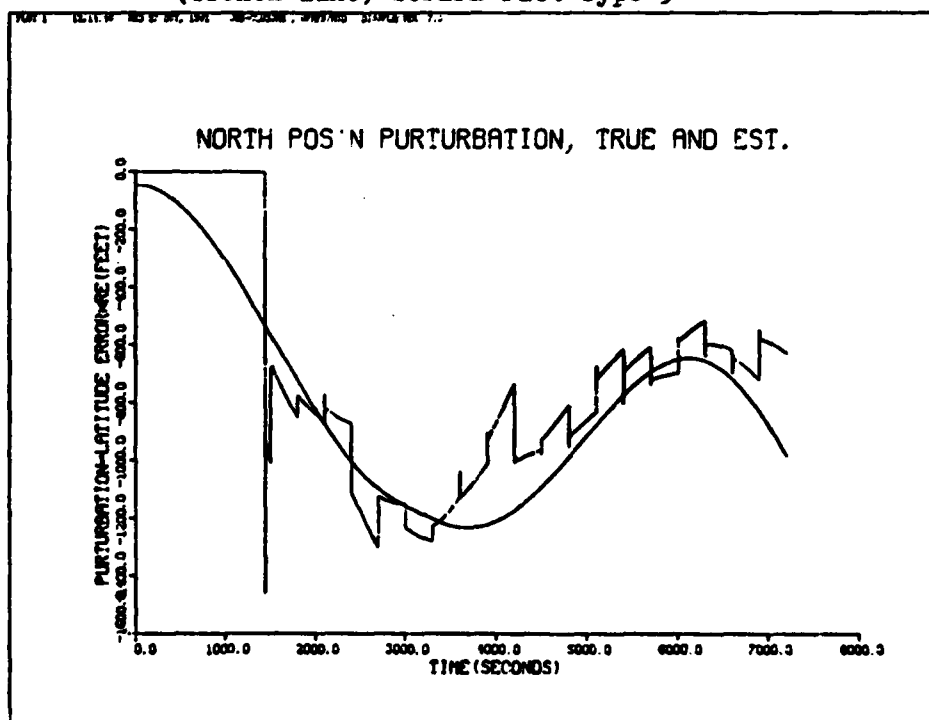
Figure 9.10 New Truth and New Filter Models - Plot of the average of
lat. truth state (solid line) and average of lat. filter
state (broken line).

149

NORTH VEL. PURTURBATION, RUN 14, TRUE AND EST.
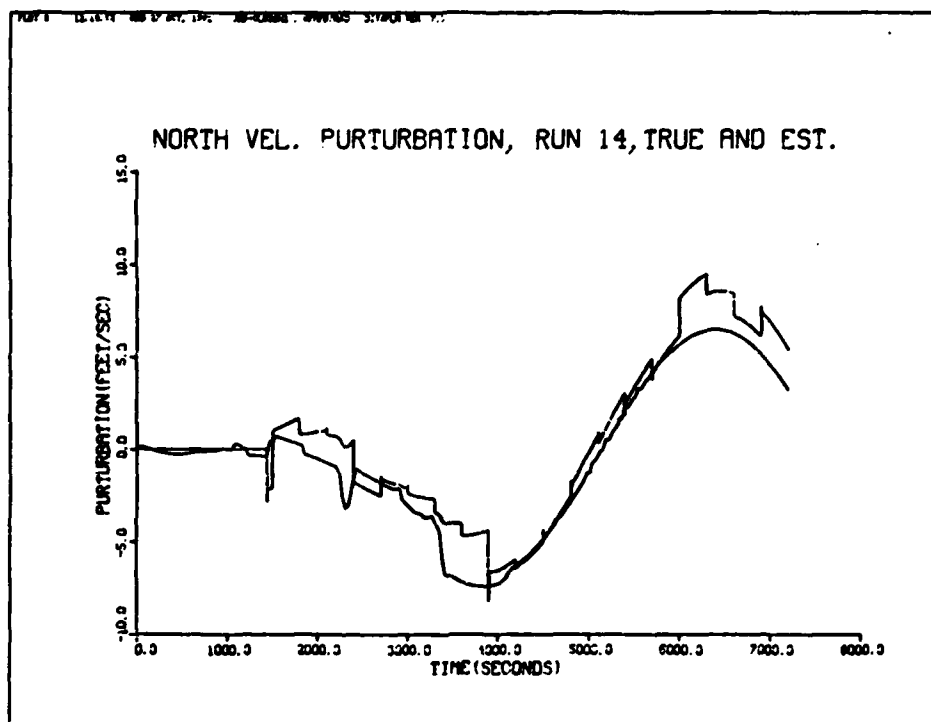
Figure 9.11   New Truth and Revised Filter Models - Plot of North
                Velocity Truth State (solid line) and North Velocity
                Filter State (broken line).

NORTH VEL. PURTURBATION, TRUE AND EST.
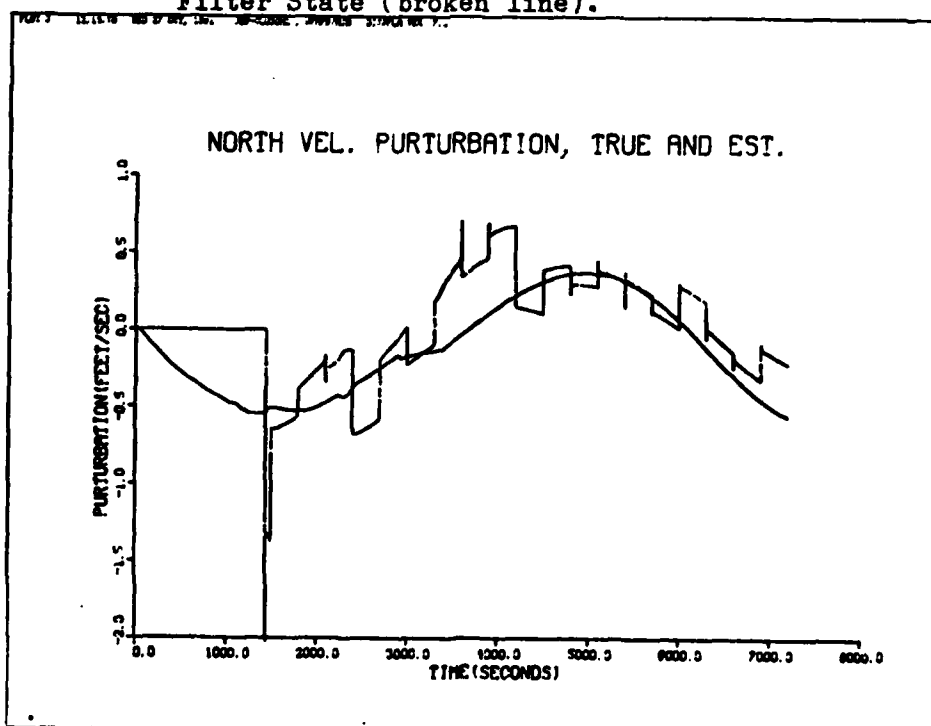
Figure 9.12   New Truth and Revised Filter Models - Plot of the Average of
                North Velocity Truth State (solid line) and the Average of
                North Velocity Filter State (broken line).

150
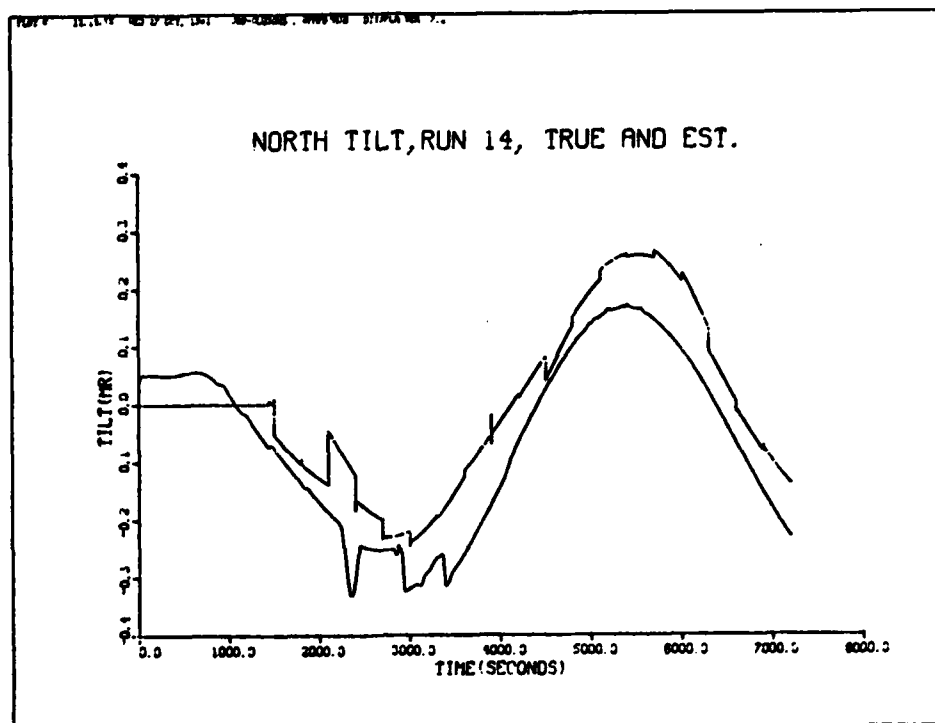
Figure 9.13 New Truth and Revised Filter Models – Plot of North Tilt Truth State (solid line) and the North Tilt Filter State (broken line).
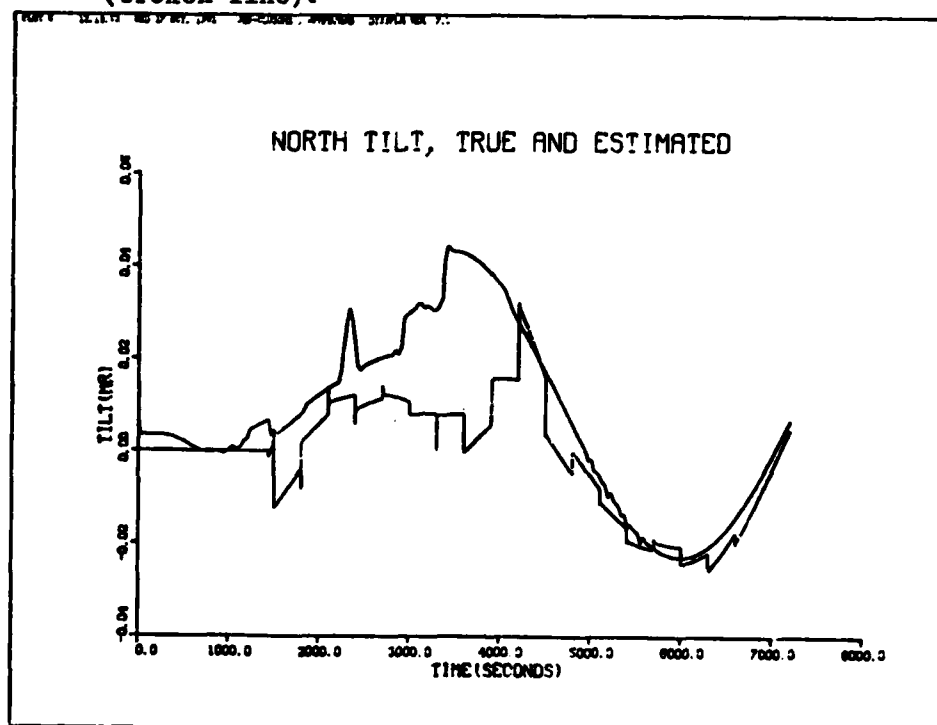
Figure 9.14 New Truth and Revised Filter Models – Plot of the Average of the North Tilt Truth State (solid line) and the Average of the North Tilt Filter State (broken line).

151

EAST POSITION EST. ERROR, +-1PF AND 1 TRUE SIGMA
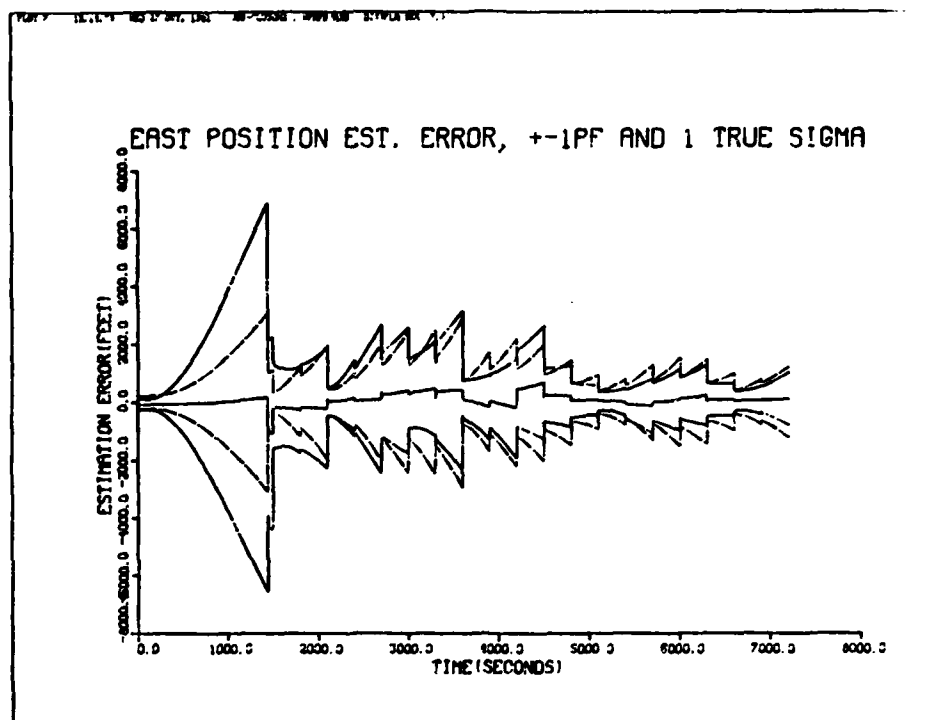
Figure 9.15 New Truth and Revised Filter - Plots of the Difference of
East Vel. Truth and Filter States (solid line), Plus and Minus one Std.
Dev. of this Difference (broken line), and Plus and Minus Filter Std.
Dev. (dashed line), Plot Type 14.

EAST VEL. EST. ERROR, +-1PF AND 1 TRUE SIGMA
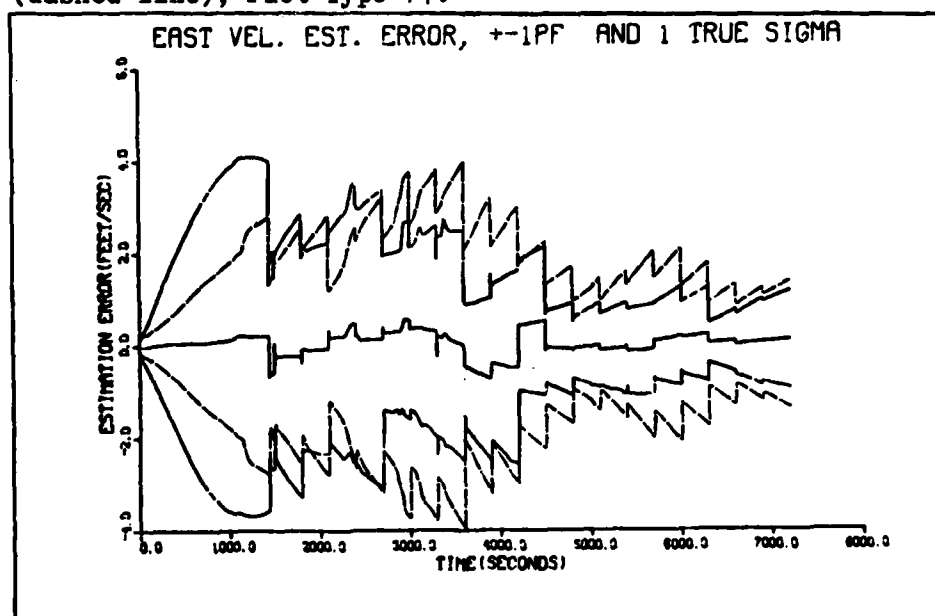
Figure 9.16(a) New Truth and Revised Filter - Plots of the Differences
of East Pos'n Truth and Filter States (solid line), Plus and Minus One
Std. Dev. of this Difference (broken line), and Plus and Minus Filter
Std. Dev. (dashed line).

152

EAST TILT EST. ERROR, +-1PF AND 1 TRUE SIGMA
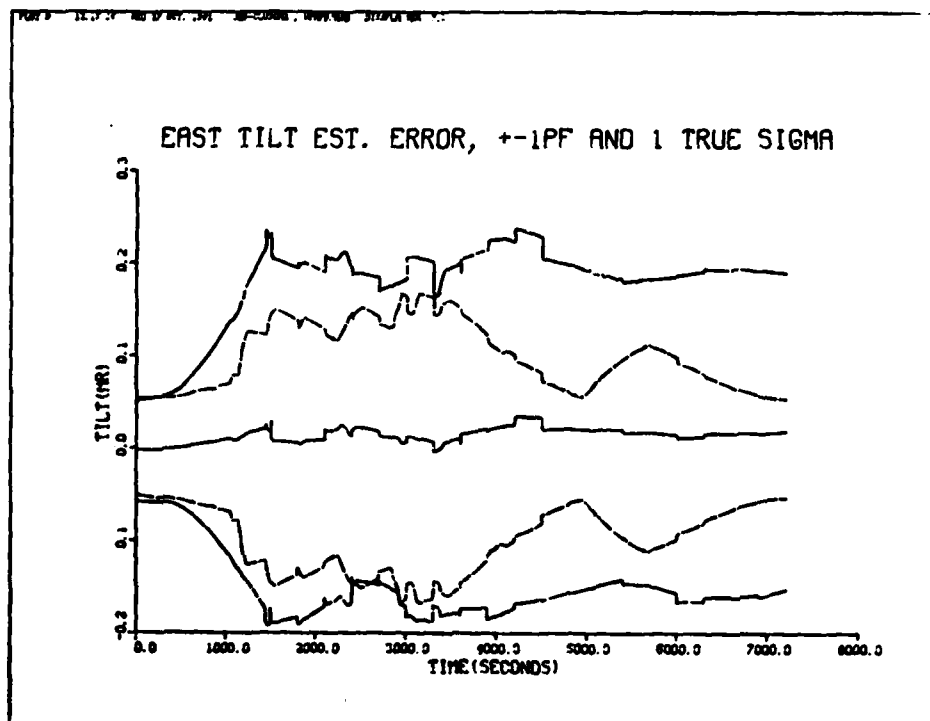
Figure 9.16(b)   New Truth and Revised Filter – Plots of the Difference
of East Tilt Truth and Filter States (solid line), Plus
and Minus One Std. Dev. of this Difference (broken line)
Plus and Minus Filter Std. Dev. (dashed line).

153

The plots of the CEP of position errors and the RSS of velocity errors, for the new truth and revised filter models, with all the errors at their normal values are shown in Figures 9.17a and 9.17b. These plots are the baseline against which the other sensitivity studies are compared. Figures 9.17a and 9.17b represent the same error conditions as used for Figures 9.7 and 9.8. Because the sensitivity studies use only 20 Monte Carlo runs, Figures 9.7 and 9.8 cannot be exactly compared with sensitivity plots, due to the 30 run vs 20 run difference shown in Figure 8.1.

Zero Error Condition

A 20-run Monte Carlo study was performed with all the HMS truth model error terms set equal to zero. Only the truth model was changed, the filter remained the same. With all the measurement error removed the HMS measurements were essentially perfect. The plots of actual and predicted position CEP, Figure 9.18, and the RSS of actual velocity errors, Figure 9.19, illustrate the improvement in performance. These figures show that with all the HMS error sources "turned off" the CEP drops for 600 ft to approximately 250 ft while the RSS of actual position errors approached 1.0 ft/sec. By comparing the actual position and velocity errors from these plots with those of Figures 9.7 and 9.8, the contribution of the HMS errors to the total system errors becomes apparent.

HMS Error Sensitivity Studies

The results of the sensitivity studies performed on the six HMS system error terms are shown in Figures 9.20 to 9.31. These plots show the CEP of position errors and the RSS of the velocity error one sigma
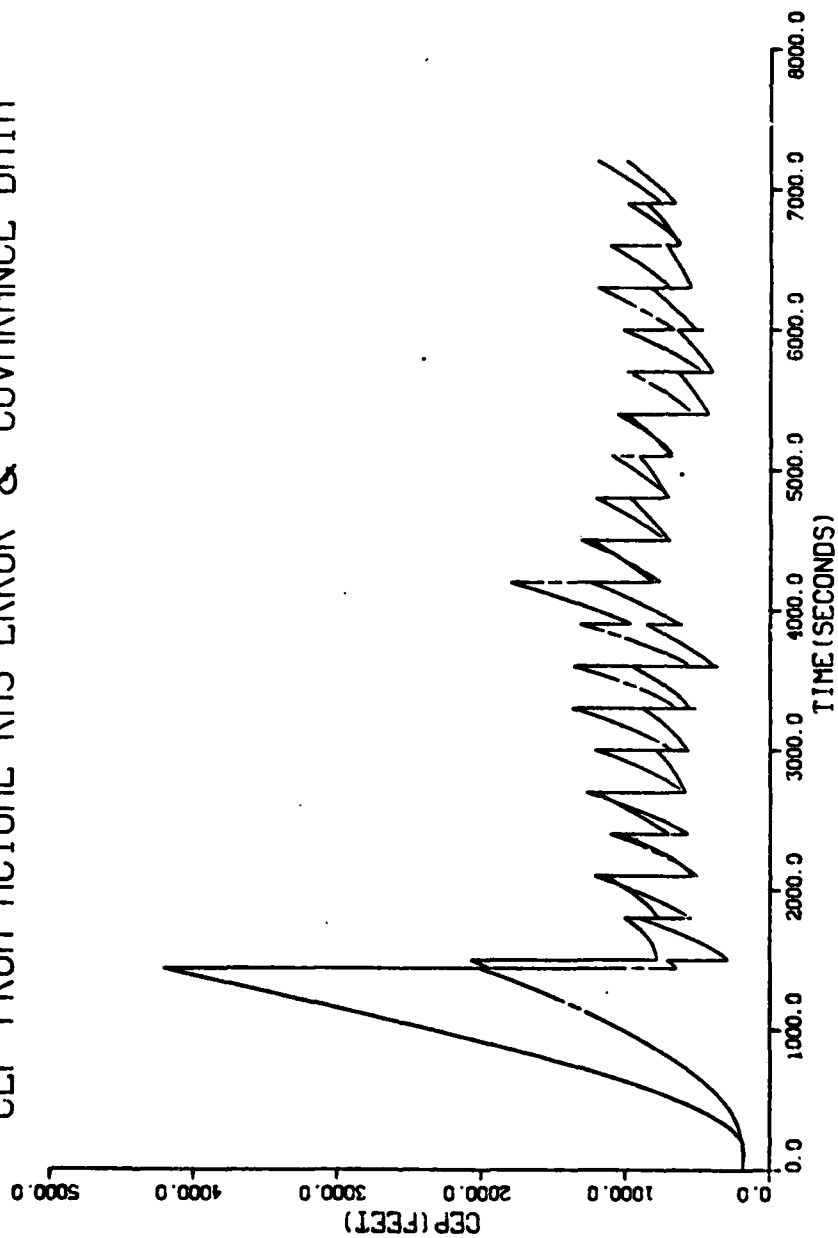
Figure 9.17(a) New Truth and Revised Filter Models - All Errors at Normal Values, Actual CEP (solid line) and Predicted CEP (broken line)

155
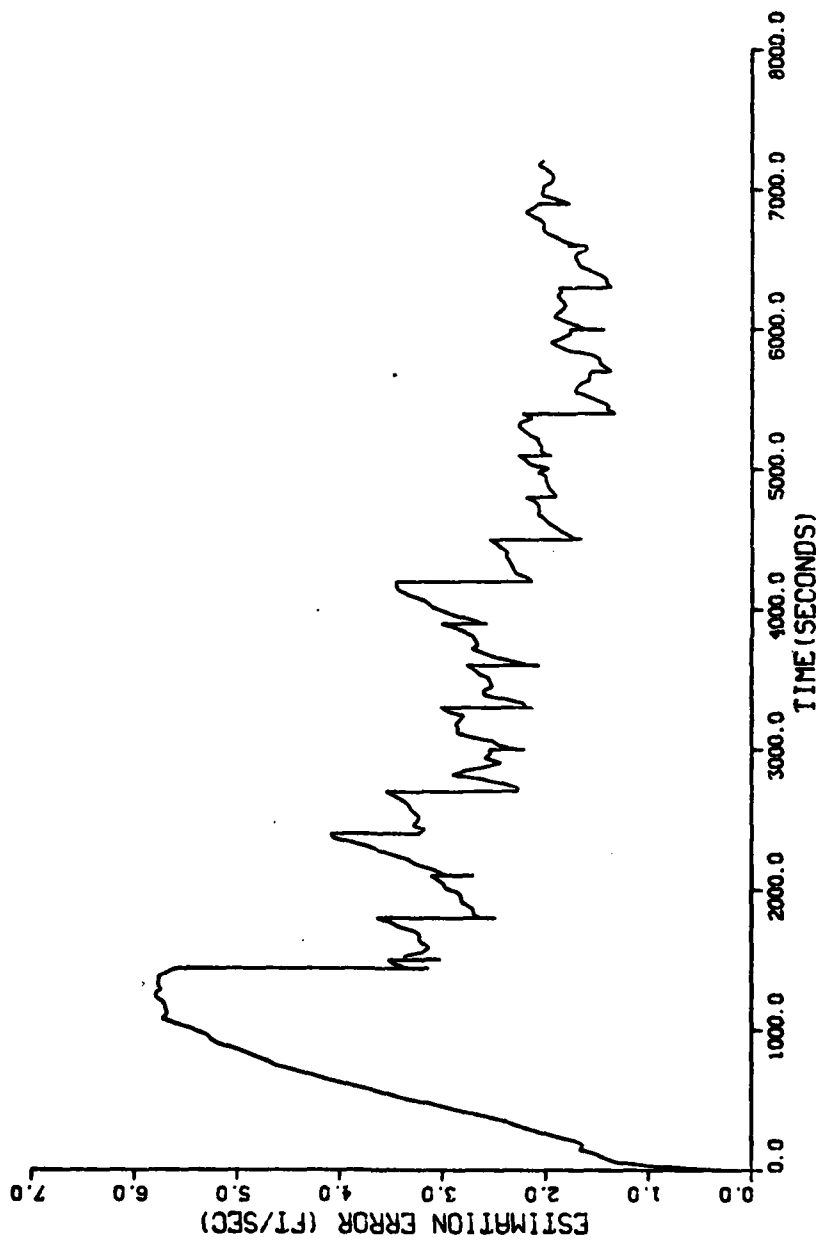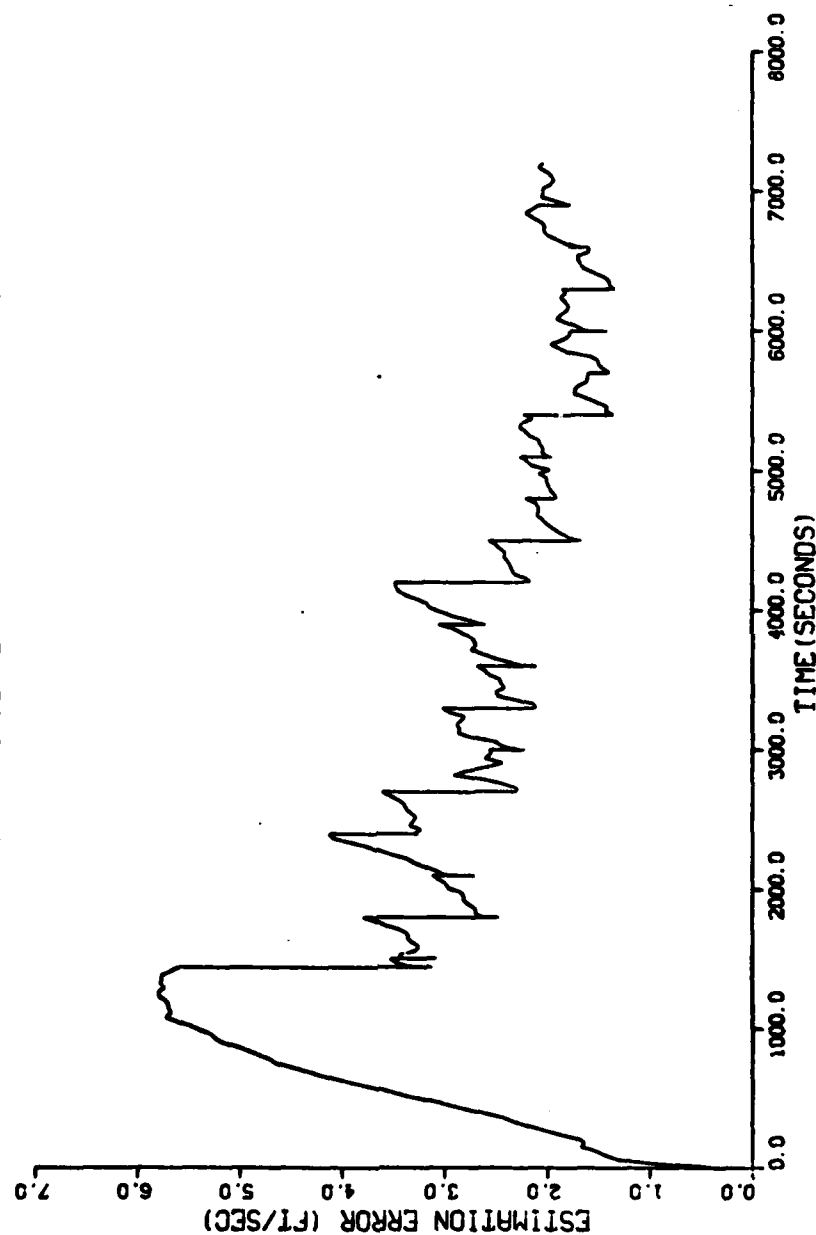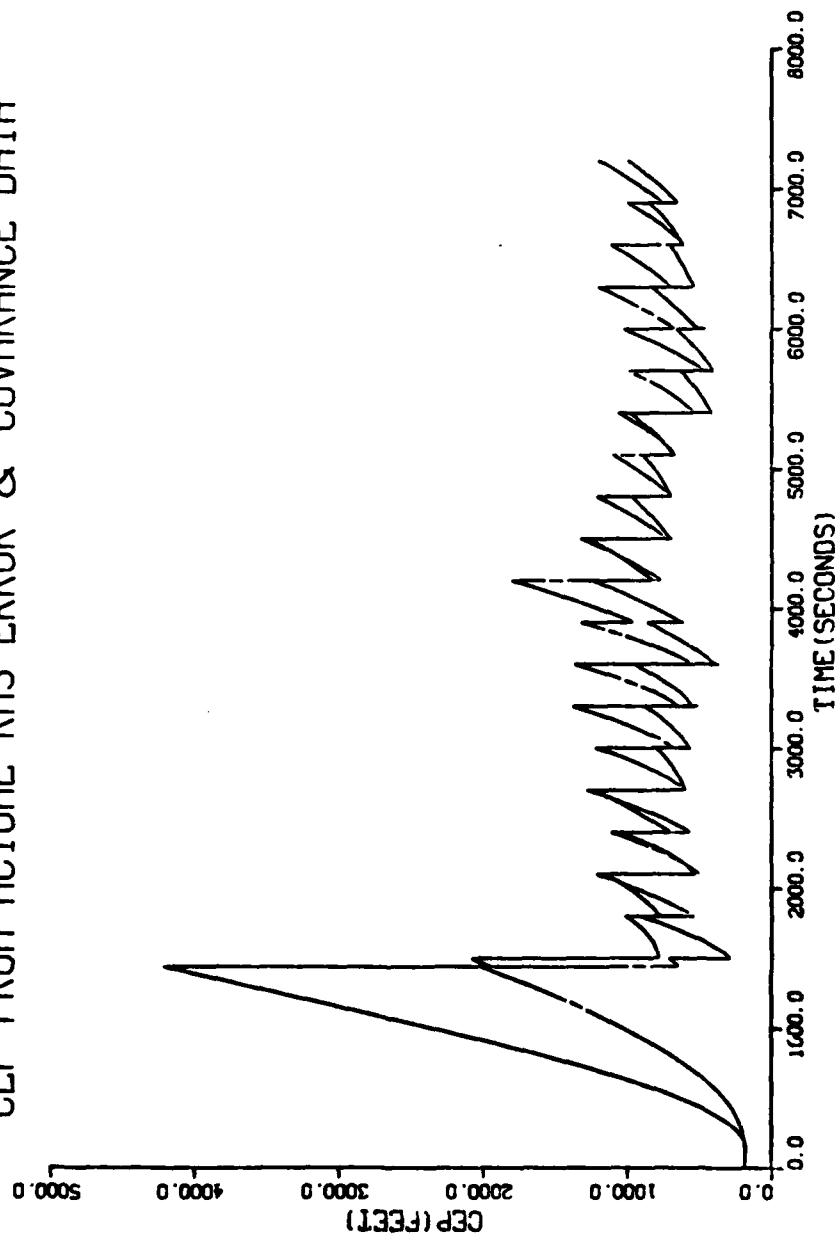
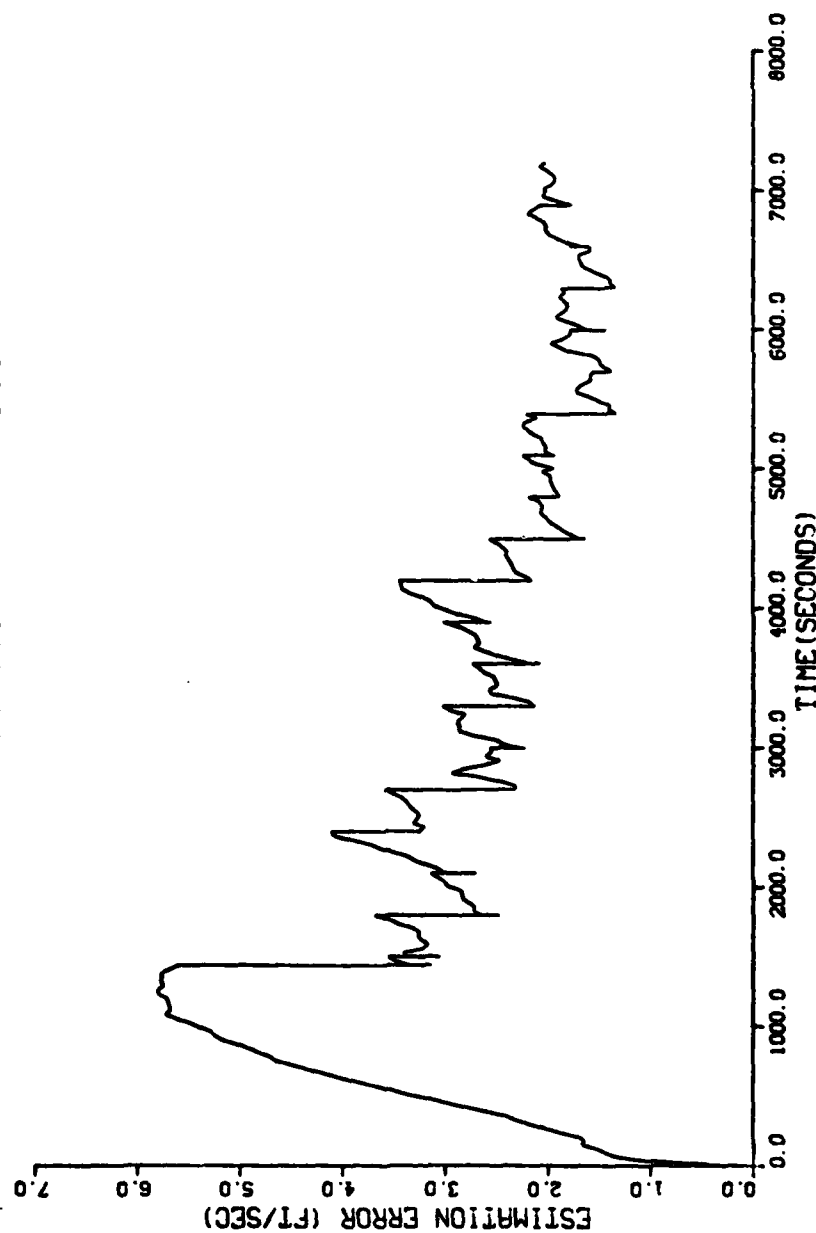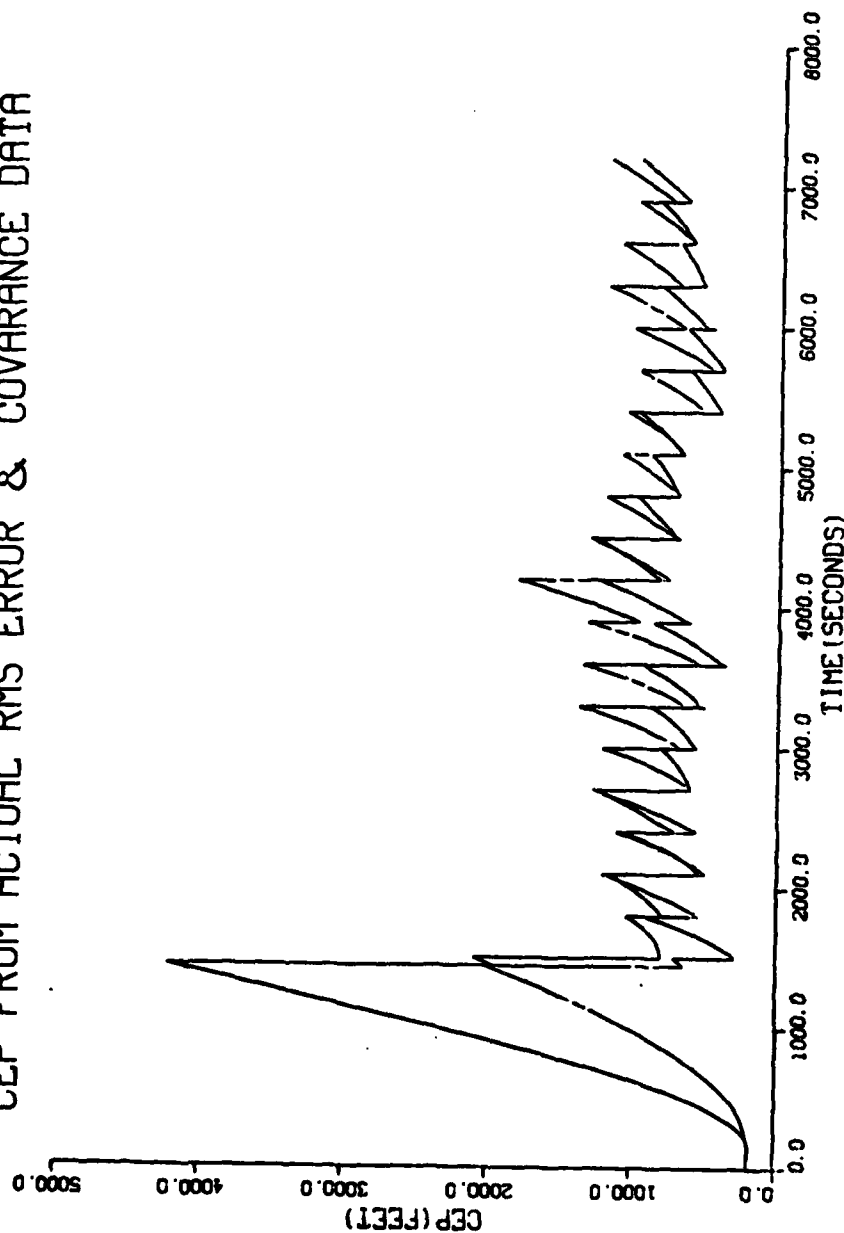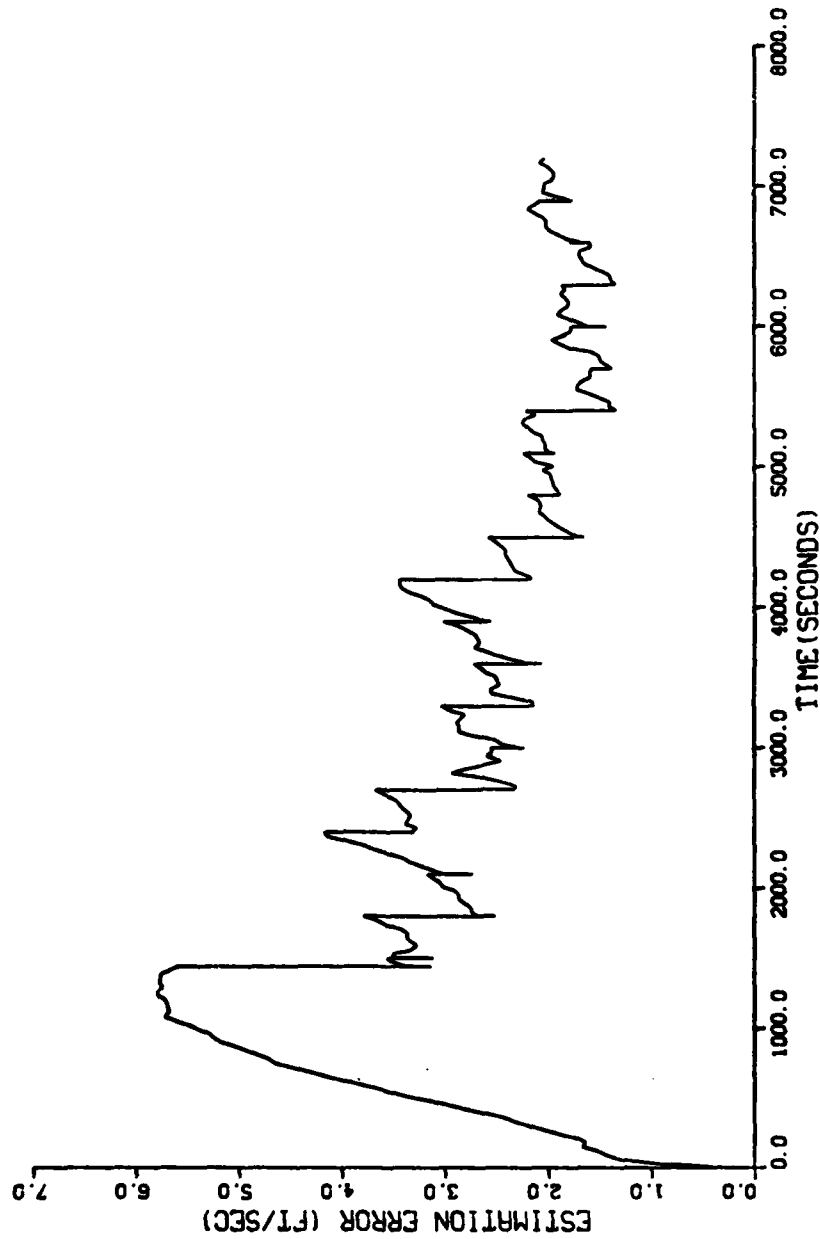Figure 9.17(b) New Truth and Revised Filter Models – All Errors at Normal Values,
RSS of Actual Velocity Errors, One Sigma Value

156
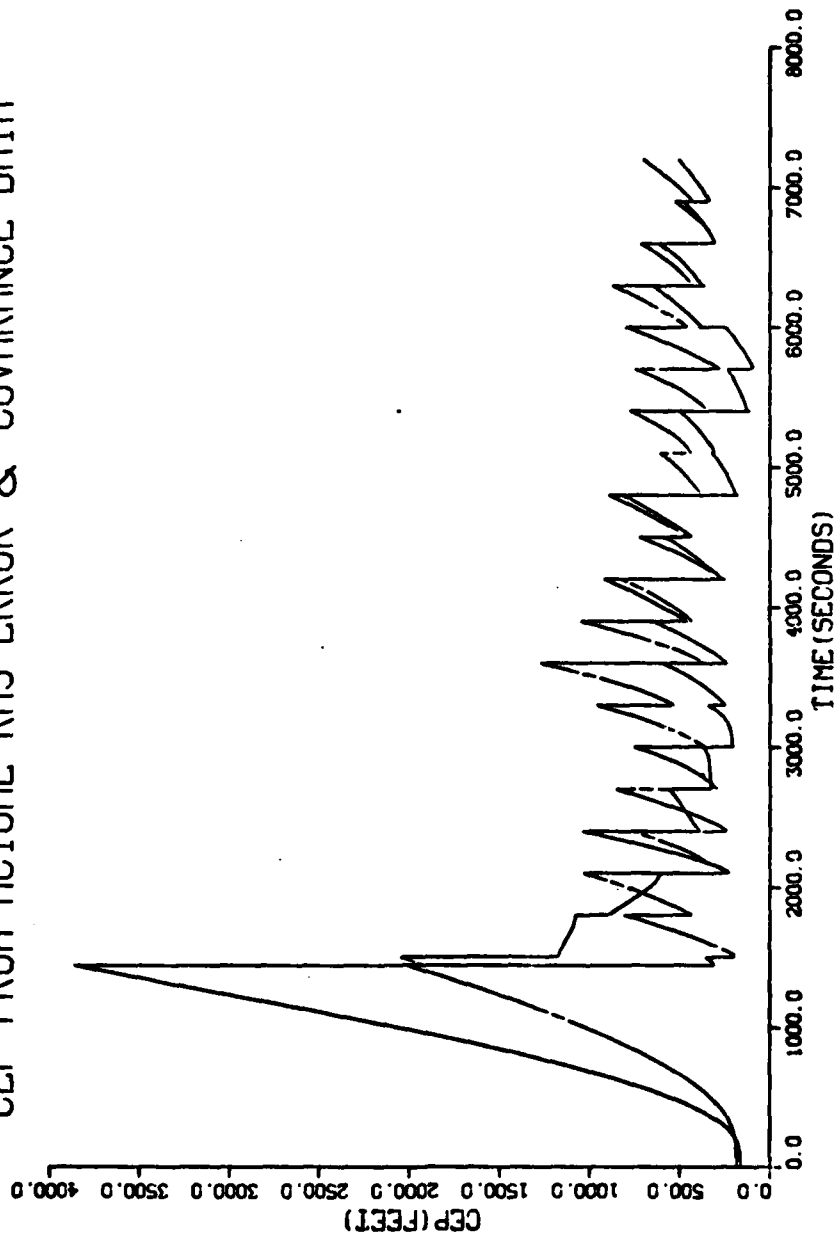
Figure 9.18 New Truth and Revised Filter Models - All Errors Set to Zero, Actual CEP (solid line) Predicted CEP (broken line)
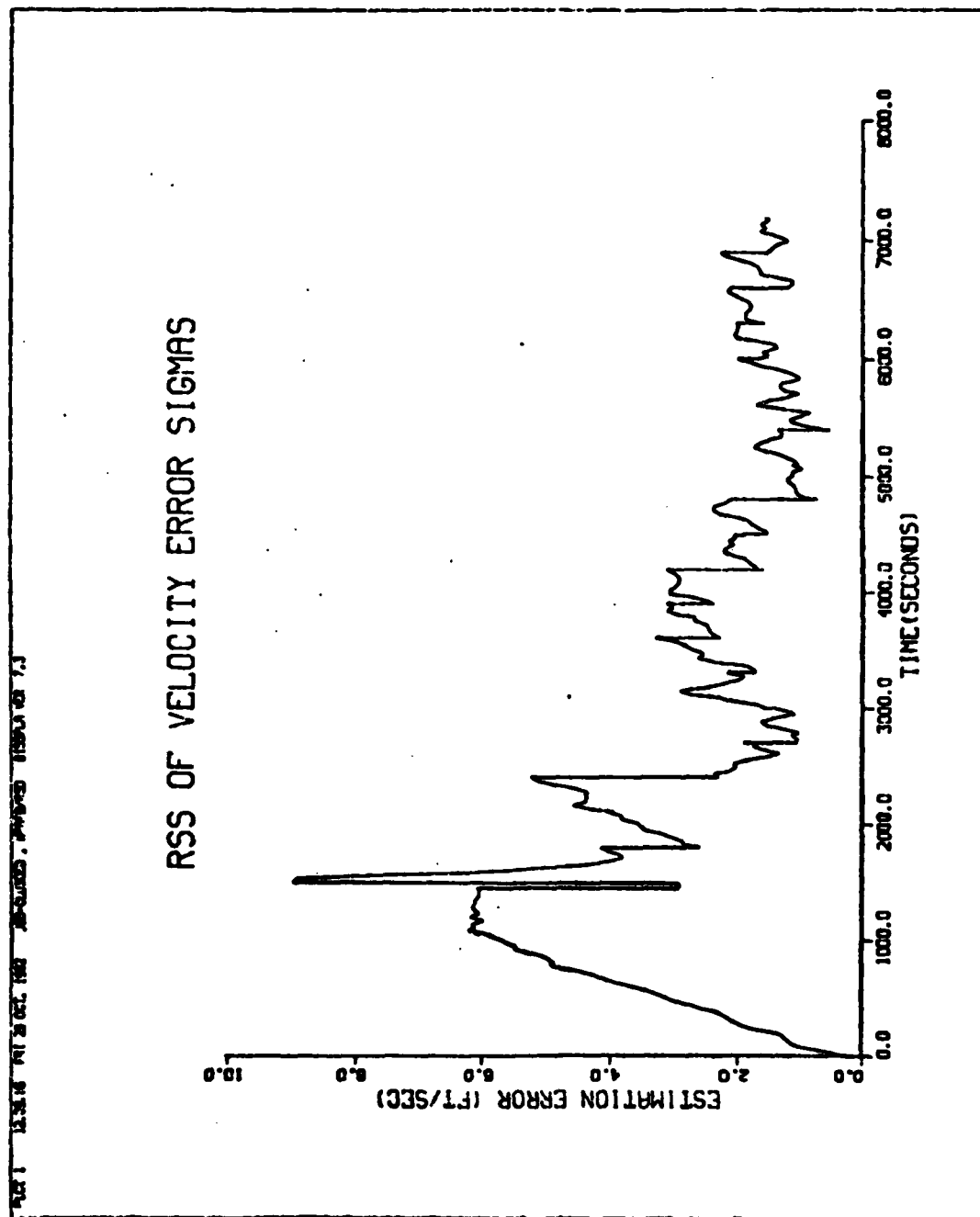
Figure 9.19 New Truth and Revised Filter Models - All Errors Set to Zero, RSS of Actual East, North, and Vertical Velocity Errors, One Sigma Values
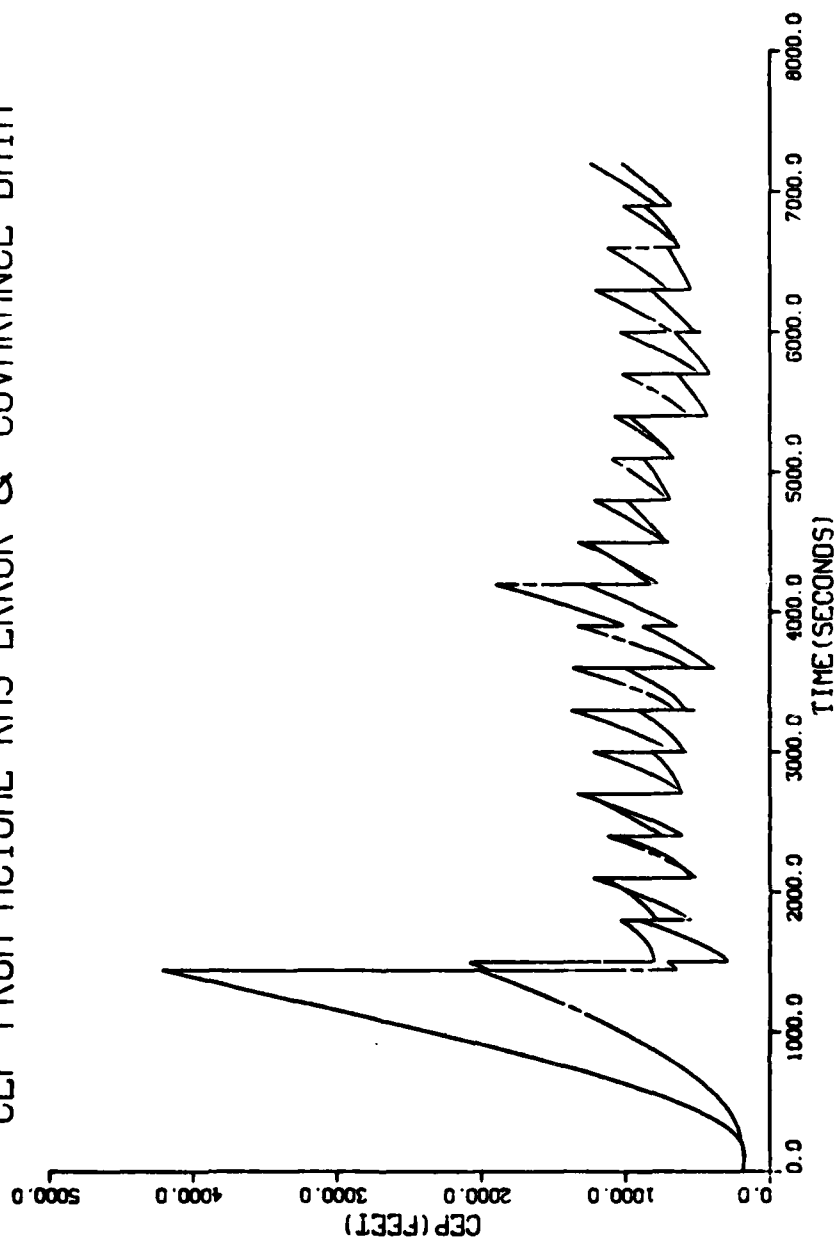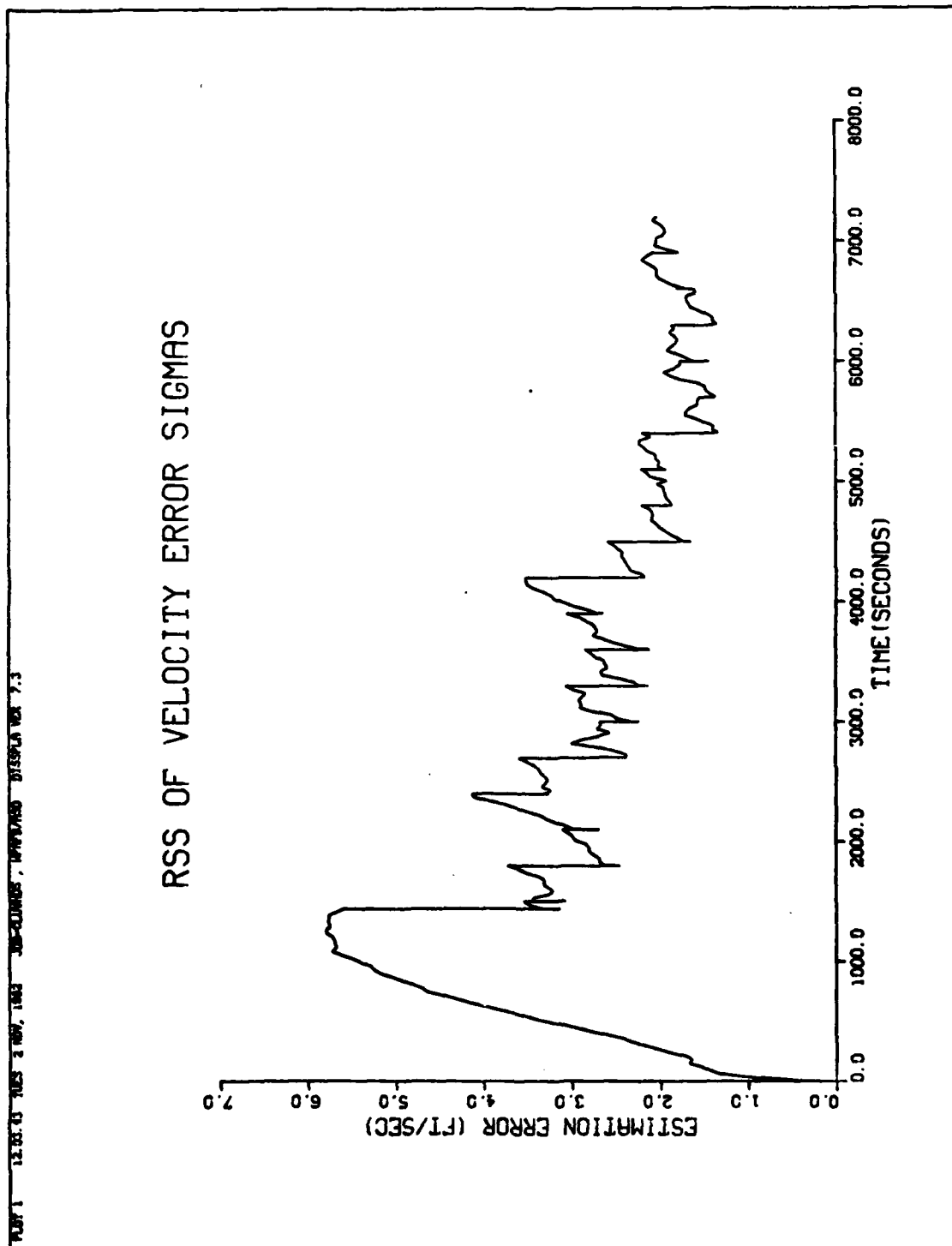
158
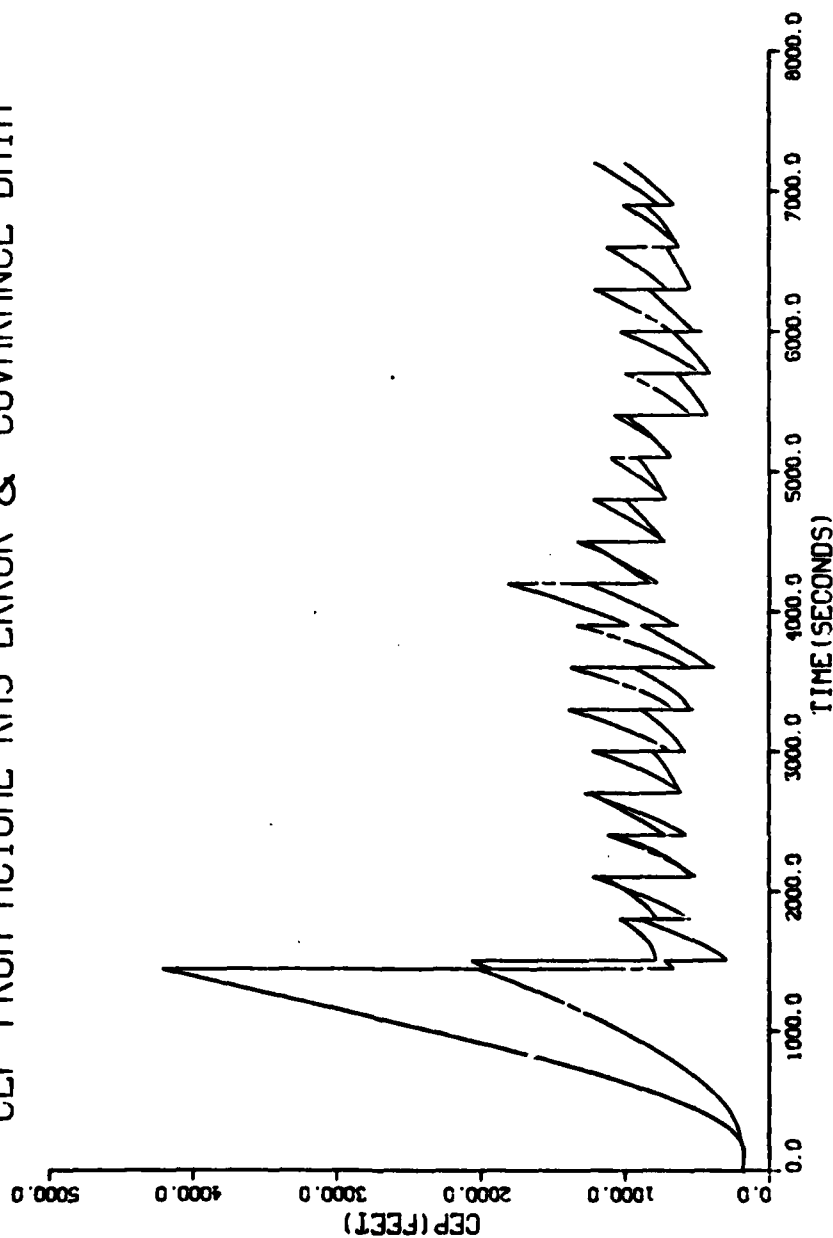
Figure 9.20 New Truth and Revised Filter Models - Helmet Error at 110% of Normal Value, Actual CEP (solid line) and Predicted CEP (broken line)

Figure 9.21 New Truth and Revised Filter Models – Helmet Error at 110% of Normal Value, RSS of Actual Velocity Errors, One Sigma Values

Figure 9.22 New Truth and Revised Filter Models – Human Error at 110% of Normal Value, Actual CEP (solid line) and Predicted CEP (broken line)

Figure 9.23 New Truth and Revised Filter Models - Human Error at 110% of Normal Value, RSS of Actual Velocity Errors, One Sigma Values

Figure 9.24 New Truth and Revised Filter Models - Canopy Refraction Error at 110% of Normal Value, Actual CEP (solid line) and Predicted CEP (broken line)

Figure 9.25   New Truth and Revised Filter Models - Canopy Refraction Error at 110% of Normal Value, RSS of Actual Velocity Errors, One Sigma Values

Figure 9.26 New Truth and Revised Filter Models – Vibration Error at 110% of Normal Value
Actual CEP (solid line) and Predicted CEP (broken line)

Figure 9.27 New Truth and Revised Filter Models – Vibration Error at 110% of Normal Value
RSS of Actual Velocity Errors, One Sigma Values
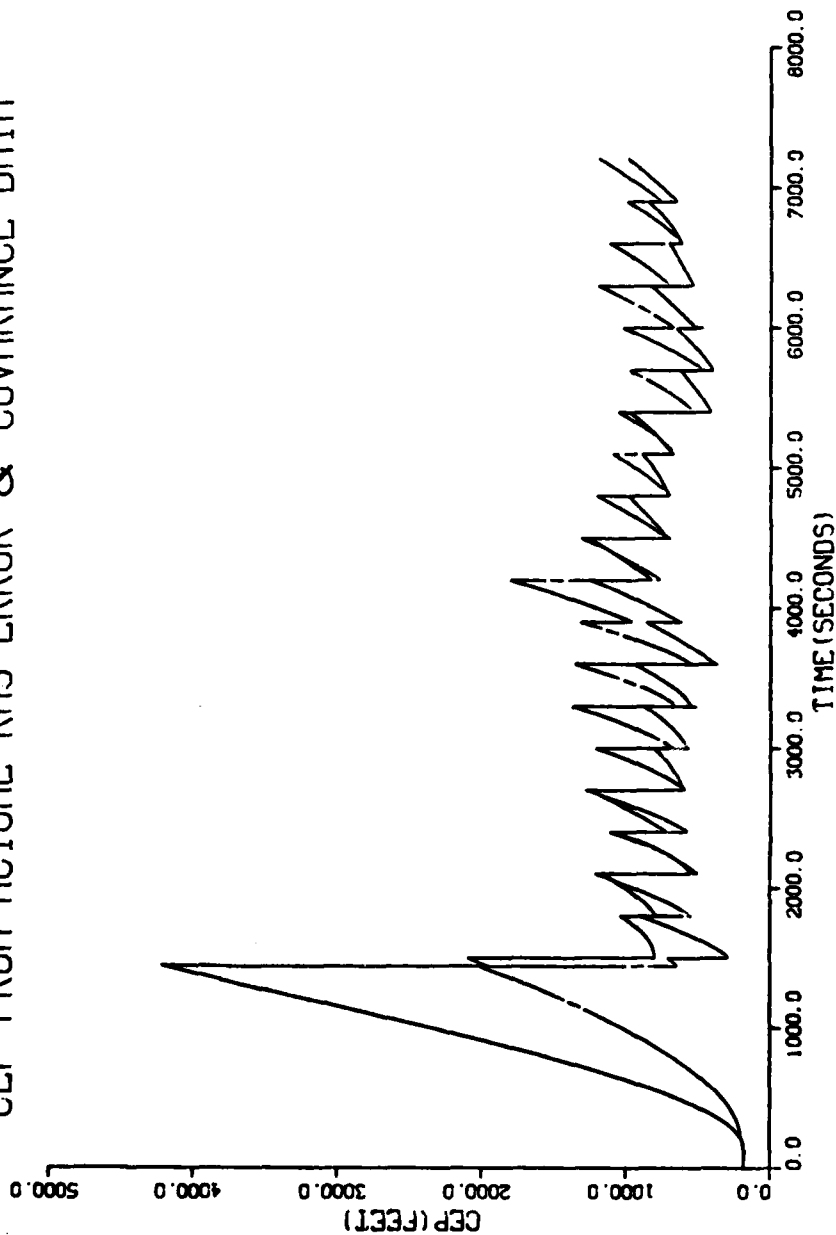
Figure 9.28 New Truth and Revised Filter Models - Boresight Error at
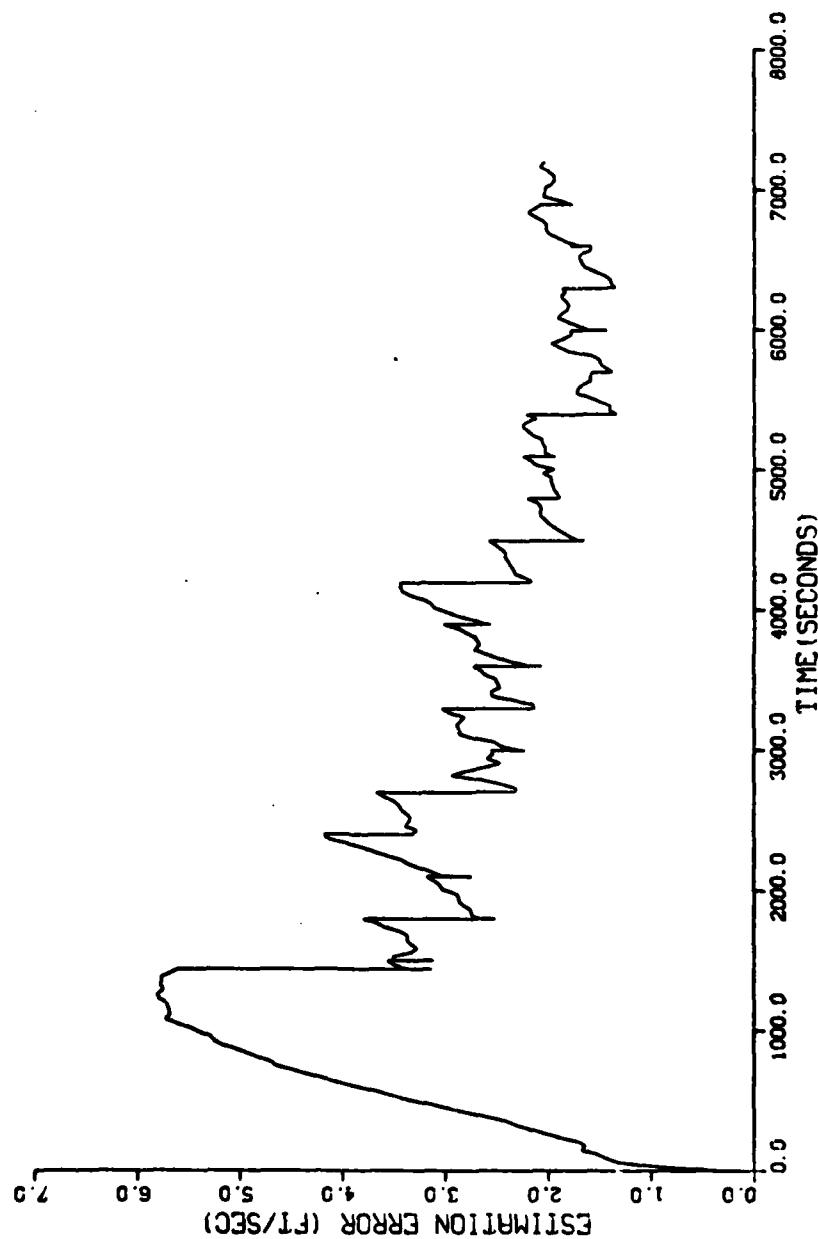110% of Normal Value, CEP of RMS Position Error

Figure 9.29 New Truth and Revised Filter Models - Boresight Error at 110% of Normal Value, RSS of Actual Velocity Errors, One Sigma Values
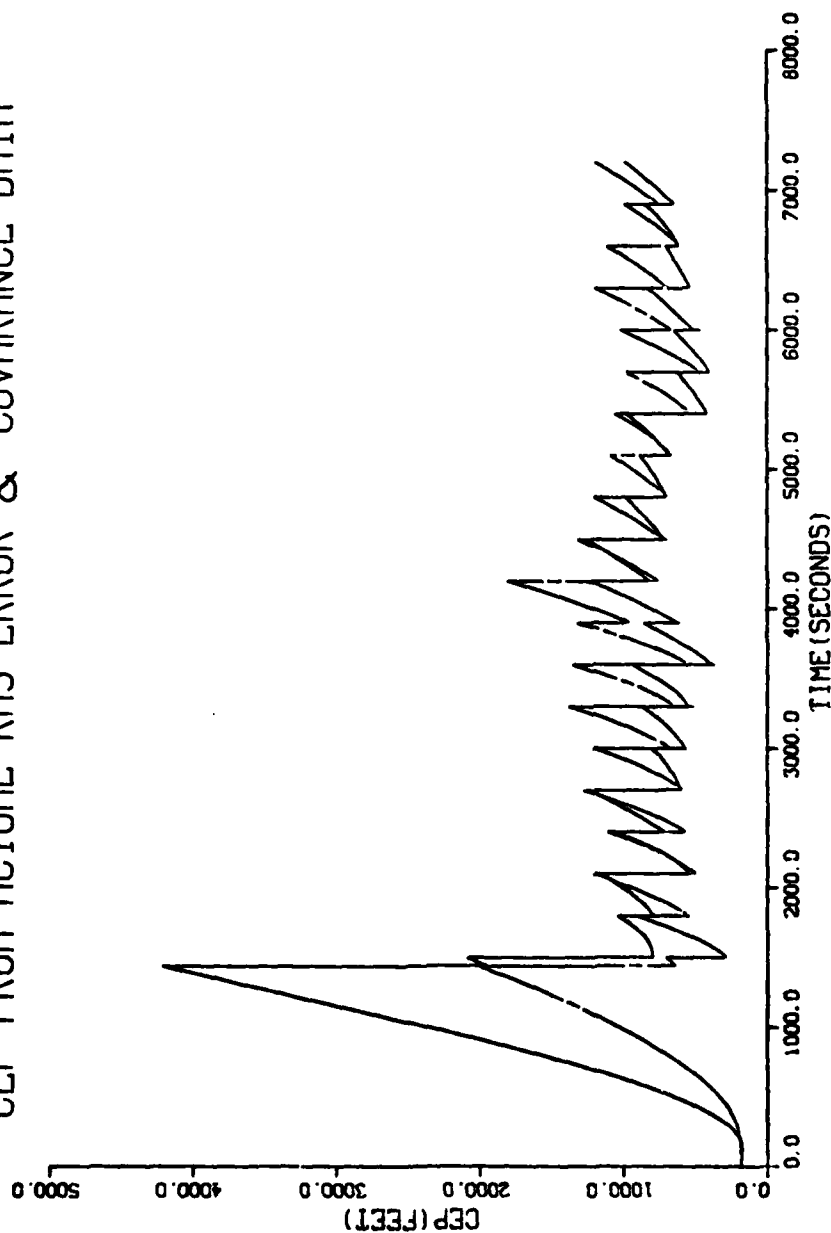
Figure 9.30 New Truth and Revised Filter Models - Additive White Noise at 150% of
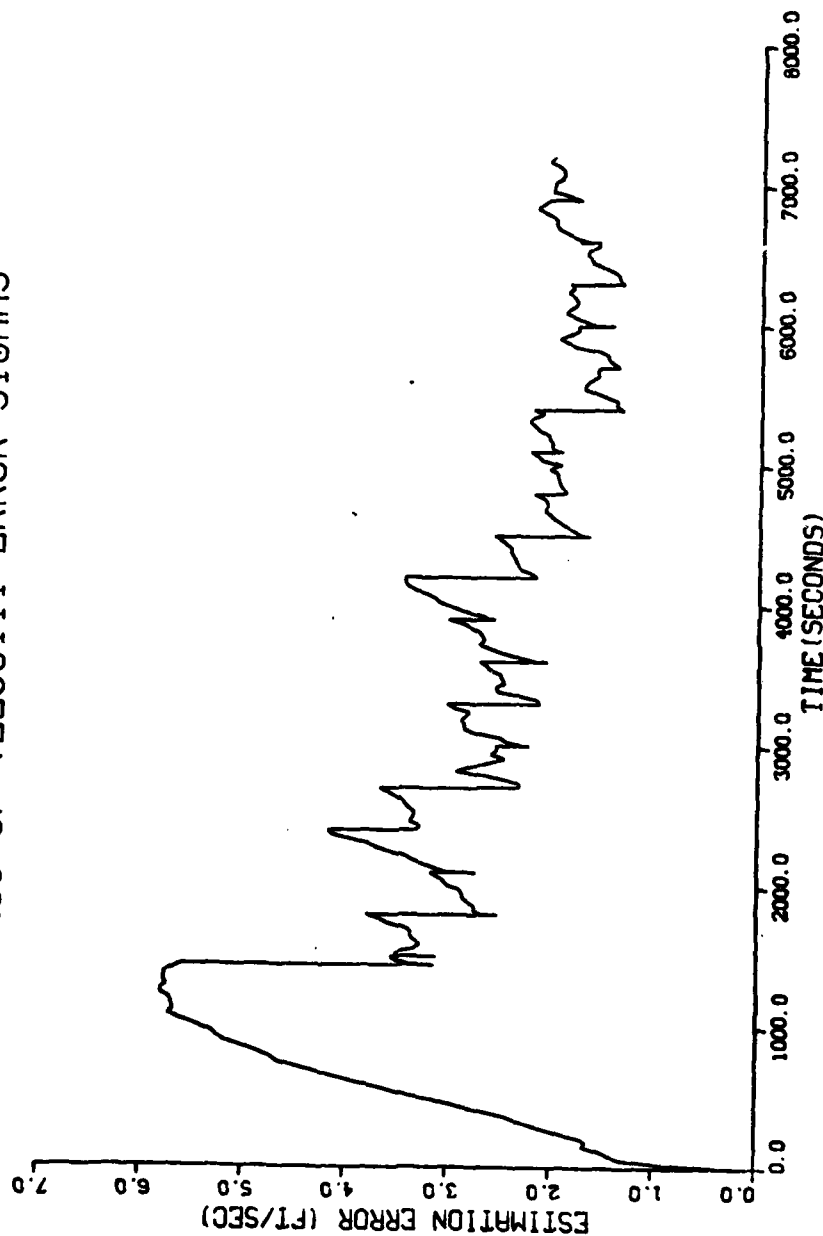Normal Value, Actual CEP (solid line) and Predicted CEP (broken line)

Figure 9.31 New Truth and Revised Filter Models - Additive White Noise at 150% of Normal Value, RSS of Actual Velocity Errors, One Sigma Values

values for the helmet, human, canopy, vibration, boresight, and additive
noise error terms of the HMS error model. A comparison of these plots
with the normalized system of Figures 9.17a and 9.17b show that a 10%
change in the magnitude of these error terms has a very small effect upon
the performance of the filter. Small changes in the position and
velocity plots can be seen by overlaying the respective plots with the
baseline plot. When a difference between the sensitivity plot and the
baseline plot exists it usually occurs in the first 3000 seconds of the
mission. The differences in position and velocity error are point
differences that occurs at the beginning of the mission. Further into
the mission there is no detectable differences between the plots of
Figure 17 and the sensitivity plots. The point differences found were
differences of 100 ft or less in CEP and 0.3 ft/sec or less in velocity.
From these preliminary results it can be concluded that the filter is
relatively insensitive to 10% changes in the magnitudes of the errors.

X   Conclusions and Recommendations

Conclusions

The original intention of this study was to develop the HMS system error model based upon the results of experimental data which have been published in the unclassified literature. This model development effort was successful in identifying three major error contributions. These were the Helmet-Mounted Sight equipment itself, the human operator, and the environment. The HMS equipment errors are the residuals that remain after the cockpit has been mapped and the system compensated for stray magnetic fields. The human operator model reflects how well the human can sight moving targets. The human sighting accuracy is a function of the target angular rate. The environmental error terms include the effect of the aircraft vibrations upon the pilot sighting accuracy and the degradation of accuracy due to the canopy refraction errors. This HMS system model was implemented into the LANA simulation and the effects of the new or more accurate truth model were demonstrated. The existing Kalman filter was retuned to match the new truth model and satisfactory performance of the LANA simulation was restored. The sensitivity analysis did not reveal the filter to be sensitive to 10% changes in the magnitude of the errors.

The canopy refraction error model could not be modeled from the literature. The lack of information in the literature required that an experiment be conducted to measure representative angular deviation or refraction data. The latest version of the canopy angular deviation measurement equipment was made available by AMRL and was used to measure the refraction of a typical F-16 canopy. It was also fortunate that the

172

AMRL is heavily involved with the design and testing of advanced versions of the HMS hardware and electronics. The information provided by the AMRL engineers was essential in developing accurate HMS equipment models and human operator models.

It should be noted that some of the elements in the HMS error model were specifically designed to suit the LANA mission. For example, the human operator model was designed around the "sight and pickle" aiming mode. This model may not be ideally suited to other studies that employ the pure pursuit tracking mode. Also the canopy refraction and vibration models were necessarily modeled after a particular aircraft. Although every effort has been made to generalize these models, any future user should determine if the aircraft under study is well represented by these models.

The results of the performance and sensitivity analysis were intended to show the effect of the new truth model upon the performance of an existing filter within a given simulation. The results of the performance study shows that the original truth and filter models were better than they were believed to be prior to the completion of the analysis. The original filter was expected to become degraded markedly when an accurate HMS truth model was used in the simulation program. This prediction did not occur; the position and velocity errors became much larger, but the filter remained convergent and after retuning yielded performance comparable to the original estimates. This result is supported by the error budget for the six HMS error terms under study. Although individually some of the terms are large error sources, the RSS values of the azimuth and elevation components of the system aiming error are less than three times the values used in the original filter. Thus,

173

with a small amount of filter tuning, the revised filter was able to produce results equivalent to those seen with the old filter and truth model.

The error sensitivity analysis indicated that the filter is able to accommodate small perturbations in the magnitudes of all of the six error terms. To develop full confidence that the filter is not sensitive to changes in one or more of the error terms, a more extensive analysis would be required.

The Helmet-Mounted Sight system error model developed in this study includes all of the significant error sources which are known to influence the HMS aiming accuracy. These error sources include the sight equipment, the human operator, and the operational environment. The equipment errors considered were the inherent accuracy of the HMS equipment and how accurately this equipment could be aligned or calibrated. The human error terms examined were the basic human head aiming abilities for both the static and moving target cases. The effect of whole body vibration, that is transmitted to the head, upon the human aiming accuracy was also included in the error model. Last, the aiming error that is induced by the canopy refraction was measured and incorporated into the error model. The performance and sensitivity analysis sections of this report illustrate the need for an accurate model of the HMS errors and the improvement in inertial navigation performance achieved by using the HMS position updates.

Recommendations

To make this HMS error model more generally useful to future studies, information to complete the vibration and HMS equipment errors

is required. The vibration model is based upon the power spectral density data of the helmet tracking error. The shape of the PSD curves over the given frequency range is believed to be generally the same for most other aircraft types. However, given any aircraft type, it is not always known how much to shift the curves up or down the ordinate axis to model the magnitude of the vibrations for that particular aircraft. In the HMS model described in this report the PSD's for the F-4 aircraft were approximated from the Canberra aircraft PSD data. For this vibration model to be widely applicable the conversion factors to the F-16, F-15, F-18, and other potential LANA aircraft, are required. The information about the HMS hardware residuals was not available. To complete this model the nature of the correlation between the errors is needed to supplement the error magnitude data given in this report.

The time limits on this study precluded verifying the accuracy of the error budget given in Chapter VIII. A suggested method of validating these numbers would be to conduct a series of Monte Carlo studies in which the error terms of the HMS truth model are "turned on" individually to determine the separate effects of these sources (Ref 29:339). The plots of each individual error source could be compared with the zero error plots of Figures 9.18 and 9.19 to determine the actual magnitude of that error. By repeating this process for each of the six error terms the relative magnitudes of each error can be found and compared with the error budget.

Bibliography

1. Musick, S.H. <u>Landmark Observation Equations for Kalman Filter Updates in LANA</u>, Technical Memorandum, AFWAL-TM-81-16, Wright-Patterson AFB, Ohio, May 1981.

2. Furness, T.A. and J.A. Joseph. "Visually Coupled Systems", <u>Air University Review</u>, Mar-Apr 1974.

3. Musick, S.H. <u>SOFE: A Generalize Digital Simulation for Optimal Filter Evaluation - Users Manual</u>, Technical Report, AFWAL-TR-80-1108, Avionics Laboratory, Wright-Patterson AFB, Ohio, Oct 1980.

4. Musick, S.H. <u>PROFGEN - A Computer Program for Generating Flight Profiles</u>, Technical Report, AFWAL-TR-76-247, Avionics Laboratory, Wright-Patterson AFB, Ohio, Nov 1976.

5. Widnall, W.S. and P.A. Grundy. <u>Inertial Navigation Error Models</u>, AFSWC-TR-73-26, May 1973.

6. Furness, T.A. "Discussions between Dr. Furness and Capt. Clubine, Ref: Human HMS aiming modes", AMRL, Wright-Patterson AFB, Ohio, 22 June 1982.

7. Burington, R.S. and D.C. May. <u>Handbook of Probability and Statistics with Tables</u>, McGraw-Hill Book Co., New York, 1965.

8. Siouris, G.M. Class Report, EE-7.35, Air Force Institute of Technology, 1982.

9. Papoulis, A. <u>Probability, Random Variables & Stochastic Processes</u>, McGraw Hill Book Co., New York, 1965.

10. Hughes, R.J. and Henke, A.H. <u>Helmet-Mounted Sight/Display Applications</u>, AFFDL-TR-69-118, Vol III, Apr 1970.

11. Nicholson, R.M. "The Feasibility of a HMS as a Control Device", <u>Human Factors</u>, Vol 8, Oct 1966.

12. Verona, R.W. <u>Head Aiming/Tracking Accuracy in a Helicoptor Environment</u>, USAARL Report No. 79-9, May 1979.

13. Reichwein, Carl. <u>Effects of G and Target Position on Static MMS Sighting</u>, NADC-MR-7023, Dec 1970.

14. Kocian, Dean. "Discussions with Mr. Kocian, Ref; HMS Hardware Accuracy", AMRL, 12 Aug 1982.

15. Grossman, J.D. Flight Evaluation of Pilot Sighting Accuracy Using a Helmet-Mounted Sight, Technical Publication 5638, Naval Weapons Center, April 1974.

16. Monk, D.L. and J.L. Porterfield. Head Tracking at Large Angles from the Straight Ahead Position, TR, AMRL-TR-78-27, Aerospace Medical Research Laboratory, Wright-Patterson AFB, Ohio, April 1978.

17. Monk, D.L. "Discussions with Mr. Monk, Re: Human Head Tracking Abilities", Aerospace Medical Research Laboratory, Ohio, 16 Jun 82.

18. Harris, J.S. Study and Evaluation of Existing Techniques for Measuring Aircraft Windscreen Optical Quality: Development of New Techniques for Measuring Aircraft Windscreen Optical Distortion, Technical Report, AFMARL-TR-81-25, June 1981.

19. Genco, L.V. and H.L. Task. Aircraft Transparency Optical Quality: New Methods of Measurement, Technical Report, AFAMRL-TR-81-21, WPAFB, Onio, June 1981.

20. Genco, L.V. The Measurement of Angular Deviation and Its Relation to Weapons Sighting Accuracy in F-16 Canopies, Draft Technical Report, AFAMRL, WPAFB, Ohio, June 1982.

21. Furness, T.A. The Effects of Whole Body Vibration on the Perception of the Helmet-Mounted Display, Doctoral Dissertation, Univ of Southhampton, Faculty of Engineering and Applied Science, England, June 1982.

22. Speakman, J.D. Crew Station Vibration Environments During Low-Altitude High Speed Flight, Proceeding of the Air Force Systems Command 1971 Science and Engineering Symposium, Dayton, OH, Oct 1971

23. Von Gierke, H.E. and N.P. Clark. "Effects of Vibration and Buffet on Man", Aviation Medicine, Chapter 10, pp 188-223, 1971.

24. Guignard, J.P. "Vibration", A Textbook of Aviation Physiology, J.A. Gilles Ed. Chapter 29, pp 813-894, 1971.

25. Jarrett, D.M. Helmet Slip during Simulated Low-Altitude, High-Speed Flight, Technical Report 78018, Farnborough, England, Feb 1978.

26. Pradko, F. and T.R. Orr, Human Vibration Analysis, Society of Automotive Engineers, Mid-Year Meeting, Chicago, IL, 17-21 May 65.

27. Griffen, M.J. and C.H. Lewis. "A Review of the Effects of Vibration on Visual Acuity and Continuous Manual Control", Journal of Sound and Vibration 56(3), pp 383-413, Oct 1978.

28. Tatham, N.O. An Investigation of Head Aiming During Simulated Aircraft Vibration Conditions, Technical Memo FS 74, Royal Aircraft Establishment, Farnborough, England, 1976.

29. Maybeck, P.S. Stochastic Models, Estimation, and Control Vol 1, Mathematics in Science and Engineering, Vol 141, Academic Press, New York, 1976.

30. Birt, J.A. and H.L. Task. Proceedings of a Symposium on Visually Coupled Systems, Development and Application, Technical Report, AMD-TR-73-1, Sep 1973.

31. Cox, T. Advanced Visual Target Acqusition System, Brochure, Polhemus Navigation Sciences, Essex Junction, Vermont, Nov 1977.

32. SHMS IIIA, Operation and Maintenance Manual for the SPASYN Helmet-Mounted Sight, OMM-80-10244, Nov 1980.

33. Hager, Doug. "Discussions with Mr. Hager Re: SPASYN HMS Compensations", Avionics Laboratory, WPAFB, 8 Sep 82.

34. Clubine, W.R. and S.H. Musick, LANA Helmet-Mounted Sight Error Model, Technical Memo   AFWAL-TM-82-16, Avionics Laboratory, WPAFB, OH, Dec 1982.

35. Musick, S.H. LANA Program Listing, Avionics Laboratory, AAAN, Wright-Patterson AFB, Ohio, Sep 82. (unpublished)

36. IMSL Library, International Mathematical and Statistical Libraries Inc., IMSL LIB03-0006VI, Sixth Edition, Houston, TX, 1977.

37. HP-41 CV STAT PAC, 00041-90030 Rev B 1/80, Polynomial Regression. Hewlett-Packard, Coruallis, Oregon, Jan 1980.

38. McRuer, D.T., et. al. Human pilot Dynamics in Compensatory Systems: Theory, Models, and Experiments with Controlled Element and Forcing Function Variations, AFFDL-TR-65-15, July 1965, Air Force Flight Dynamics Laboratory.

39. Sheridan, T.B. and Ferrell, W.R. Man-Machine Systems: Information, Control and Decision Models of Human Performance The MIT Press, Cambridge, MA, 1974.

40. Gelb, Arthur. Applied Optimal Estimation, The Analytic Sciences Corporation, The MIT Press, Cambridge, MA, Feb 1975.

APPENDIX   The SPASYN Helmet Mounted Sight (SHMS)

The SPASYN (Space Synchro) Helmet-Mounted Sight is designed and
manufactured by Polhemus Navigation Sciences, Inc. (PNSI) in Essex
Junction, Vermont. The SHMS system measures the pilot's line-of-sight to
a target with respect to aircraft coordinates, and processes that
information for use in direct control of weapon delivery systems and
remote sensors. The heart of the system is the helmet-mounted
electromagnetic device which senses the head position and attitude
relative to the selected reference frame. The system determines the
line-of-sight by measuring the angular/spatial relationship between a
radiator fixed to the aircraft and the sensor mounted on the observer's
helmet (Ref. 31:4).

System Components. The SPASYN concept is a closed-loop transducing
and computing scheme which provides a precise and continuous measure of
the relative position and orientation between two coordinate frames. The
SHMS system is comprised of three function components: a three-axis
electromagnetic radiator, a three-axis electromagnetic sensor, and a
system electronics unit.

The Radiator Assembly is permanently mounted in either the cockpit
or on the inside surface of the canopy. The radiating device is a
ferrite core structure around which an orthogonal array of coils is
wound. This core and coil assembly is excited by the System Electronics
Unit (SEU) to produce the controlled nutating magnetic field by which the
closed-loop system tracks the sensor located on the pilot's helmet (Ref
31:401).

The Sensor Unit is located under the pilot's helmet visor protector.

179

It includes a sensing device which is smaller than, but otherwise similiar to, the radiating device. The sensor weighs approximately six-tenths of an ounce, and is connected to the SEU by a pig-tail which weighs one-half ounce. The sensor unit is oriented precisely with respect to the observers headgear, which includes the necessary optical sight or reticle used by the observer to establish his line-of-sight. The sensor and reticle are both fixed to the helmet and boresighted (Ref 30:401).

The System Electronics Unit (SEU) is a single unit containing the power conditioning, analog signal conditioning, and interface electronics required to continuously determine the pilot's line-of-sight angles (azimuth, elevation, and roll) relative to the aircraft reference frame (Ref 31:3).

System Operating Principles. The SHMS sytem is an all-attitude, six degree-of-freedom, position and orientation measurement device. More precisely, it measures the two angles ($\propto$,β) that define the direction to the sensor from the radiator, and the three angles (ψ,θ,ϕ) that define the relative orientation of the sensor to the radiator. The azimuth and elevation angles used in LANA can readily be defined from these five angles. The SHMS is a full six degree-of-freedom measurement system, that is, a system that provides range (R) determination (distance between sensor and radiator) as well as the five angular measurements (Ref 30:402).

The radiator coordinate frame, designated XYZ, represents and defines the SHMS reference frame. It is oriented to align with the aircraft body coordinate frame. The angular degrees-of-freedom, which correspond to the five measured angles, the range, and the geometry

180

relating to the various coordinate frames is illustrated in Figure A.1. This system uses an inverted "right-hand" coordinate frame. The X axis is positive forward (toward the nose of the aircraft). The Y axis is positive along the right wing of the aircraft, and the Z axis extends in the direction of the x cross y vector. The radiator coordinate frame X,Y,Z is defined by the axes of the radiator. The sensor position is specified in rectangular (X,Y,Z), or spherical (α,β,R), coordinates defined relative to the radiator coordinate frame (Ref 12:402).

The radiator coordinate frame is defined during installation and not during boresighting. The mapping of the system aligns the system angles α , β, ϕ, θ, and ψ to the aircraft reference frame. Boresighting, on the other hand, mathematically aligns the sensor to the operators line-of-sight.

Basically, the system tracks the position and orientation of the sensor by determining small changes in the coordinates and then updating the previous measurements. These computations are accomplsihed with linear rotation transformations that yield quantities linearly proportional to these small changes. This information is transformed to the desired coordinate frame and used to update the previous measurements. Figure A.2 illustrates the PNSI SPASYN concept (Ref 32:4-4).

Radiator-Sensor Coupling. The radiator and sensor units of the SHMS system each consist essentially of three identical orthogonal windings on some core structure with radiating and sensing properties which are isotropic. The excitation of three radiator coils and the resultant sensor output are represented as vectors. The excitation produces the equivalent of a single axis source dipole of arbitrary direction as shown
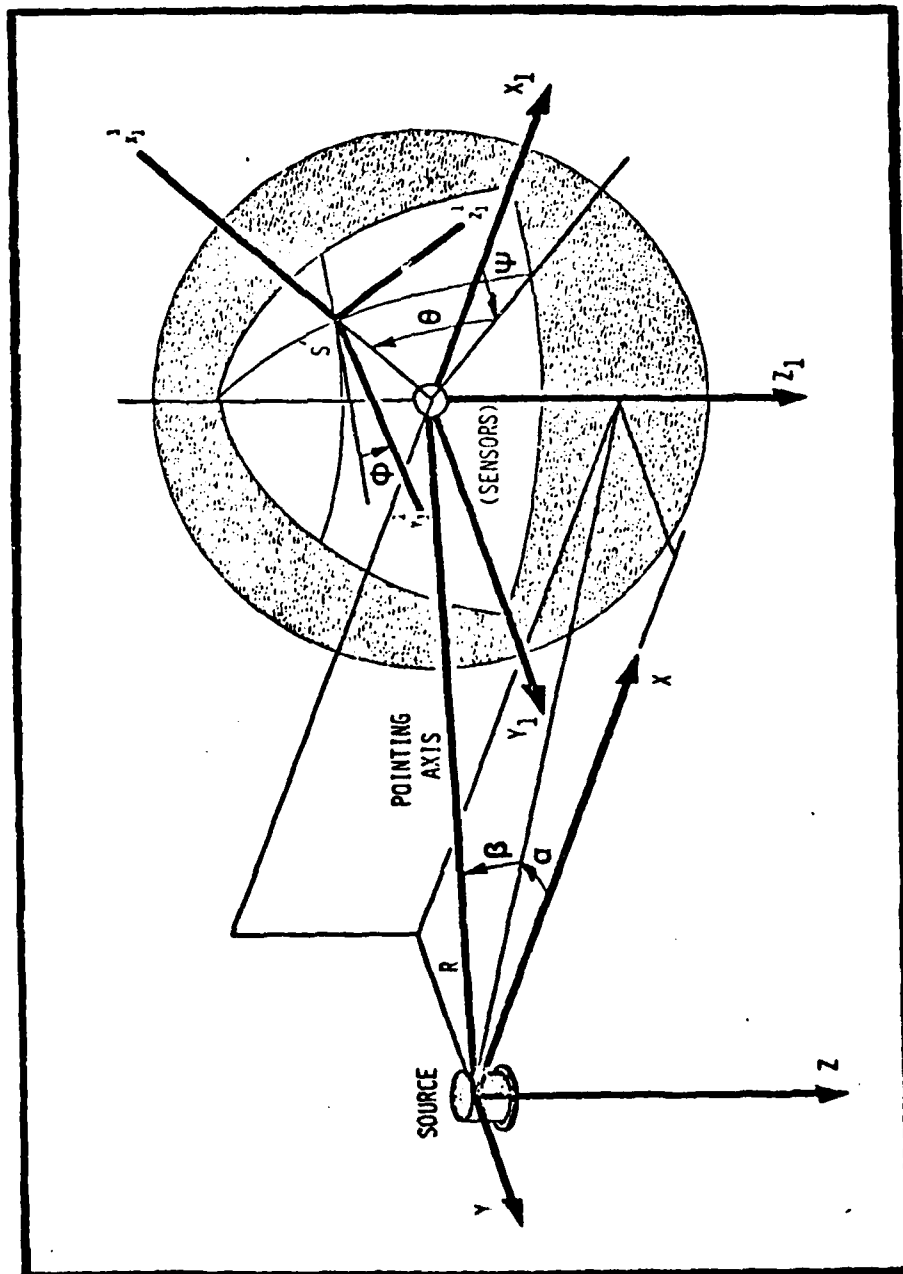
181

Figure A.1 Position and Orientation Coordinate

MICROCOPY RESOLUTION TEST CHART

NATIONAL BUREAU OF STANDARDS-1963-A

A CLOSED-LOOP TRANSDUCING/COMPUTING SCHEME USING A VECTOR
FIELD COUPLING BETWEEN AIRFRAME & HELMET MOUNTED SIGHT
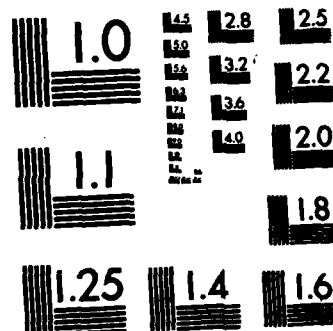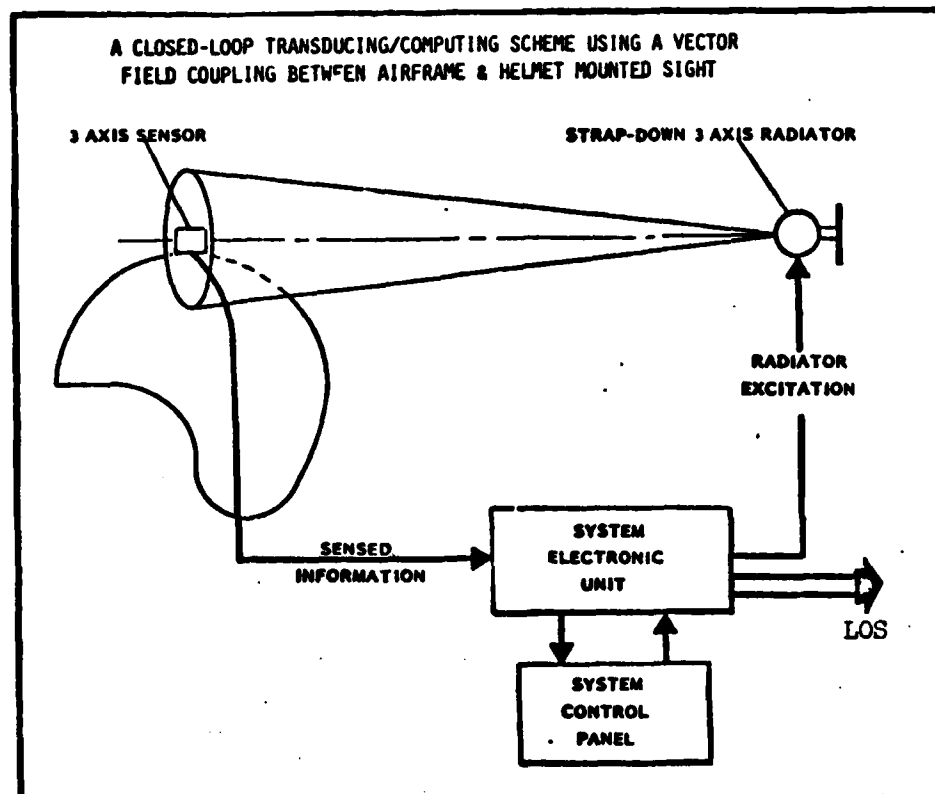
Figure A.2   Space Synchro Helmet-Mounted
             Sight Concept (Ref 30:16)

in Figure A.3. The excitation of the radiator and the resultant currents generated in the coils of the sensor by the magnetic dipole field creates a coupling effect between the radiator and sensor as shown in Figure A.4. Note that each radiator axis is coupled only to the corresponding sensor axis. The single axis dipole of Figure A.3 is the nutation axis of the nutation field created by the excitation of the radiator. This vector is precisely and continuously defined in the reference coordinate frame, centered in the radiator, by the currents generated in the senosr coils. The signals from the sensor are used to compute the angles α and β which completely define the direction of this "tracking line' or pointing axis to the sensor (Ref 30:408 and Ref 31:15).

Determination of Position and Orientation. The position and orientation of the helmet are determined continuously by solving for the six unknowns shown in Figure A.1, i.e. R, α, β, ψ, ϕ, and ψ . This solution requires at least six independent measurements. SHMS generates three pointing vectors at the radiator and makes nine measurements of these vectors at the sensor, thus supplying the systems electronics processor with enough information to solve for the six unknowns. In general, any six of the nine measurements can be used to generate the solution. The radiator-to-sensor coupling equations (Ref 30) contain multiple trigometric products and sums. These nonlinear coupling equations can be reduced to linearized equations in small changes in the position and orientation of the sensor. This is accomplished by using the previous measurements of position and orientation to compute rotation matrices that approximately undo the effects of the large-angle sensor position and orientation (Ref 30:411). Through these computational techniques the pilot's line-of-sight can be tracked throughout the mission.
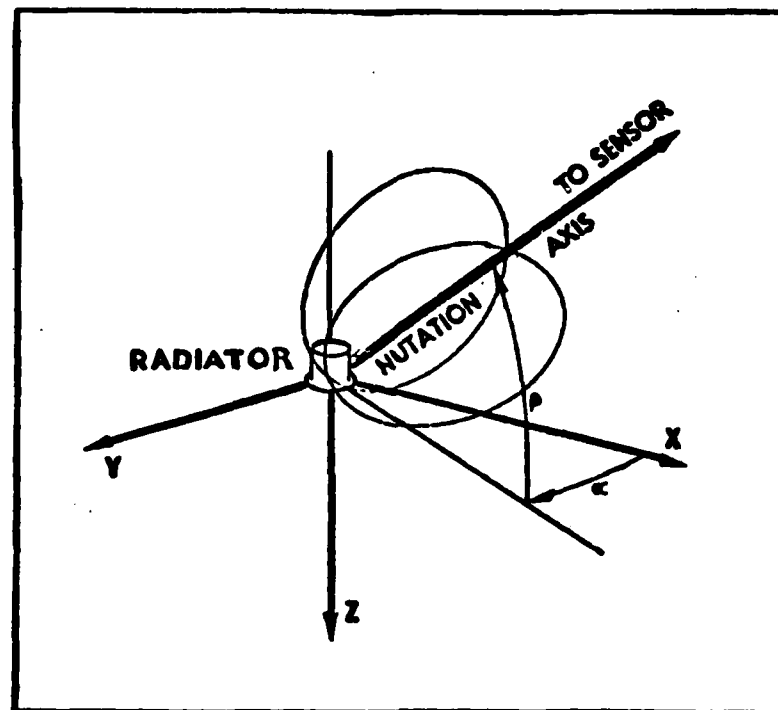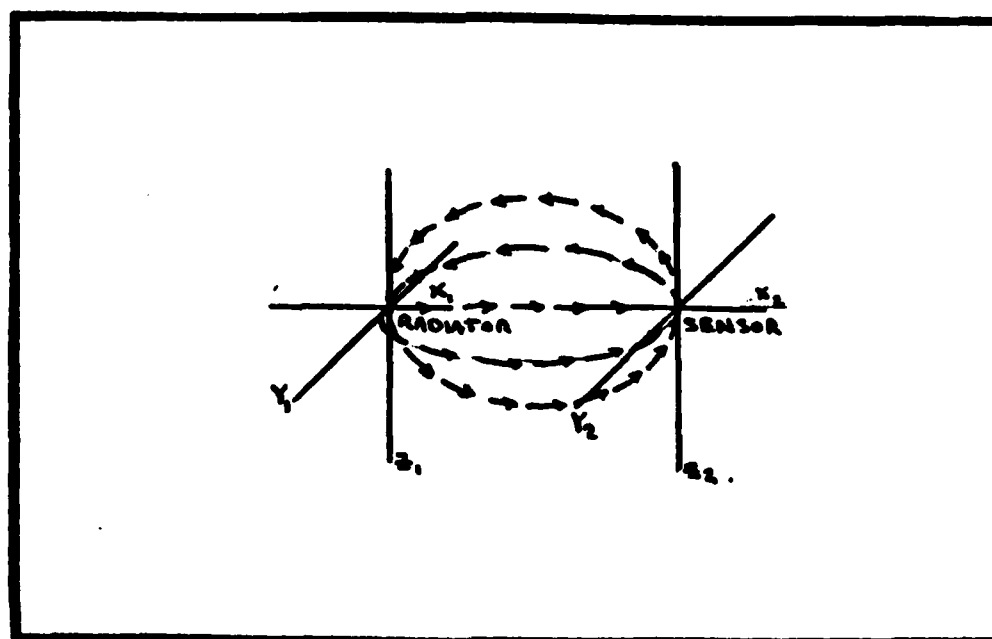
184

Figure A.3   Radiator Pointing

Figure A.4   Coupling Between Sensor & Radiator,
Radiator & Sensor Frames Aligned

185

Vita

Wayne Russell Clubine was born on 26 April 1952, in Toronto, Ontario, Canada. He graduated from high school in Stouffville, Ontario, in 1971. He attended the Royal Military College of Canada, in Kingston, Ontario; graduating in 1975 with a Bachelor of Applied Science degree.

Upon completion of his Aerospace Engineering training in 1976, he was stationed at Canadian Forces Base North Bay. From 1976 to 1981, he served as the Avionics Maintenance Officer for the Electronic Warfare Squadron. From 1978 to 1981 he was a Quality Assurance engineer with the CP-140 Aurora Procurement program in Burbank, California.

In June 1981, he was selected to join the resident Graduate Guidance and Control program under the Department of Electrical Engineering at the United States Air Force Institute of Technology. He is currently assigned to the Communications and Navigation office with the Director General of Aircraft Engineering and Maintenance Division in Ottawa.

Permanent Address: 6392 St. Louis Drive
Orleans, Ontario
K1C 2X2

REPORT DOCUMENTATION PAGE

1. REPORT NUMBER	2. GOVT ACCESSION NO.	3. RECIPIENT'S CATALOG NUMBER
AFIT/GE/EE/82D-24		

4. TITLE (and Subtitle)	5. TYPE OF REPORT & PERIOD COVERED
MODELING THE HELMET-MOUNTED SIGHT SYSTEM	MS Thesis
	6. PERFORMING ORG. REPORT NUMBER

7. AUTHOR(s)	8. CONTRACT OR GRANT NUMBER(s)
Capt Wayne R. Clubine Canadian Armed Forces	

9. PERFORMING ORGANIZATION NAME AND ADDRESS	10. PROGRAM ELEMENT, PROJECT, TASK AREA & WORK UNIT NUMBERS
Air Force Institute of Technology (AFIT-EN) Wright-Patterson AFB OH 45433	

11. CONTROLLING OFFICE NAME AND ADDRESS	12. REPORT DATE
Air Force Avionics Laboratory (AAAN) Wright-Patterson AFB OH 45433	December 1982
	13. NUMBER OF PAGES
	196

14. MONITORING AGENCY NAME & ADDRESS(if different from Controlling Office)	15. SECURITY CLASS. (of this report)
	15a. DECLASSIFICATION/DOWNGRADING SCHEDULE

16. DISTRIBUTION STATEMENT (of this Report)

Approved for public release; distribution unlimited

17. DISTRIBUTION STATEMENT (of the abstract entered in Block 20, if different from Report)

18. SUPPLEMENTARY NOTES

19. KEY WORDS (Continue on reverse side if necessary and identify by block number)

Helmet-Mounted Sight System

Pilot Aiming Errors

HMS Error Model

20. ABSTRACT (Continue on reverse side if necessary and identify by block number)

This report describes the development of an error model for the Helmet-Mounted Sight System. This model is designed to generate the HMS aiming errors that are encountered when the sight is used in the Navigation Update role. This report details the research performed to identify, catagorize, and model the Helmet-Mounted Sight (HMS) errors. The HMS error model includes errors generated by the human operator, the HMS equipment, the vibration environment, canopy refraction, and the system boresighting procedure. The final portion of this report demonstrates the performance of this model in a Monte Carlo simulation program.

DD FORM 1473 EDITION OF 1 NOV 65 IS OBSOLETE
1 JAN 73

EN